



**Rafael Peralta Muniz Moreira**

**Displacement flow of compressible non-Newtonian fluids in annular geometries for well cementing applications**

**Dissertação de Mestrado**

Dissertation presented to the Programa de Pós-graduação em Engenharia Mecânica of PUC-Rio in partial fulfillment of the requirements for the degree of Mestre em Engenharia Mecânica.

Advisor: Profa. Mônica Feijó Naccache

**Rio de Janeiro  
October 2023**



**Rafael Peralta Muniz Moreira**

**Displacement flow of compressible non-Newtonian fluids in annular geometries for well cementing applications**

Dissertation presented to the Programa de Pós-graduação em Engenharia Mecânica of PUC-Rio in partial fulfillment of the requirements for the degree of Mestre em Engenharia Mecânica. Approved by the Examination Committee.

**Profa. Mônica Feijó Naccache**

Advisor

Departamento de Engenharia Mecânica – PUC-Rio

**Dra. Priscilla Ribeiro Vargas**

Departamento de Engenharia Mecânica – PUC-Rio

**Dr. André Leibsohn Martins**

CENPES – Petrobras

Rio de Janeiro, October 20th, 2023

### **Rafael Peralta Muniz Moreira**

Rafael Peralta graduated in Mechanical Engineering in the Federal University of Santa Catarina (UFSC) in 2009.

In 2010 Rafael joined Petrobras as a Petroleum Engineer and completed the Corporate Petroleum Engineering Training Course early 2011. Since then, he developed a career in deepwater-wells drilling and interventions, focusing on casing and cementing design and operations and integrity assessment of the well structure.

Currently, Rafael works in the Wells Engineering Department at the Directory of Engineering and Technology for Upstream Projects as a Technical Advisor for Well Cementing and Zonal Isolation and lead the technical guidelines and the Well Cementing and Zonal Isolation Technical Authority Group.

From 2021 to 2023 he developed part-time research at the Rheology Group at PUC-Rio, where he is currently a Master Candidate in the Mechanical Engineering Department.

#### Bibliographic data

Moreira, Rafael Peralta Muniz

Displacement flow of compressible non-newtonian fluids in annular geometries for well cementing applications / Rafael Peralta Muniz Moreira; advisor: Mônica Feijó Naccache. – 2023.

149 f. : il. color. ; 30 cm

Dissertação (mestrado)–Pontifícia Universidade Católica do Rio de Janeiro, Departamento de Engenharia Mecânica, 2023.

Inclui bibliografia

1. Engenharia Mecânica – Teses. 2. Cimentação de poços. 3. Fluidos não-newtonianos. 4. Reologia. 5. Análise numérica. 6. Simulação em fluidos complexos. I. Naccache, Mônica Feijó. II. Pontifícia Universidade Católica do Rio de Janeiro. Departamento de Engenharia Mecânica. III. Título.

To my wife Sara Lorena and my son Rafael  
who are the reason for my existence.

## Acknowledgments

I wish to thank my family for their support and encouragement throughout my studies, especially to my mother (Regina) which inspired me to follow further academic studies.

To my wife Sara Lorena and my son Rafael, for patience and love when I had to focus on this work at home.

To my advisor, Prof. Mônica Feijó Naccache, for the guidance and trust throughout the development of this work.

To all professors and employees of PUC-Rio, for great lectures and partnership in developing and maintaining this remarkable university, and to all GReo (Rheology Group) team as well.

To Petrobras for providing incentives for my continuous development in the mechanical engineering master. To the managers that provided me with the dedication time to the course and to my company colleagues that supported me taking some of the work when developing this dissertation, especially Gilson Campos and Thiago Piedade.

To CAPES and PUC-Rio, for financial support.

This study was financed in part by the Coordenação de Aperfeiçoamento de Pessoal de Nível Superior - Brasil (CAPES) - Finance Code 001.

## Abstract

Moreira, Rafael P.M.; Naccache, Mônica (Advisor). **Displacement flow of compressible non-Newtonian fluids in annular geometries for well cementing applications.** Rio de Janeiro, 2023.149p. Dissertação de mestrado – Departamento de Engenharia Mecânica, Pontifícia Universidade Católica do Rio de Janeiro.

This master dissertation investigates multiphase displacement flow in annular geometries involved in well cementing operations with foamed cement slurries and spacers. Well cementing plays a relevant role in well integrity and some applications require combining a low-density cement slurry with high compressive strength, and foamed cement suits this purpose. To properly model the displacement complexity involving foamed fluids flow - pressure and temperature dependent densities and non-Newtonian rheology - a 3-dimensional computational fluid dynamics (CFD) model was developed from the open-source OpenFOAM toolbox. The mass, momentum and phase conservation equations are solved in an annular geometry, taking the effect of pressure in the fluid density and rheology, and the volume-of-fluid (VoF) method was used to capture the interface between the fluids. The models were validated using exact solutions for axisymmetric single-phase flow with incompressible and compressible fluids, and Newtonian and non-Newtonian constitutive models. Further, multiphase simulations were performed to estimate the removal efficiency of the drilling fluid by the foamed cement slurry/spacer in different conditions – density and viscosity contrast, eccentricities, and flow rate - and with different correlations for the foamed cement rheological behavior. Finally, the displacement simulations with constant density and rheology displacing fluids (unfoamed) were performed and used to compare the results with the foamed displacing fluids. The results indicate that the displacement efficiency with a foamed cement technique outperforms constant density lightweight cement slurries with similar conditions and are much less sensitive to impairment when challenging conditions are present.

## Keywords

Well Cementing; Non-Newtonian Fluids; Rheology; Numerical Analysis; Complex Fluids Simulations; Foamed Fluids, CFD.

## Resumo

Moreira, Rafael P.M.; Naccache, Mônica. **Deslocamento de fluidos não newtonianos compressíveis em espaços anulares aplicados a cimentação de poços**. Rio de Janeiro, 2023. 149p. Dissertação de Mestrado – Departamento de Engenharia Mecânica, Pontifícia Universidade Católica do Rio de Janeiro.

Esta dissertação investiga escoamentos multifásicos de deslocamento de fluidos em geometrias anulares envolvidas em operações de cimentação de poços com fluidos espumados. A cimentação desempenha um papel relevante na integridade de poços e algumas aplicações requerem pastas leves com alta resistência à compressão, e o cimento espumado atende a este propósito. Para modelar adequadamente a complexidade do escoamento - que compreende comportamento não-newtoniano e elevada compressibilidade - um modelo tridimensional de dinâmica computacional de fluidos (CFD) foi desenvolvido a partir do código aberto OpenFOAM. As equações de conservação da massa, momento e fases são solucionadas em uma geometria anular, considerando o efeito da pressão na densidade e na reologia dos fluidos, e o método *Volume of Fluid* (VoF) foi usado para capturar a interface entre fluidos. Os modelos foram validados com soluções exatas para escoamento monofásico axissimétrico com fluidos incompressíveis e compressíveis, e com modelos constitutivos newtonianos e não-newtonianos. Além disso, simulações multifásicas estimaram a eficiência de deslocamento do fluido de perfuração pela pasta de cimento em diferentes condições – contraste de densidade e de viscosidade, ecentricidade e vazões de bombeio – e com diferentes correlações para a reologia dos fluidos espumados. Finalmente, simulações de deslocamento com fluidos com densidade e reologia constante (não-espumados) foram utilizadas para comparação. Os resultados indicam que a eficiência no deslocamento com a técnica de cimentação espumada é superior em condições similares e ilustra que as pastas espumadas são menos susceptíveis a gerarem falhas quanto condições desafiadoras estão presentes.

## Palavras-chave

Cimentação de Poços; Fluidos Não-Newtonianos; Reologia; Análise Numérica; Simulação em Fluidos Complexos; Fluidos Espumados, CFD.

## **Table of contents**

1. Introduction	21
1.1. Overview	21
1.2. Motivation	26
1.3. Objectives	28
1.4. Structure of Dissertation	29
2. Literature Review	31
2.1. Foamed cement properties and preparation methods	31
2.2. Design of foamed cementing operations	39
2.3. Modeling of multiphase flow for well cementing operations	46
2.4. General remarks and gaps from literature review	52
3. Methodology - Development of numerical model	54
3.1. Problem Definition and Governing Equations	54
3.1.1. Equation of state	56
3.1.2. Constitutive transport model	58
3.2. Finite Volume Method and Interface capturing modeling of multiphase flow	59
3.3. Surface tension modeling	63
3.4. Numerical schemes, discretization, and boundary conditions	65
3.4.1. Geometry Discretization	65

3.4.2. Boundary conditions	71
3.4.3. Numerical Schemes	72
3.4.4. Herschel-Bulkley Regularization	73
4. Test cases and parametric analysis	76
4.1. 1D steady-state single-phase flow verification and validation	76
4.2. Influence of the eccentricity on hydraulics of foamed fluids	80
4.3. Well cementing scenarios and test cases details	84
4.3.1. Simple test case	84
4.3.2. Realistic scenario case	89
4.4. Parametric analysis of displacement flow, dimensional analysis	92
5. Results and discussions	97
5.1. Results from the foamed cement displacement simulations	97
5.1.1. Eccentricity effect in the displacement efficiency	97
5.1.2. Deviation angle effect in the displacement efficiency	101
5.1.3. Effects from density and viscosity contrast in the displacement efficiency	105
5.1.4. Effect of Reynolds Number in the displacement efficiency	108
5.1.5. Effect of foam constitutive model in the displacement efficiency	108
5.2. Results from the constant density and rheology cement displacement simulations	112

5.3. Comparison of systems from displacement perspective and important considerations	116
5.3.1. Displacement Efficiency comparison	116
5.3.2. Channeling growth in eccentric annuli	122
6. Conclusions	127
6.1. Future work proposals	130
Bibliography	131
Nomenclature	136
Appendix A – New Solver Compilation	138
Appendix B – Validation of steady-state single-phase flow	146
Appendix C – List of variables per case	149

## List of figures

Figure 1-1. Fossil fuel demand in the Stated Policies Scenario (IEA, 2022)	21
Figure 1-2. Lifecycle of wells (ANP, 2016)	23
Figure 1-3. Well cementing steps and overview	24
Figure 1-4. Deepwater Horizon Accident in the Macondo Well (Macondo Report, 2011)	25
Figure 1-5. Deepwater well with multiple cemented phases (left) and well with single long cemented phase (right)	26
Figure 1-6. Operational window and pressure profiles for multiple (left) and single (right) phase design.	27
Figure 2-1. Field preparation of foamed cement (IADC Drilling Contractor, 1999)	32
Figure 2-2. Foamed cement choke diagram (SLB)	32
Figure 2-3. Field generated foamed cement.	33
Figure 2-4. Tomography of foamed-cement samples (Cunningham et al, 2017)	34
Figure 2-5. Classification of foams and energized fluids based on volume fraction (Faroughi, 2015).	35
Figure 2-6. Relative viscosity behavior of energized fluids and foams (Faroughi, 2015)	36
Figure 2-7. Relative viscosity of energized fluid from base fluid viscosity ( $\eta_{fb}$ ) for low qualities	39
Figure 2-8. Wellhead pressure for foamed and unfoamed cementing	

operation (Guillot, 2012)	41
Figure 2-9. Minimum and maximum equivalent circulation density (ECD)	42
Figure 2-10. Foamed cementing pumping strategies	44
Figure 2-11. Evolution of top of cement after placement due to temperature equilibrium with the adjacent formations (adapted from Guillot, 2012)	45
Figure 2-12. Generalized Newtonian models (adapted from Barnes)	47
Figure 2-13. Flow curve of displaced (Fluid 1) and displacing fluid (Fluid 2) in annular flow. Top: Shear-rate and shear stress curve; Bottom: Flow rate and pressure gradient curve (for specific geometry).	50
Figure 2-14. Minimum normalized Reynolds number for a turbulent flow in wide side of annulus (Nelson, 2006)	51
Figure 3-1. Schematic of the simplified geometric and flow model of well cementing	54
Figure 3-2. Conservation of a quantity “F” in a discrete element	60
Figure 3-3. VOF interface (Source: NPTEL)	61
Figure 3-4. Workflow development of a custom solver in OpenFOAM with new equations of state and viscosity functions	63
Figure 3-5. Surface tension modeling as a CSF (adapted from Brackbill, 1991)	65
Figure 3-6. Basic mesh of the concentric case (Z normal)	66
Figure 3-7. Basic mesh of the concentric cases (Y direction normal)	67

Figure 3-8. Boundary surfaces for 2D simulations. (Green: Inlet; Yellow: External wall; White: Symmetry; Blue: Internal wall; Red: Outlet)	68
Figure 3-9. 3-dimensional discretization (eccentric cases)	69
Figure 3-10. Regularized (top) and unregularized (bottom) examples of the Herschel-Bulkley Fluid Model	75
Figure 4-1. Validation case for Newtonian incompressible fluid	78
Figure 4-2. Validation case for non-Newtonian (Power-law) incompressible fluid	78
Figure 4-3. Validation case for non-Newtonian (Herschel-Bulkley) incompressible fluid	78
Figure 4-4. Validation case for non-Newtonian compressible fluid	79
Figure 4-5. Validation case for non-Newtonian compressible fluid – annular velocity	80
Figure 4-6. Velocity Profile for 75% eccentricity	81
Figure 4-7. Velocity Profile for 50% eccentricity	82
Figure 4-8. Velocity Profile for 25% eccentricity	82
Figure 4-9. Pressure Drop for eccentric, 3D, single fluid simulations.	83
Figure 4-10. Pressure for eccentric annulus foamed fluid flow drop comparisons with Bailey correlation.	84
Figure 4-11. Velocity and phase concentration fields in 2D simulations showing interface evolution.	86
Figure 4-12. Velocity profile evolution with the density and rheology pressure dependence at $t = 2,6s$ for sections at $z = 0,5m$ ; $z = 1,0m$ and	

z = 2,0m.	87
Figure 4-13. Average density profile at wide and narrow side of annular space	87
Figure 4-14. Control Volume definition for TED calculations	88
Figure 4-15. Displacement efficiency curves for the control volume in annular space	89
Figure 4-16. Well configuration for simulations.	90
Figure 4-17. Flow curves for the fluids in the case study, considering the inlet conditions.	91
Figure 5-1. Foamed fluid Fluid 2 concentration (Reference Case) for concentric (Foam #1) and eccentric (Foam #3) annulus at z = 2.0m for different pumped volumes	98
Figure 5-2. Interface shape at $V^*=1.02$ around z=2.0m (Reference Case) for concentric (Foam #1) and eccentric (Foam #3) annulus	98
Figure 5-3. Eccentricity effect for basic case simulations on TDE (cases Foam #1, Foam #3, and Foam #5)	99
Figure 5-4. External wall fluid concentration for base case at $V^*=1.64$ (cases Foam #1, Foam #3, and Foam #5)	100
Figure 5-5. Fluid Concentration evolution in the external wall for base case at $e^* = 0.75$ (Foam #5)	100
Figure 5-6. Wall displacement efficiency (WDE) for the base case and different eccentricities	101
Figure 5-7. Velocity and volume fraction for $0^\circ$ and $90^\circ$ with $e^*=0.50$	102
Figure 5-8. Total displacement efficiency (TDE) for basic case simulations considering well deviation effect (cases Foam #1, Foam	

#3, Foam #7 and Foam #8)	103
Figure 5-9. Wall displacement efficiency (WDE) for the base case and different well deviations (cases Foam #1, Foam #3, Foam #7, and Foam #8)	104
Figure 5-10. Results from centralized ( $e^*=0$ ) and variations in the Fluid 1 Rheology (cases Foam #1, Foam #9 and Foam #11)	106
Figure 5-11. Results from centralized ( $e^*=0$ ) and variations in the Fluid 1 Density (cases Foam #1, Foam #13, Foam #15, and Foam #17)	106
Figure 5-12. Results from eccentric base case ( $e^*=0.50$ ) and combined eccentric, inclined and with lower viscosity ratio (cases Foam #3 and Foam #23)	107
Figure 5-13. Results from centralized ( $e^*=0$ ) and variations in the Reynolds Number (cases Foam #1, Foam #19, and Foam #21)	108
Figure 5-14. Effect from foam rheological correlation for concentric ( $e^*=0$ ) cases (Foam #25, Foam #26, and Foam #27)	109
Figure 5-15. Effect from eccentricity for the simulations with the base case fluids and correlation from Rosenbaum et al. (cases Foam #3 and Foam #28)	110
Figure 5-16. Difference in Wall Displacement Efficiency (WDE) for the two constitutional models considered in the simulations (at $V^*=1.6$ ).	111
Figure 5-17. Comparison of the displacement at the external wall (Cases Foam #3 and Foam #28)	112
Figure 5-18. Effect from eccentricity for the simulations with the base case with constant density displacing fluid (cases Constant #2, Constant #4 and Constant #6)	114
Figure 5-19. Effect from viscosity contrast for the simulations with	

constant density displacing fluid (cases Constant #2, Constant #10, and Constant #12)	114
Figure 5-20. Effect from density contrast for the simulations with constant density displacing fluid (cases Constant #2, Constant #14, Constant #16, and Constant #18)	115
Figure 5-21. Effect from flow rate for the simulations with constant density displacing fluid (cases Constant #2, Constant #20, and Constant #22)	115
Figure 5-22. Results from eccentric base case ( $e^*=0.50$ ) and combined eccentric, inclined and with lower viscosity ratio for constant-density displacing fluid (cases Constant #4 and Constant #24)	116
Figure 5-23. Eccentricity effect comparison	118
Figure 5-24. Density contrast comparison	119
Figure 5-25. Comparison of efficiency from the effect of flow rate	120
Figure 5-26. Comparison of efficiency from the combined effect of eccentricity and viscosity ratio	121
Figure 5-27. Density profile in annulus for foamed fluid simulation (left) and constant density (right), at $V^* = 1.6$ .	122
Figure 5-28. Interface Position in annulus for base case with $e^*=0.50$ .	123
Figure 5-29. Channel length for base case simulation with $e^*=0.50$ and $\beta = 0$ .	123
Figure 5-30. Interface Position in annulus for complex 3D case with $e^* = 0.50$ .	124
Figure 5-31. Channel length for complex case simulation with $e^*=$	

0.50 and  $\beta = 450$ .

125

Figure A-1. Child class created cimThermo for the thermodynamical properties

138

## List of tables

Table 2-1. Summary of studies on energized and foamed fluids rheology	38
Table 2-2. Generalized Newtonian Fluid Models	47
Table 2-3. Causes and consequences of an impaired displacement process.	49
Table 2-4. Parameters for example of frictional pressure contrast	50
Table 3-1. Mesh discretization	70
Table 3-2. Mesh quality properties for hexahedral elements	70
Table 4-1. Fluid and flow parameters for incompressible validation cases	77
Table 4-2. Fluid and flow parameters for compressible validation case	77
Table 4-3. Test case data	85
Table 4-4. Basic data for the deepwater well case study	90
Table 4-5. Fluid data for deepwater well case study	91
Table 4-6. Cases with Ducloué Correlation – Reference Flow parameters, changing geometry.	95
Table 4-7. Cases with Ducloué Correlation, changing flow parameters.	95
Table 4-8. Simulation of eccentric cases from the worst cases in the concentric simulations	96

Table 4-9. Cases considered to evaluate the correlation effect from Eq. 3-22	96
Table 5-1. Summary results for base case at different eccentricities	101
Table 5-2. Results for the simulations at $V^* = 1.64$ with variable deviation angles (cases Foam #1, Foam #3, Foam #7, and Foam #8)	105
Table 5-3. Difference in displacement efficiency results with correlation from Eq. 3-22 in relation to the correlation from Eq. 3-20	111
Table 5-4. Source for TDE and WDE for the constant density displacing fluid simulations	113
Table 5-5. Source for comparison between foamed and unfoamed displacing fluid	117
Table 5-6. Rheology and viscosity contrast effect comparison	119
Table 5-7. Channel size at $V^* = 1.6$ for base case and complex case	126
Table C-1. Parameter list	149

*“Whoever you are, no matter what social position you have in life, rich or poor, always show great strength and determination, and always do everything with much love and deep faith in God. Then one day you will reach your goal. You will reach your goal, somehow.”*

Ayrton Senna

# 1

## Introduction

### 1.1.

#### Overview

The oil and gas industry still has a relevant role in the energy supply worldwide and will continue to play during the ongoing energy transition. Based on the data by the International Energy Agency (IEA, 2022), oil and natural gas corresponded in 2022 for approximately 54,4% of the total world energy supply (TES) and forecasts estimates it will respond to 53,2% in 2030 and 46,3% of TES in 2050 (Figure 1-1). Even in an increasing speed in energy transition, leading to a lower demand on petroleum and derived products – Announced Pledges Scenario (APS) – the IEA predicts a participation of oil and gas sources in TES of 47,7% in 2030, which represents a net increase in the total production of oil and gas from the 2022 basis.

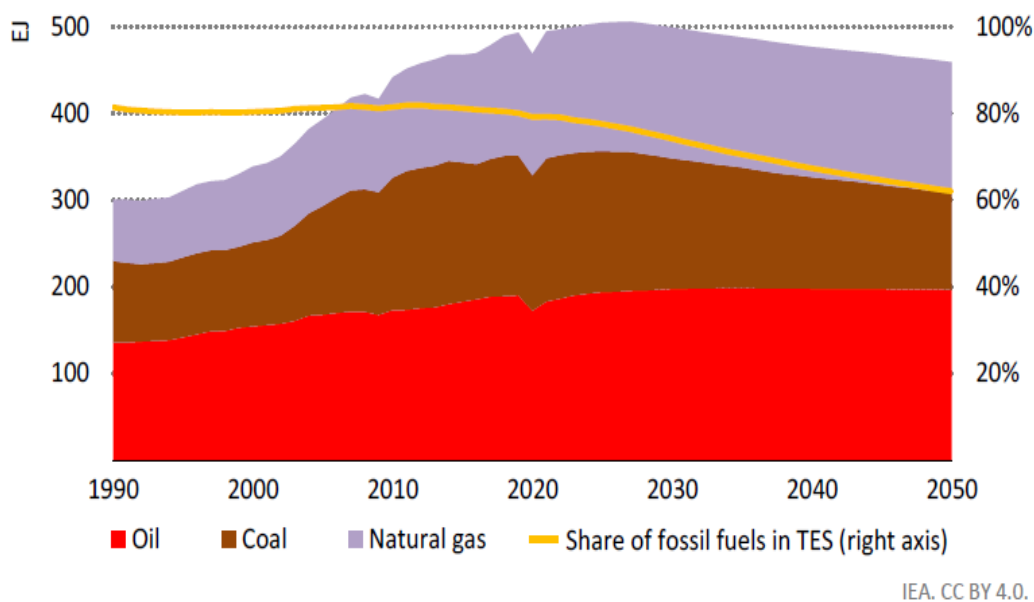


Figure 1-1. Fossil fuel demand in the Stated Policies Scenario (IEA, 2022)

In Brazil, regardless of the alignment with the energy transition, the Empresa de Pesquisa Energética (EPE) predicts that the national oil and gas production will rise from 2.9 million of equivalent barrels per day (boed) in 2021 and 3,02 million boed in 2022 to 5.3 million in 2030, an increase of 82% in 10 years. For that

purpose, the production development projects that are already approved consider investments around US\$ 156 billion up to 2030 (EPE, Plano Decenal de Energia 2032).

To produce oil and gas in the energy transition environment the industry needs to achieve a reduction in greenhouse gas emissions, due to the absolute increase in the unrenovable fuels output. This could be obtained through an increase in efficiency and sustainability in the industry's operations (IEA, 2022). Besides providing a lower environmental footprint, achieving new standards of safety and efficiency saves cost and provides safe energy supply for society.

Among the large capital expenditures in the Oil and Gas Industry, well construction corresponds to one of the largest investments in exploring and developing an Exploration and Production Project, ranging from 20% up to 50% of the Capital Expenditure (CAPEX). Well construction involves, beyond other activities, the drilling and completion of wells and the installation of production equipment. The criticality of such operations leads to a demand for correct design and construction of well barriers to prevent uncontrolled flow of fluids (such as hydrocarbons) to the external ambient, to different permeable potential flow zones and to the contamination of fresh water in all the field lifecycle, described in Figure 1-2 (ANP, 2016). In addition, the design needs to ensure that the well and all its barriers support the weight of all equipment installed inside the well and above the wellhead and support the service loads that occur during construction, production, interventions, and abandonment (API, 2013; ANP, 2016).

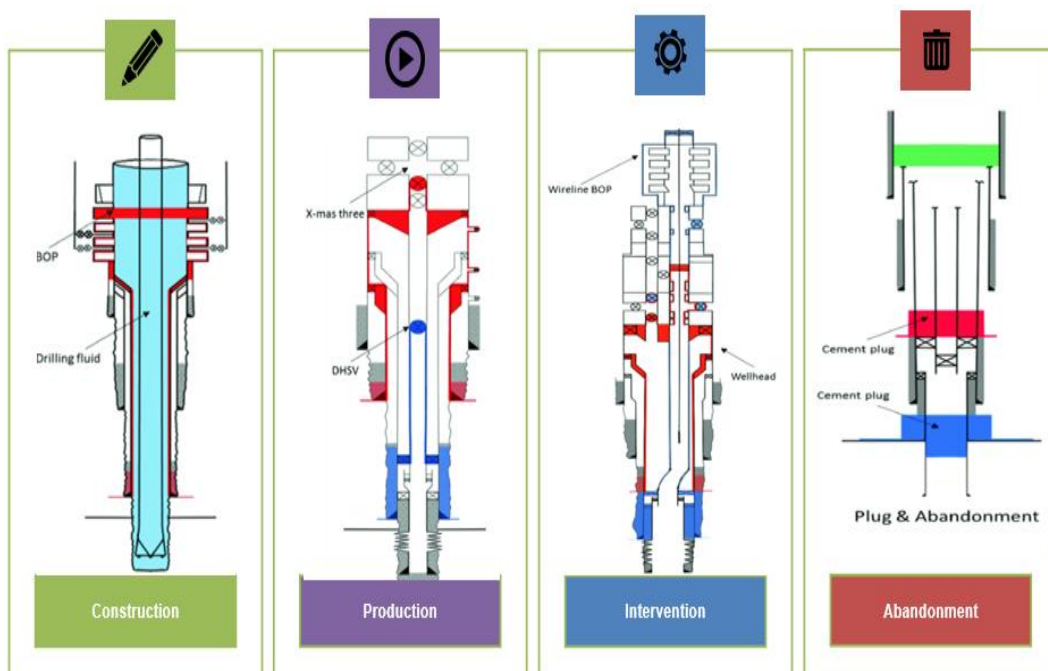


Figure 1-2. Lifecycle of wells (ANP, 2016)

Beyond the oil and gas exploration and production industry, well construction and well integrity also play an important role for geothermal energy projects and Carbon Capture and Storage (CCS). In the first, the wells need to be drilled and completed to allow cold water injection and hot water production. For CCS, the placement of injection and monitoring wells will be part of an infrastructure expected to allow an increase of capacity for CO<sub>2</sub> injection from 45 Mt CO<sub>2</sub> (2022) to 220 Mt CO<sub>2</sub> in 2030 (IEA, 2022), in projects already announced.

Steel casing tubulars and annular cement compose the well structure, the elements that provide the support for production equipment (and subsea equipment in the case of subsea wells) and provide well integrity to avoid the undesired uncontrolled flow of hydrocarbons and other fluids. The casing tubulars are installed in a determined depth after the hole is drilled, followed by the placement of a pumpable cementitious slurry to form the annular barriers to complete the process in each phase of the well. Well cementing therefore fits the purpose of isolating potential flow zones or fresh water and providing structural support for the casing, contributing for well integrity in short, medium, and long term (API, 2010). A schematic of well the cementing process steps is shown in Figure 1-3.

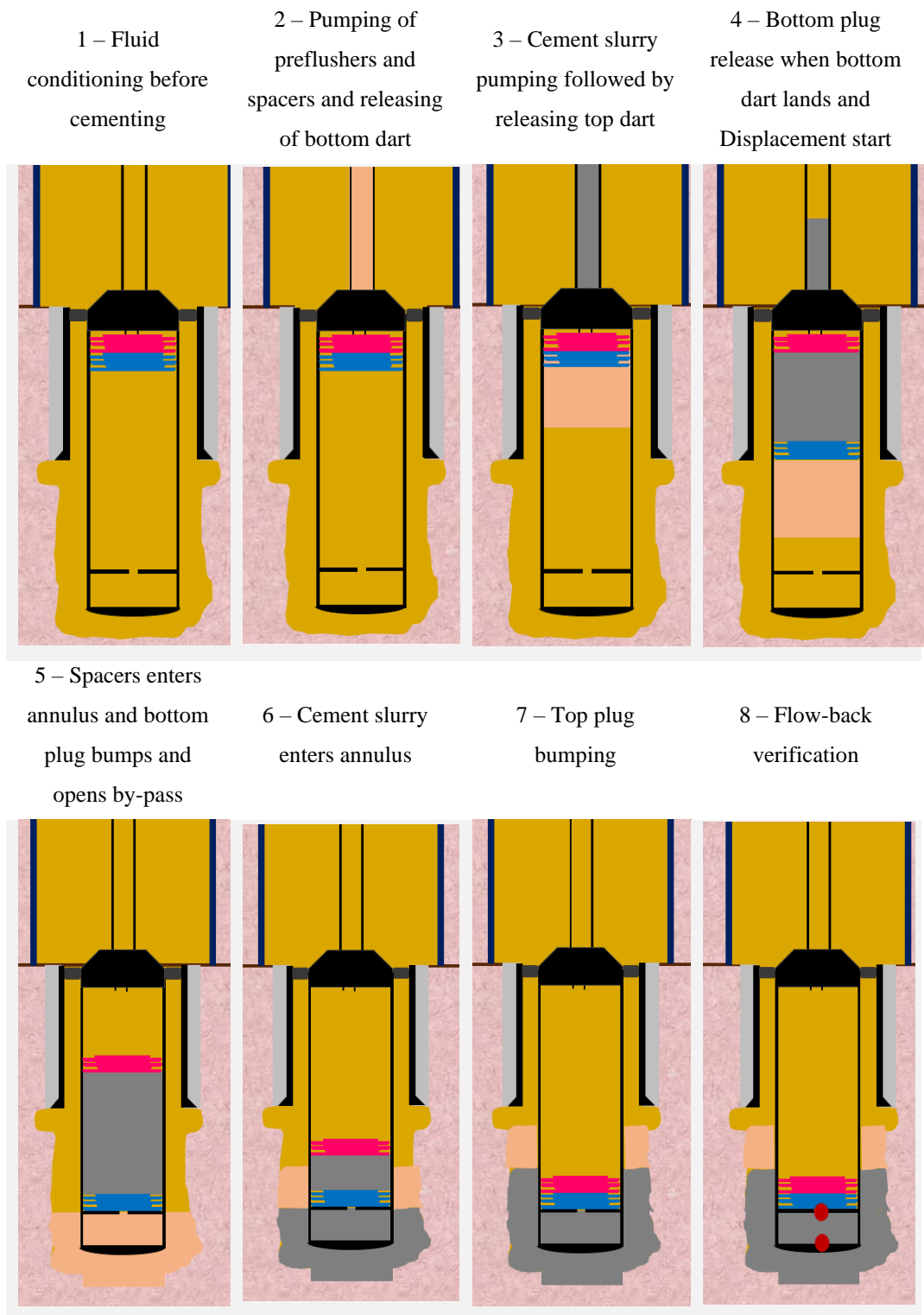


Figure 1-3. Well cementing steps and overview

A well-designed cement job optimizes cement placement through following good practices such as laboratory-tested slurry design, honoring pore pressure/fracture gradient window, use of spacers/pre-flushes, proper density and rheological hierarchy, fluid compatibility and adequate centralization of the casing. The success

of the operation requires that the spacers and cement slurry fully displaced the drilling fluid in the annular geometry for a sufficient length upwards. Several aspects may influence the quality of the cementing process and consequently the quality of the annular isolation, such as the drilled hole profile (no critical enlargement, doglegs, or hole instability), drilling fluid chemical and physical properties, spacers and cement slurry properties and conditioning, casing hardware (float equipment, wiper devices and casing centralizers), flow conditions (pump rates and movement of tubulars), among others. The proper understanding and selection of strategies for the design may define success of zonal isolation (Nelson, 2006; API, 2010).

In addition, well cement poses as a critical operation in well construction and interventions. If inadequate criteria for a cementing design and cement evaluation are executed, hazardous accidents may appear with potential massive environmental and safety consequences (Macondo Report, 2011; Montara Report, 2010). The Macondo incident (Figure 1-4) is frequently reminded as the most critical example.



Figure 1-4. Deepwater Horizon Accident in the Macondo Well (Macondo Report, 2011)

## 1.2.

### Motivation

Many well designs look for the minimum number of phases to reduce costs, which may lead to increasing the length of the cement in the annulus, depending on the amount and location of potential flow zones to be isolated. Long cement columns in annulus often challenge the cementing design and execution due to the higher density of cement slurries compared to the density of drilling fluids, which increase the risk to exceeding fracture gradient of formations (Nelson, 2006; API, 2010). Figure 1-5 shows an example of this reduction of phases, where a well with 4 phases and short-length cement in the intermediate and production casing (left) and a well with 3 phases with a long-length cement column in the production casing (right) are presented.

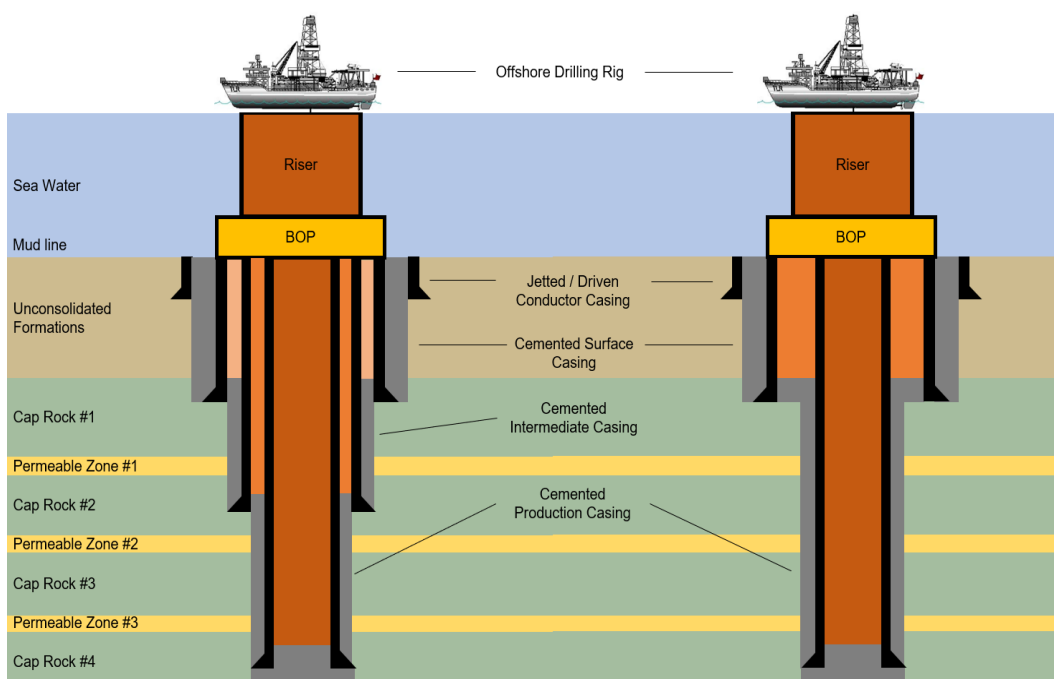


Figure 1-5. Deepwater well with multiple cemented phases (left) and well with single long cemented phase (right)

The cost reduction of decreasing the number of phases in a well can be substantial, in the magnitude order of 30% to 50% of the total drilling time of the well (Ferreira, 2022; Passos, 2023). To make this possible, a feasible and dependable cementing design and execution is mandatory.

Figure 1-6 shows the pressure profile in such alternatives, showing that:

- In a well with multiple phases design (left), a viable cementing design with conventional heavyweight cement slurry exists in both intermediate casing and production casing since the maximum pressure profile respects pore and fracture gradients;
- In a well with a single long cementing design for the production casing (right), the pressure profile for the heavyweight cement slurry exceeds the fracture and would increase risks of inducing fluid losses and lead to a lower top of cement in the annulus, therefore compromising the cementing objectives. However, when a lightweight cement system is designed and selected, the fracture gradient can be respected due to a lower slope on the hydrostatic pressure increase, assuming that the friction pressure is the same in both cases.

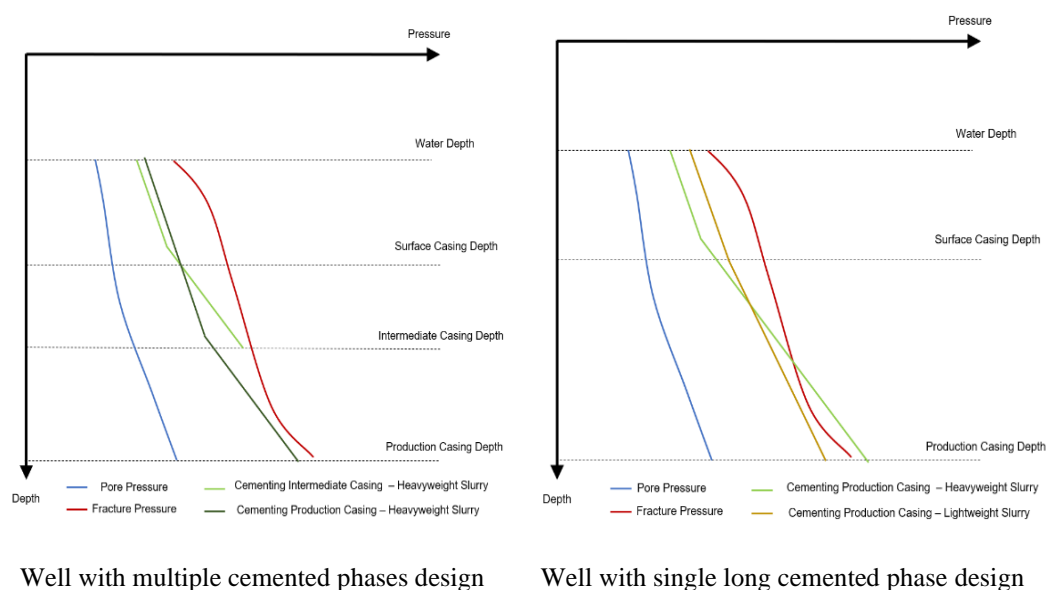


Figure 1-6. Operational window and pressure profiles for multiple (left) and single (right) phase design.

When evaluating a lightweight cementing system to the well design, there are many cementing design alternatives that may be considered under such situations, briefly described below.

- Conventional extended lightweight cement: Cement slurry with high water-cement ratio for reducing the final density of the cement slurry.

Usually, for stabilizing the suspension, additives (extenders and viscosifying agents) are used to avoid settling of the solids and optimizing the rheology.

b) High-performance lightweight cementitious blends: Composite blends of cement with low-density materials, such as glass (hollow spheres) or pozzolan (low-density particles) microspheres. The specific gravity of the particles, their proportion in the blend and water-cement ratio are tailored to achievement of the final desired cement slurry density.

c) Foamed cement: A stabilized dispersion of gas (usually nitrogen) in a cement slurry with the use of foaming agents. The final density of the foamed cement depends on the amount of gas added in the mixture and the pressure and temperature in the well.

d) Multiple stage cementing: Strategy that uses casing equipment to provide hydraulic communication with the annulus in a shallower depth than the casing shoe. Multiple cement jobs may be performed sequentially starting from a different depth in the casing. The disadvantages over the previous alternatives are an increase in the total operational time and the risk of equipment failure.

Therefore, defining a proper strategy for such cementing operations require a comprehensive – especially complex operations like foamed cementing - analysis and understanding of the scenario of each well, since all alternatives have advantages and limitations. Typically, the analysis for the selection of the best alternative relies on the experience of the cementing engineer, however, when considering displacement efficiency in the annulus, the considerations are mostly qualitative.

Consequently, the development of quantitative studies that provide information and present performance differences of cementing design in different well conditions are valuable for the well construction engineer. The innovative research on this dissertation intends to present a new method for evaluating quantitatively different cementing alternatives.

### **1.3.**

#### **Objectives**

This dissertation focuses on the development of computational models and simulation of case studies for improving the comprehension of the annular flow of foamed cement and the displacement of the drilling fluids by foamed spacers and foamed cement slurries.

The specific objectives of this work are the following:

- Develop 2-dimensional and 3-dimensional multiphase transient model capable of simulating real-scale annular displacement flow of foamed fluids and constant density fluids with non-Newtonian constitutive models.
- Apply the developed model in parametric simulations for well foamed cementing applications with real-scale parameters, considering differences in the fluid properties, casing eccentricity, well deviation and flow boundary conditions.
- Perform parametric simulation for unfoamed well cementing in similar conditions than applied for the foamed cementing.
- Compare the performance of foamed and unfoamed cementing strategies to identify key aspects to consider from a fluid displacement perspective that benefits a foamed cement strategy in a particular well condition. The comparison may also be used to identify if displacement efficiency models need a compressible assumption, which increases computational costs.
- Since reproducing field conditions for the cement slurry preparation and pumping are complex, the development of a 3-dimensional computational fluid dynamics (CFD) model for multiphase flow in annular geometries can support the analysis of different well conditions and fluid properties that affect the flow and the displacement in foamed cementing operations, identifying possible hazards and advantages.

#### **1.4.**

#### **Structure of Dissertation**

This research is presented in 6 chapters that include introduction and conclusions. The dissertation also comprises the used bibliography and nomenclature.

Chapter 2: Presents a literature review divided in three different sections. The first, presenting the review of foamed cement properties and preparation methods. The second, presenting the most variables impacting foamed cementing design. Finally, the third, presenting a review for modeling displacement simulations for foamed cementing applications.

Chapter 3: Details the numerical modeling of the displacement of foamed fluids in annular geometries, considering the variables and equations involved, time and space discretization, boundary conditions and numerical methods and criteria.

Chapter 4: Test cases were used to validate the model implementation with exact solutions for annular geometry, and to test the equations implemented comparing with experimental data from literature. In addition, studies eccentricity effects and compares the results with numerical correlations. Finally, presents the well cementing scenarios and case studies, indicates the dimensional and dimensionless parameters, and selects the matrix of numerical experiments.

Chapter 5: Presents the results from the matrix of numerical experiments considering velocity and pressure profiles and the displacement efficiency with both foamed and unfoamed cement used as a displacing fluid. All results consider the set of dimensionless parameters used.

Chapter 6: Presents the conclusions of the work and provides insight and suggestions for future research projects.

## 2

### Literature Review

#### 2.1.

##### **Foamed cement properties and preparation methods**

Well cementing technology companies developed foamed cementing for specialized applications requiring low-density cement with advantages compared to alternative solutions. The first applications date from 1979 and the use began as a cheaper alternative to blended composite cements with low-density particles. Many advantages were reported for scenarios of low fracture gradient, curing loss circulation zones, and due to expanding properties of the foamed cement (Davies et al, 1981). The use of foamed cement also became very relevant in deep-water drilling scenarios for shallow water flow control, which occurs frequently in the Gulf of Mexico and Caribbean Sea (Stiles, 1997; API, 2010; API, 2018; Odden, 2020). The cement sheath also may become more reliable in the long term for preventing loss of well integrity and surface casing vent flow (Ahmady et al, 2020). Many other applications have been reported since.

Preparing a foamed cement involves the injection of a gas, typically nitrogen, from a pressurized unit (using cryogenic N<sub>2</sub> or nitrogen extracted and separated from air) into the existing high-pressure cementing line with the use of a foam generator (Figure 2-1 and Figure 2-2). The base cement slurry is prepared conventionally, and foaming agents are added before the addition of gas (IADC, 1999). A picture of field-generated foamed cement may be seen in Figure 2-3.

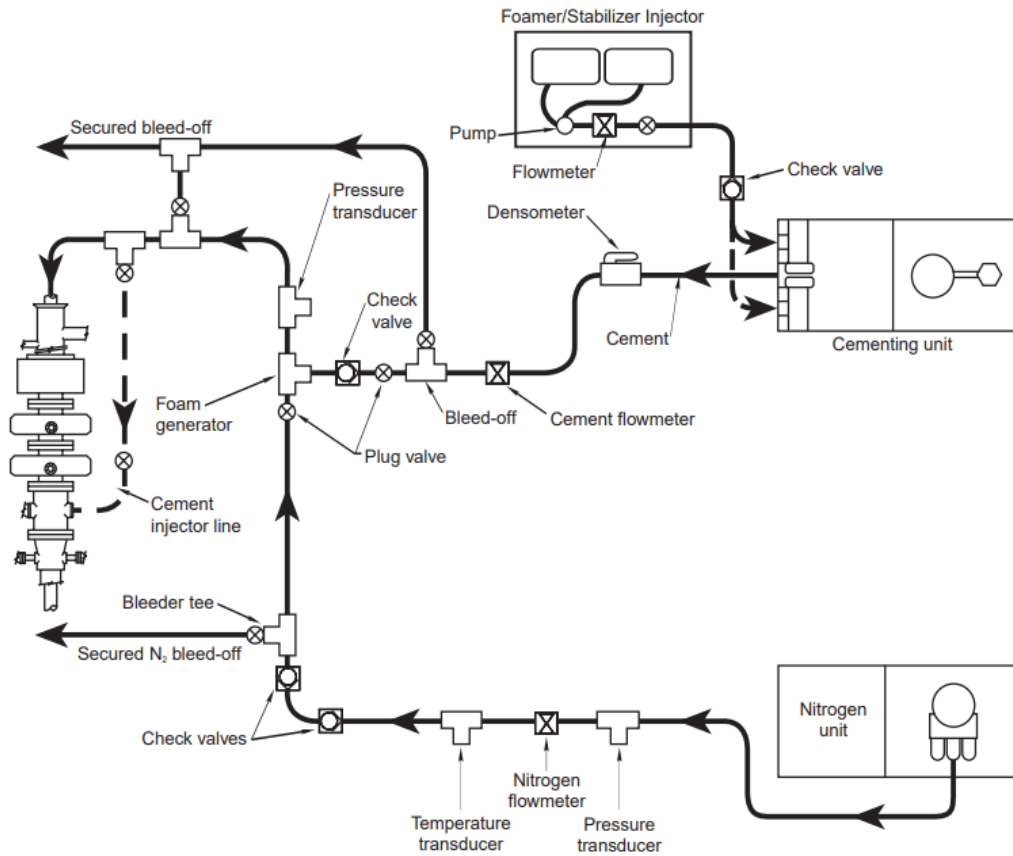


Figure 2-1. Field preparation of foamed cement (IADC Drilling Contractor, 1999)



Figure 2-2. Foamed cement choke diagram (SLB)



Figure 2-3. Field generated foamed cement.

The density of the foamed cement at downhole conditions may be controlled by the rate of gas injection (usually nitrogen) and the density of the base cement slurry. Conventional cement slurries with API Class G or Class H cement type have a target  $1900 \text{ kg/m}^3$  density when mixed with fresh water and conventional additives. With addition of an inert gas, dispersed and stabilized in the mixture, the bottomhole final foamed cement density can become as low as  $420 \text{ kg/m}^3$  in field applications (Nelson, 2006). The compressive strength of a low-density cement slurry obtained is significantly higher than extended high water-to-cement ratio cement slurries (Cunningham, 2017). In addition to not having impaired mechanical properties, foamed cement becomes more mechanically resilient, with lower Young Modulus (50% lower compared to neat heavyweight cement) and lower thermal conductivity (50% lower compared to neat heavyweight cement), making it interesting to applications in heavy-duty environments, such as geothermal wells (Niggemann, 2010).

Foamed cement also presents a lower tendency to dehydrate in front of a

permeable formation, which leads to good fluid loss control even without the use of specific additives (Olowolagba, 2010; Nelson, 2006).

The expansive behavior of foamed cement increases the zonal isolation by minimizing micro annuli and maintaining the hydrostatic pressure during the curing of the cement, impeding gas migration (Davies, 1981; Olowolagba, 2010; API, 2010; Odden, 2020).

Although the addition of dispersed gas bubbles to foamed cement increases its porosity, the permeability of foamed cement remains relatively low and within the ranges of neat base cured cement (lower than 1 mD), if the bubbles are homogeneously distributed in the matrix and the gas volume fraction is below 30% (Cunningham, 2017; Glosser, 2016; Kutchko, 2014).

Dalton et al (2019) also showed through computerized tomography scans (CT) that pressurized foamed cement has smaller bubbles than a sample prepared at atmospheric conditions at the laboratory. The studies concluded that field prepared foamed cement show better zonal isolation properties than the slurries measured in laboratory conditions with standardized measurement methods. CT scans of foamed cement slurries with different volume fractions are shown in Figure 2-4.

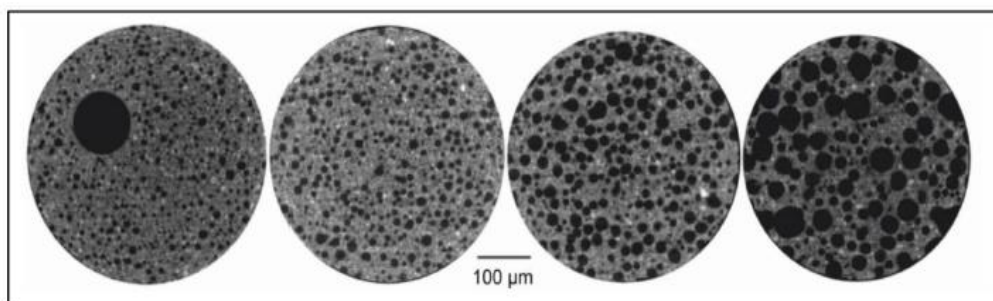


Figure 15—2D slices of reconstructed 3.7- $\mu\text{m}$  resolution CT scans taken of the 0.6-cm diameter subsamples of 10, 20, 30, and 40% air fraction FCR1 (Recipe 1, left to right).

Figure 2-4. Tomography of foamed-cement samples (Cunningham et al, 2017)

Rheological studies of foamed cement and other foamed fluids remain challenging up to the present days. According to several authors (Guillot, 2012; Ahmed, 2009) the rheological behavior of a foam relies heavily on the gas volume fraction, on the flow regime and properties of the base fluid. The effect of the surfactant agent used may also modify the rheology if the bubbles are not encapsulated by solid particles (Feneuil, 2019; Ducloué, 2014). At higher volume

fractions (above 40%), the interaction between the gas bubbles and other dispersed particles becomes more relevant and the dispersed phase may form common boundaries between the bubbles, which loses its sphericity (Faroughi, 2018). Although the term “Foam” is commonly used generally, the term “Energized fluid” would better describe foamed cementing applications, since the gas volume fraction is low to avoid the discussed impairment of permeability and mechanical properties. Energized fluids have diluted or dispersed gas with negligible or little bubble interaction, while in foams the bubbles lose their spherical shape and interact with each other. Figure 2-5 presents schematically this distinction. However, for historical reasons, the term “Foamed cement / cementing” is still used in specialized literature and as field jargon.

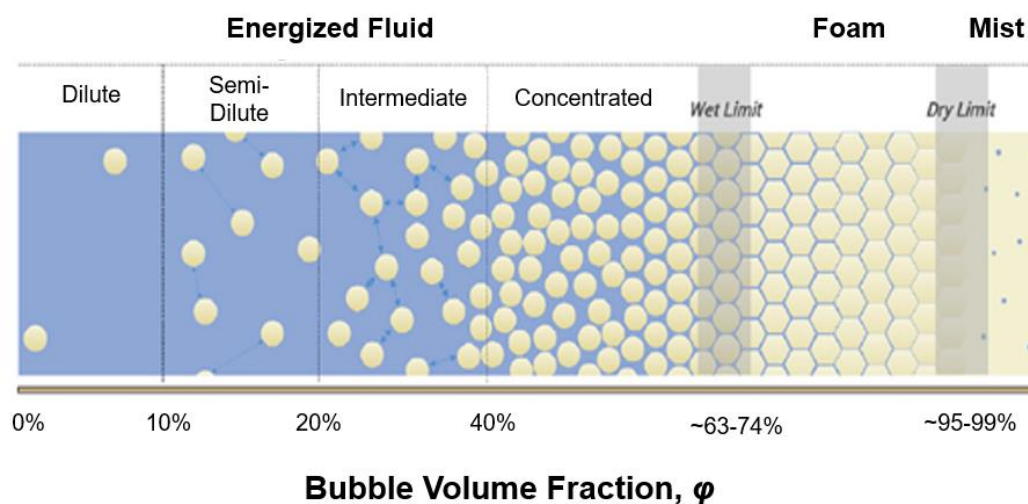


Figure 2-5. Classification of foams and energized fluids based on volume fraction (Faroughi, 2015).

Different methods have been reported to study the rheology of foams with experimental, theoretical, and numerical methods. Due to its complexity, many results require careful consideration. The assumptions over the shape and deformability of the bubbles – in addition to the bubble interaction already discussed – impose different results on the relative viscosity compared to the base fluid. The dimensionless capillary number ( $Ca$ ) represents the relation between the viscous forces acting on the surface of the bubbles and the surface tension forces, and influence directly the energy required to deform and move the bubbles.

Consequently, the resultant rheological behavior may be very different as shown in Figure 2-6 (Faroughi, 2019).

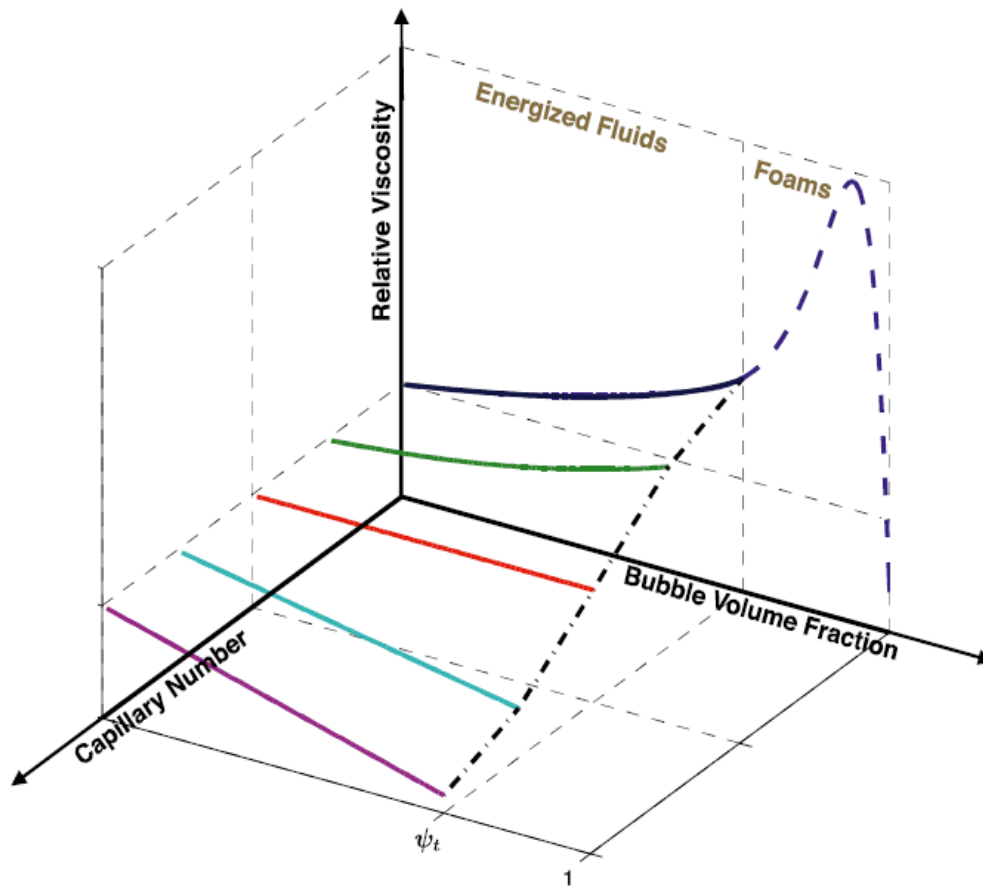


Figure 2-6. Relative viscosity behavior of energized fluids and foams (Faroughi, 2015)

Einstein (1911), Batchelor and Green (1972) and Barthes-Biesel and Chhim (1981) developed theoretical correlations for the viscosity of fluids with dispersed bubbles from the viscosity of the base fluid. The use of pressurized flow loops has been reported in literature (Mitchel, 1971; Bogdanovic, 2009; Ahmed, 2009; Sinha et al, 2019) and has the advantages of being able to consider pressure and temperature effects, however few studies consider foamed fluids with low gas fraction. Ducloué (2014) performed analysis with stress-controlled rheometer and investigated the yield stress, flow consistency and the complex modulus (elastic and viscous) in monodispersed bubble foams prepared with nitrogen and perfluorohexane ( $C_6F_{14}$ ). Feneuil (2019) performed measurements of yield stress with a vane-in-cup geometry on low-quality cement slurries and obtained that the

effect of surfactant used as foaming agent the yield stress could lead to two conflicting results: they may slightly decrease the yield stress or may increase the yield stress when the gas content in the foamed cement increases. Olowolagba (2010) used an improved geometry in a rotational viscometer to avoid the effect of slippage due to the high yield stress and two-phase fluid using foamed cement samples prepared at atmospheric conditions. Rosebaum (2019) performed numerical simulations with Stokesian dynamics with implementation of shearing flow to account for bubble interaction and developed viscosity ratio relations of a bubble suspension compared to a base Newtonian fluid. A summary of the results and relations developed is shown in Table 2-1.

Table 2-1. Summary of studies on energized and foamed fluids rheology

<b>Author</b>	<b>Methodology</b>	<b>Viscosity predictions</b>
Einstein (1911)	Theoretical energy balance for flow with solid, homogeneously distributed spherical bubbles	Linear function of relative viscosity increases with volume fraction
Mitchel (1971)	Experimental measurements in small diameter pipes for low-quality foams	Linear function of relative viscosity increases with volume fraction
Batchelor and Green (1972)	Theoretical study on rheological properties of a suspension of spherical particles with interaction of pairs of spheres for a pure straining flow and low capillary numbers	Quadratic function of relative increases viscosity with volume fraction
Barthes-Biesel and Chhim (1981)	Theoretical study of dilute suspensions with surface tension	Provides a correction in Einstein's equation for high capillary number (Ca) foams
Ahmed, 2009	Flow loop measurements with a flow-through rotational viscometer	Foamed cement with lower viscosity than base cement slurry
Olowolagba (2010)	Rotational modified vane rheometer measurements in foamed cement	Increasing viscosity with volume fraction, and increasing yield point with volume fraction
Ducloué (2014)	Stress-controlled rheometer measurements in aqueous foam	Increasing viscosity with volume fraction with stiff, small bubbles
Feneuil (2019)	Rotational vane-in-cup rheometer measurements with low-quality cement slurries	Slight increase of the yield stress in low capillary number foams (Ca) or particle covered bubbles
Sinha et al, 2019	Flow loop measurements with PAC-based polymeric foams with medium quality	Increased viscosity with gas volumetric fraction with exponential relation
Rosebaum (2019)	Stokesian Dynamics Simulations of foamed cement	Quadratic function of relative viscosity with volume fraction considering bubble polydispersity

Quantitatively, the differences in each relation may differ substantially as shown in Figure 2-7. Many causes should be considered such as the influence of surfactant type and concentration, type of suspension and the experimental method itself.

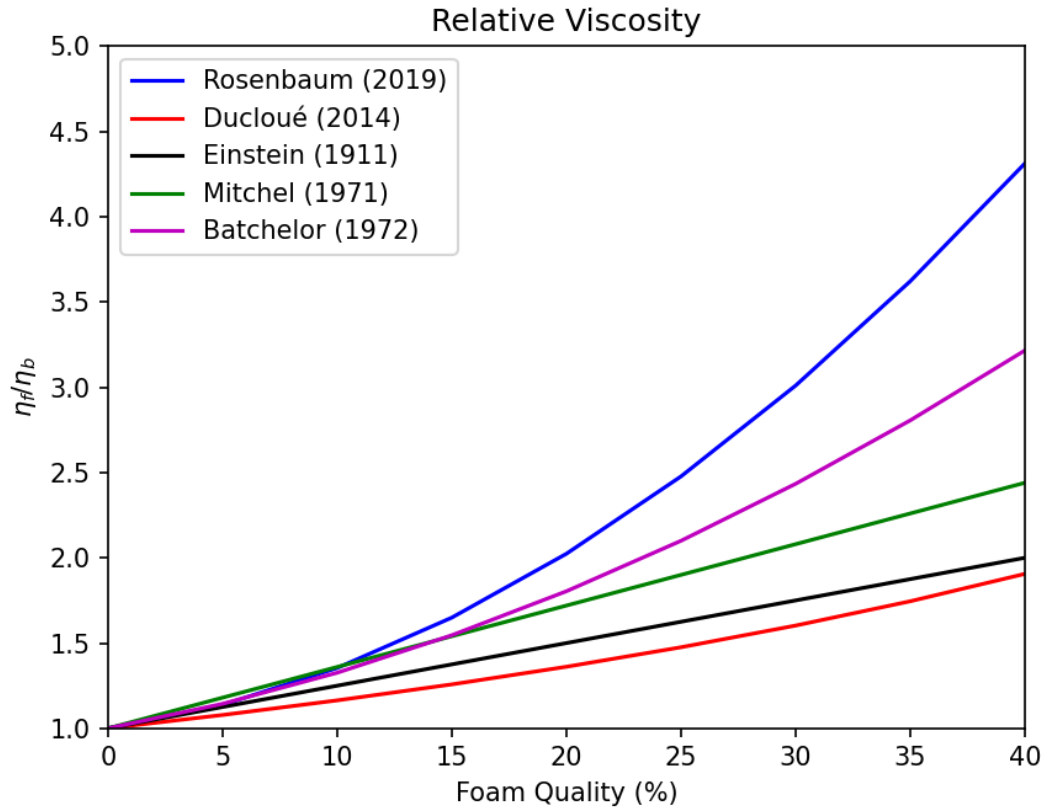


Figure 2-7. Relative viscosity of energized fluid from base fluid viscosity ( $\eta_f/\eta_b$ ) for low qualities

Where:

$\eta_f$  – Foamed fluid viscosity

$\eta_b$  – Base fluid viscosity

Although the studies increased over the years, there's still little experimental work on measuring foamed cement and spacers rheology under high pressure and high temperature (HPHT). Typical rotational HPHT viscometers take ambient pressure and temperature prepared samples and then increase to the desired parameters. Therefore, applying this equipment for foamed cement would result in lower foamed qualities than field conditions.

## 2.2.

### Design of foamed cementing operations

Laboratory testing of foamed cement slurries follows the procedure defined in API RP 10B-4: Preparation and Testing of Foamed Cement Formulations at

Atmospheric Pressure, producing an atmospheric pressure foamed cement sample that mimics the one in downhole conditions (API, 2015). The main recommended practice states that the base cement slurry follows all the design parameters (density, stability, free fluid control, rheology, thickening time, fluid loss, compressive strength) according to the specific scenario of the operation. After preparing the foamed cement sample, the unset and set stability of foamed cement shall be tested to ensure no bubble breakout, no variations in density and no discontinuity on the sample occur.

The field preparation of foamed spacers and cement shall ensure the gas (typically nitrogen) supply rate is synchronized - manually controlled or with automated equipment - with the base cement slurry liquid pump rate and foaming agent pump rate (API, 2010). The gas injection rate follows from the estimated pressure and temperature conditions at the end of the job to the achievement of the desired final density at bottomhole conditions, therefore it will produce a high gas concentration slurry / spacer at surface conditions, where low pressure and ambient temperature are present in the beginning of the cement job. Consequently, due to the low-density of the prepared foamed spacer / slurry in surface conditions (below the density of the drilling fluids), the pumping pressure tends to increase while pumping the foamed fluids. When the foamed fluids achieve a certain pressure inside the well, their density increases again which will decrease the pumping pressure.

This behavior differs from typical cementing operations with constant density fluids, where the fluids accelerate during the pumping inside the landing string and casing due to gravitational effects (free-fall). Figure 2-8 presents an example (Guillot, 2012) for the difference in the pumping pressure (Wellhead pressure) profile in a deepwater 22” casing cementing operation considering compressible (foamed) and incompressible (constant density) lightweight cement slurry. The water depth of the well is 1300m and the casing is 900m long inside a 31” vertical well.

Therefore, for better control and design of the pumping schedule of fluids, the compressible behavior shall be considered and evaluated. In some cases, avoiding free-fall (Terra et al, 2020) will be beneficial to the cement job by ensuring a positive wellhead pressure occurs during the whole operation, providing better control of bottomhole pressure above pore pressure and limits in the well

equipment.

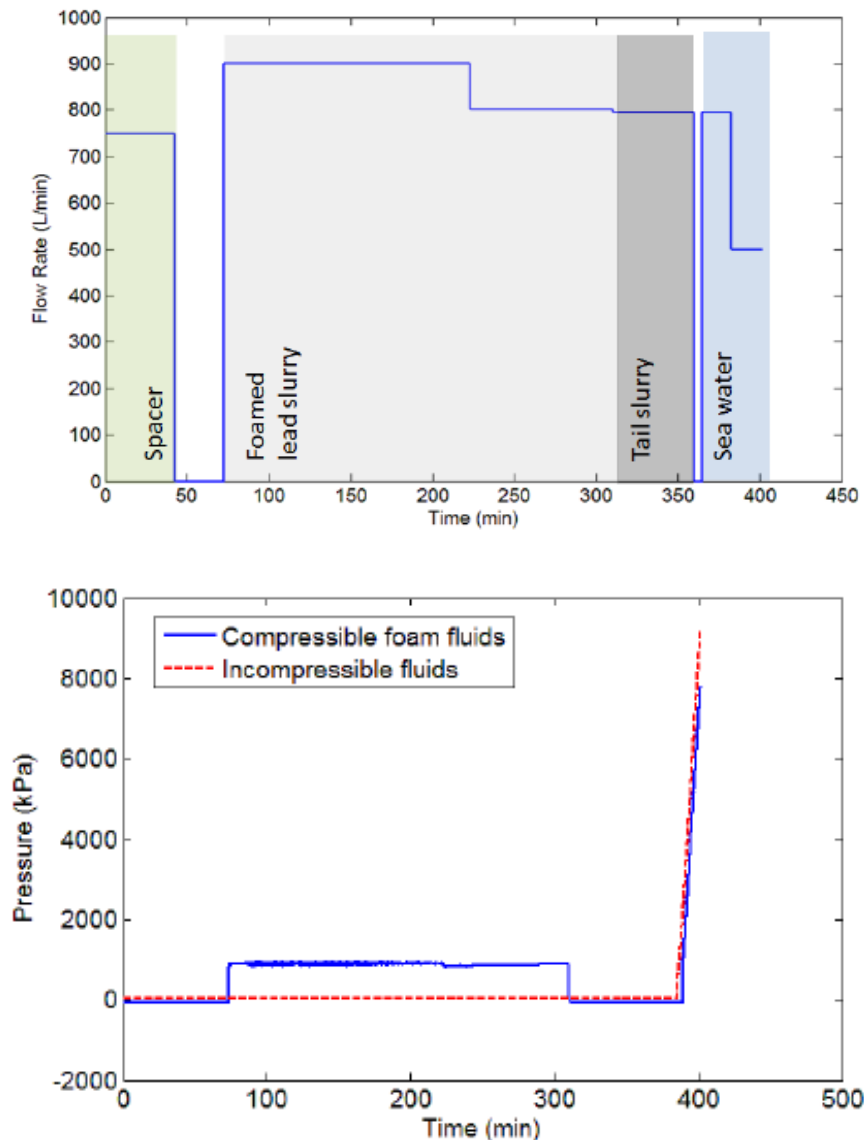


Figure 2-8. Wellhead pressure for foamed and unfoamed cementing operation (Guillot, 2012)

The design of foamed cementing hydraulics requires the same caution as any well cementing operation concerning the operation window in pore and fracture pressure, and the Hydrostatic Equivalent Pressure (ESD) and Equivalent Circulating Density (ECD) need to be calculated at each step of the cementing operation. Figure 2-9 presents an example for the plot considering the minimum (purple line) and maximum (red line) ECD and maximum hydrostatic pressure (dark blue line). All curves are calculated from the pressure at every depth of the

well. The pore (light blue line) and fracture (green line) gradient are the lower and upper limit for the other curves.

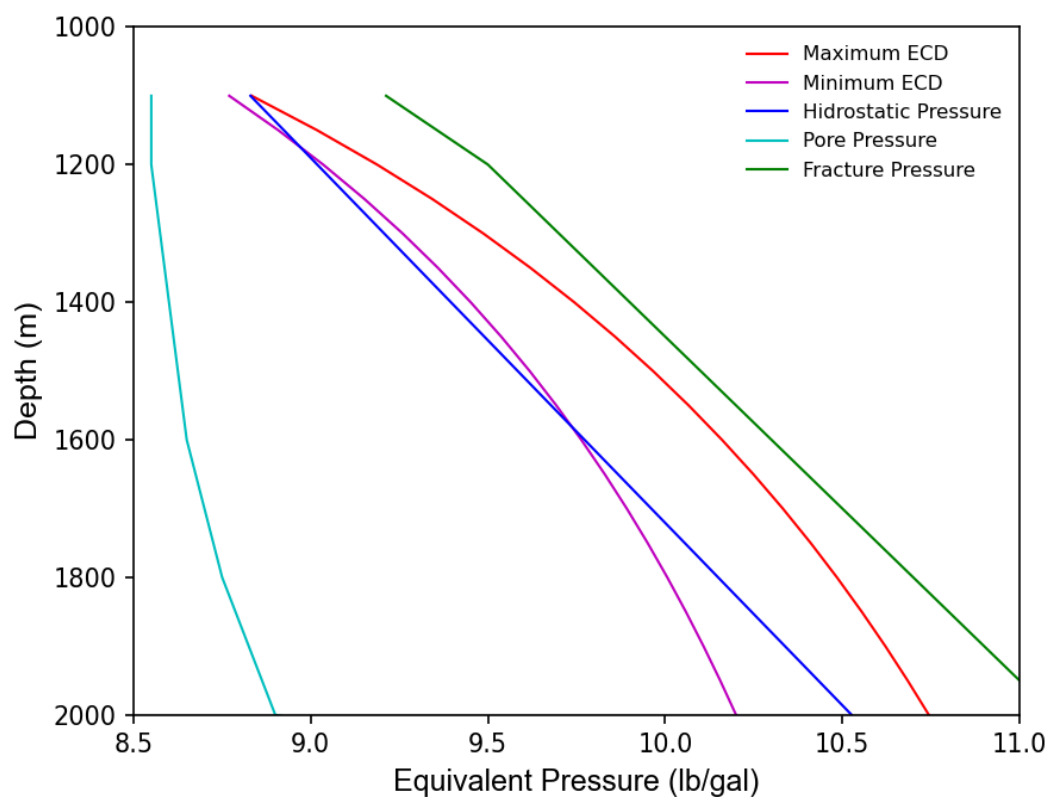


Figure 2-9. Minimum and maximum equivalent circulation density (ECD)

Since the foamed cement has a high compressibility, the calculations of the pressure, density and temperature profile require specific software. The approach for modeling the flow considers dispersed bubbly flow and relative motion between the gas and liquid phases may be ignored (Brill, 1999). Foamed cement density and rheology will vary during the placement due to the U-tube effect, well diameter profile and heat transfer (pressure and temperature changes), and these effects need to be considered in calculating the nitrogen volume to be injected.

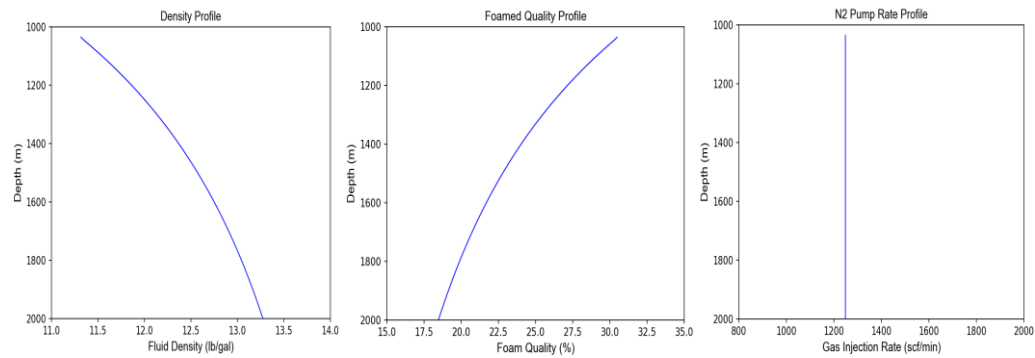
The placement method commonly used in field operations receives a brief description (API, 2010).

- i. Constant nitrogen ratio: downhole density and gas volumetric fraction (typically known as foam quality) will vary in the well annular profile due to pressure and temperature changes along the well.
- ii. Constant density: the nitrogen ratio will vary continuously during the

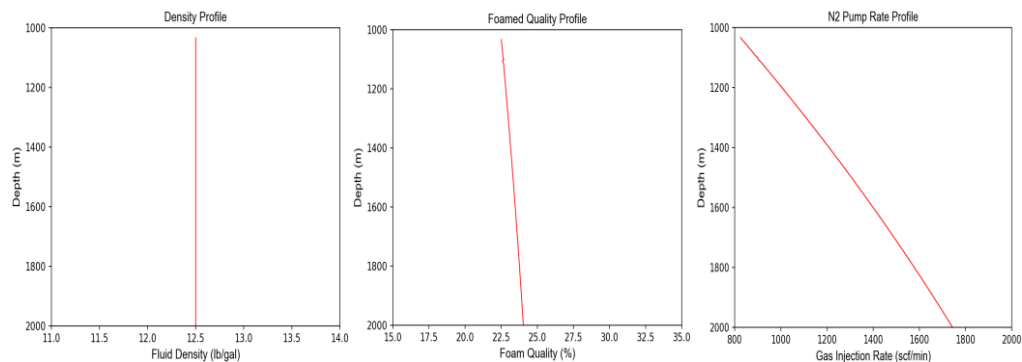
pumping of the cement slurry. The gas volumetric fraction increases with depth in the annulus to maintain a constant density.

- iii. Staged nitrogen ratio (hybrid): steps of constant nitrogen ratio to reduce the changes in density in an annulus. It is considered a simpler operational method for injecting nitrogen because the gas rates are kept constant for each stage.

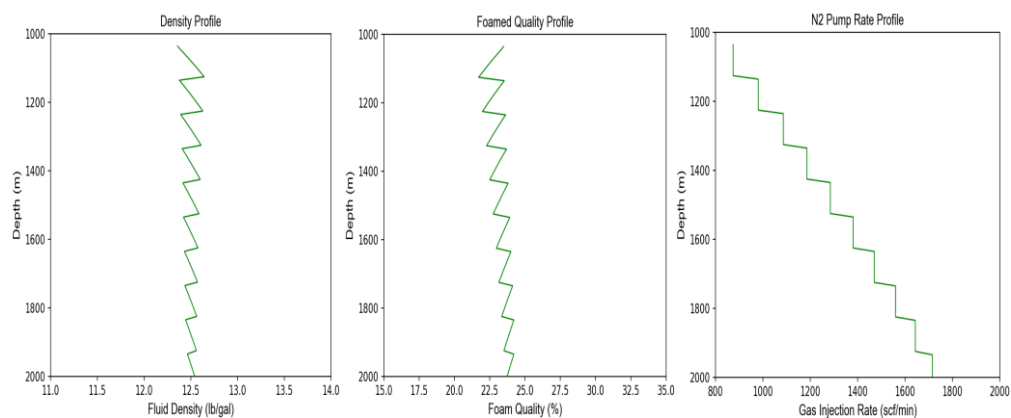
An example for how the density, foam quality and N<sub>2</sub> pump rate profiles change along the well according to the placement method is shown in Figure 2-10. The example comprises a cemented casing in a deepwater well in water depth of 1000m and a casing shoe set in 2000m and considers a base slurry density of 16,2 ppg (unfoamed) with a target density (foamed cement slurry) of 12,5 ppg.



a) Constant nitrogen ratio



b) Constant density



c) Staged nitrogen ratio (hybrid with 10 stages)

Figure 2-10. Foamed cementing pumping strategies

If a constant nitrogen ratio (nitrogen pump rate over liquid pump rate) is applied, the density at the uppermost part of the cement column will be lower than at the bottom and shall not reduce the hydrostatic pressure underbalance with the exposed formations. (API, 2010). In addition, the density of foamed cement should not be lower than the drilling fluid to maintain a density hierarchy.

The final top of cement obtained in annulus after the final placement will change due to thermal expansion of the slurry (Guillot, 2012). Since the

temperature at the end of displacement is not at equilibrium with the adjacent formation, the increase in temperature makes the gas expand and consequently the foamed cement. Figure 2-11 shows an example of an expansion occurring in the cement after the placement, which needs to be considered in cementing design. In some cases, the Top of Cement (TOC) may be increased by over 100 meters.

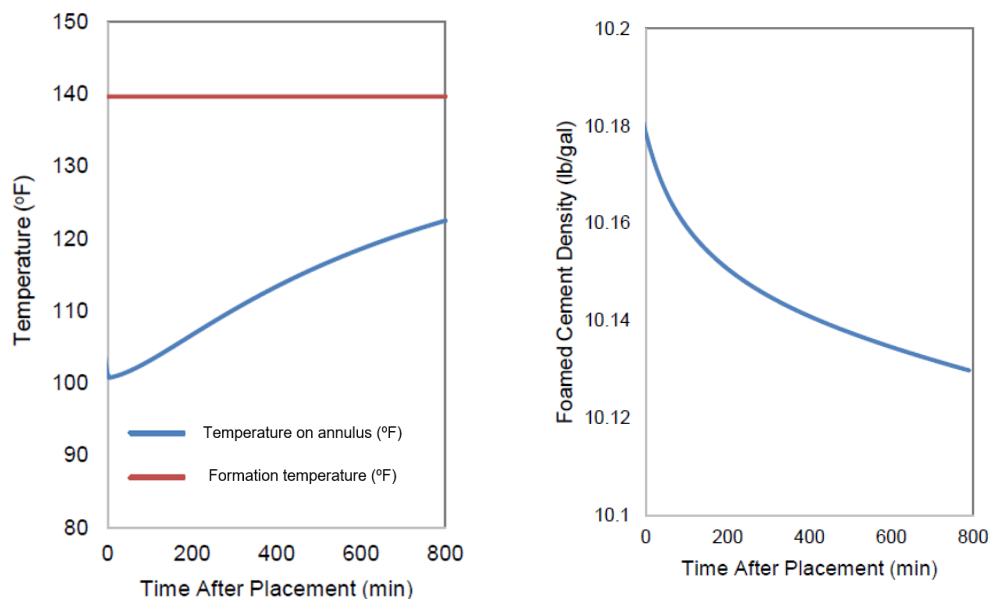


Figure 2-11. Evolution of top of cement after placement due to temperature equilibrium with the adjacent formations (adapted from Guillot, 2012)

Another characteristic of the design of foamed cement jobs is flexibility for defining optimized properties of the cement slurry, such as free-fluid, fluid loss control and gas migration control, which are challenging in extended cement slurries and dry-blended specialty cements. Also, the rheology of dry-blended cement with hollow glass microspheres are typically high (API, 2018) and must be reduced with dispersant agents, however the dispersion is usually limited to avoid sedimentation and free-fluid.

The density of foamed cement can also be performed by increasing the density of the base cement slurry and the bottomhole gas concentration, or conversely, decreasing the base cement slurry density and bottomhole gas concentration. This characteristic provides better flexibility and may be optimized on a case-by-case basis.

Further, it is relevant to mention certain characteristics in the cement evaluation of foamed cements. Such as the evaluation on any cement sheath, sonic and ultrasonic cement bond logging tools can measure signal attenuation of acoustic waves, however ultralight and foamed cements may indicate similar behavior as the drilling fluid (Kalyanraman, 2021). This attenuation can make it difficult to accurately assess the quality and integrity of the cement bond.

### 2.3.

#### **Modeling of multiphase flow for well cementing operations**

Drilling fluids and cement slurries present strong non-Newtonian behavior due to its complex natures – polymer and particle content, emulsification, etc. Generalized Newtonian fluid is highly used to describe drilling and cementing hydraulics due to its ability to consider yield stress and shear thinning behavior (Nelson, 2006; API, 2010). The Generalized Newtonian equation is shown in Eq. 2-1 and the flow curves in Figure 2-12.

$$\bar{\tau} = \eta(\dot{\gamma}) \cdot \bar{\dot{\gamma}} \quad (2-1)$$

Where the quantities are defined as:

$\bar{\tau}$  – Shear Stress Tensor

$\bar{\dot{\gamma}}$  – Shear Strain Tensor

$\eta(\dot{\gamma})$  – Generalized Newtonian Viscosity

Table 2-2 summarizes some of the most common constitutive models considered in the modeling of well cementing operations, and Figure 2-12 presents shear-stress versus shear-rate plots of each constitutive model.

Table 2-2. Generalized Newtonian Fluid Models

Constitutive Model	Viscosity Equation
Newtonian	$\eta = K$
Pseudoplastic	$\eta = K \cdot  \dot{\gamma} ^{n-1}, n < 1$
Dilatant	$\eta = K \cdot  \dot{\gamma} ^{n-1}, n > 1$
Bingham Plastic	$\eta = \frac{\tau_y}{ \dot{\gamma} } + K, \text{ if } \tau > \tau_y$ $\infty, \text{ if } \tau < \tau_y$
Plastic (Herschel-Bulkley)	$\eta = \frac{\tau_y}{ \dot{\gamma} } + K \cdot  \dot{\gamma} ^{n-1}, \text{ if } \tau > \tau_y$ $\infty, \text{ if } \tau < \tau_y$

Where the following parameters are defined as:

K – Consistency index

n – Behavior Index

$\tau_y$  – Yield Stress

$|\dot{\gamma}|$  – Magnitude of the Shear-rate

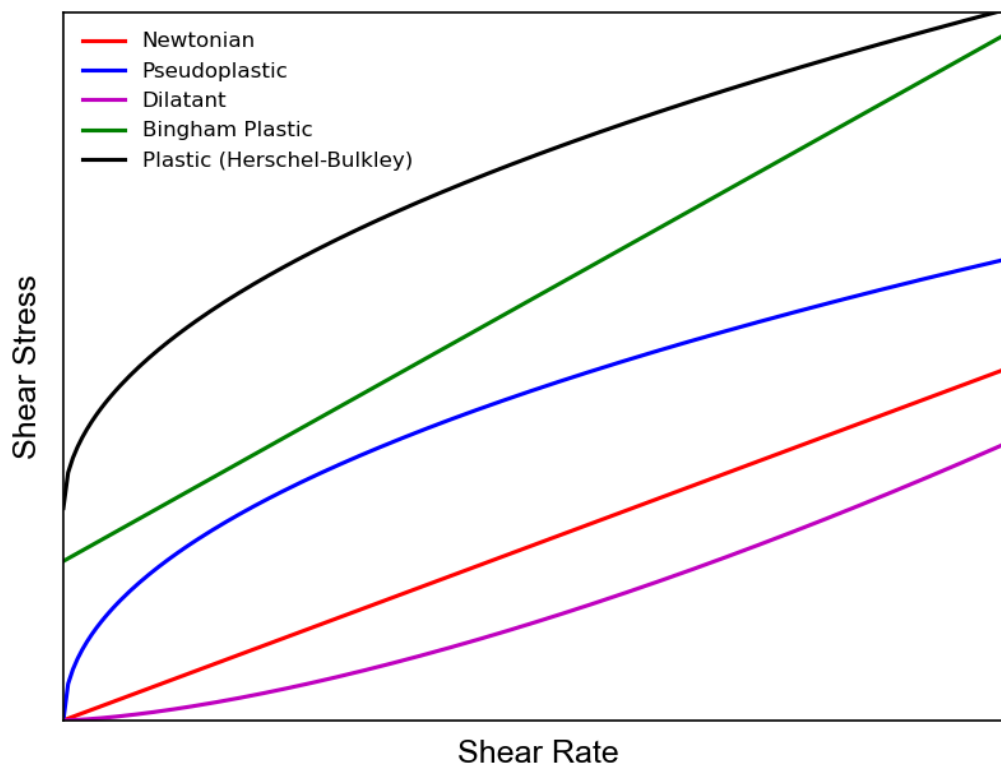


Figure 2-12. Generalized Newtonian models (adapted from Barnes)

Becker (2003) proposed a generalized form to the fluids involved in well drilling and cementing including two-phase fluids such as involved in foam drilling and foam cementing. The model is usually called Generalized Herschel-Bulkley (GHB) model, initially proposed by R.Y. Ofoli (1987) and provides a better accuracy in predicting the yield point in yield stress fluids with shear thinning behavior, especially in complex behaviors. Eq. 2-2 describes the viscosity of the GHB fluid – the Herschel-Bulkley will be recovered by considering  $m = 1$ .

$$\eta(\dot{\gamma}) = (\tau_y^m + K \cdot |\dot{\gamma}|^n)^{\frac{1}{m}} \cdot |\dot{\gamma}|^{-1} \quad (2-2)$$

In addition to the selection of proper constitute model for the fluids, the design process requires the evaluation of the proper displacement efficiency of the drilling fluid by the spacers and cement slurries. The upwards displacement in the annulus depends on several parameters and it shall be analyzed in barrier placement with proper simulation tools (API, 2010; Nelson, 2006). Casing centralization, density contrast, frictional pressure contrast and annular velocity influence directly the ability to evenly displace the existing drilling fluid in annulus and all of them should be kept as high as possible to allow a better drilling fluid removal. Table 2-3 summarizes some of the causes and consequences of impaired displacement in annulus, which may appear stand-alone or combined in a real cementing operation.

Table 2-3. Causes and consequences of an impaired displacement process.

<b>Causes of failed cement jobs</b>	<b>Impairment effect in removal</b>
Critically eccentric annulus	Channeling of the cement sheath in annulus Microannulus due to poor drilling fluid removal
Insufficient annular velocity to displace high yield stress or gelled drilling fluids	Insufficient displacement of gelled or unconditioned drilling fluid Microannulus due to poor drilling fluid removal. The viscosity hierarchy may not be obtained or be low in such situations.
Low or negative density contrast and/or low frictional pressure contrast (a consequence from a low viscosity contrast)	High contamination of the cement slurry and/or channeling of the cement sheath in annulus Microannulus due to poor drilling fluid removal
Low effectiveness of spacers and preflushers	Patches of drilling fluid in cement sheath, unbonded cement in casing and formation and contaminated cement slurry Microannulus due to poor drilling fluid removal
Excessive circulating pressure in low-fracture formations and/or narrow annulus	Insufficient top of cement and/or compromised effective displacement rate

Flow curves plots are useful in identifying the minimum effective pump rate to obtain a positive frictional pressure contrast in the annular flow. An example is shown in Figure 2-13 where the minimum pump rate recommended for displacing the fluid after the top plug would be around 3.0 bbl/min for a concentric annulus and laminar flow.

In this example both fluids are non-Newtonian and the Herschel-Bulkley model adopted parameters are described in Table 2-4 below. Geometric parameters for this example consider a hydraulic diameter of 0.10m.

Table 2-4. Parameters for example of frictional pressure contrast

	<b>Fluid 1</b>	<b>Fluid 2</b>
$k$	4.0 Pa.s <sup>n</sup>	1.0 Pa.s <sup>n</sup>
$n$	0.5	0.8
$\tau_y$	4.0 Pa	4.0 Pa

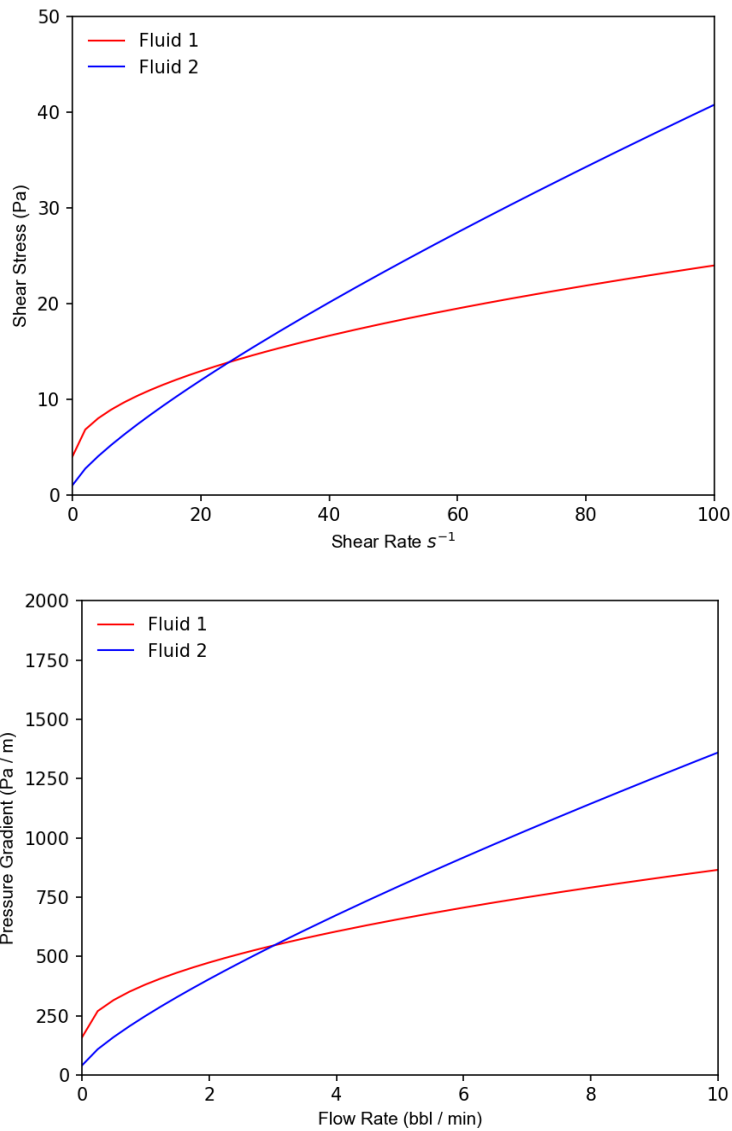


Figure 2-13. Flow curve of displaced (Fluid 1) and displacing fluid (Fluid 2) in annular flow. Top: Shear-rate and shear stress curve; Bottom: Flow rate and pressure gradient curve (for specific geometry).

Eccentricity will also play an important role in the flow regime in the annulus. As the standoff ratio (SOR) decreases (the casing becomes more eccentric on the

wellbore) the flow in the wide side of the annulus becomes turbulent with a lower pump rate than the one considered in the concentric average calculations. In the same way, the necessary pump rate to obtain turbulent flow in the narrow side of the annulus will be higher (Nelson, 2006).

Figure 2-14 shows an example for the case where the Eccentric Reynolds Number ( $(N_{Re1})_{ecc}$ ) – Reynolds number in the wide side of the annulus - is plotted as a function of the SOR for three different behavior indexes ( $n$ ) in generalized Newtonian fluids.

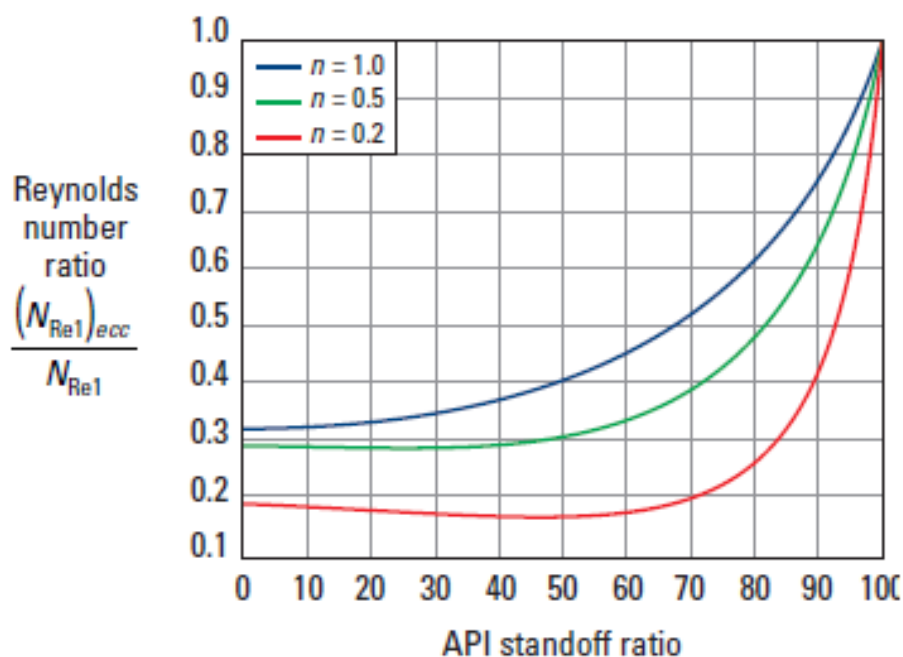


Figure 2-14. Minimum normalized Reynolds number for a turbulent flow in wide side of annulus (Nelson, 2006)

In the development of well cementing technology throughout the years, the use of computational tools for the simulation of displacement in an annulus replaced certain “rule of thumbs” for the design parameters and well geometry. Foroushan (2021) reviews several modeling approaches in well cementing displacement simulations that solve the continuity and momentum equations in multiphase flow considering geometric and constitutive models for the fluids involved. Maleki and Frigaard (2017) and Gomes and Carvalho (2015) present developments of laminar and turbulent flow in small-gap eccentric annuli from

lubrication theory, which reduces the 3-dimensional problem flow to a 2-dimensional flow with reduced computation cost.

3D Computational fluid dynamics (CFD) models have also been reported in literature to simulate well cementing in complex applications where the simplified models have limitations, such as variable size annulus (Skadsem, 2018; Vargas, 2022), perforate wash and cementing operations (Phadke et al, 2020) and in highly eccentric annuli with and without rotation (Enayatpour, 2017). The CFD modeling provides good flexibility to a wide range of analysis, however, the computational cost increases dramatically (Bois et al, 2023).

For foamed cementing applications, Garcia Jr. (1993) developed an algorithm for estimating the transient pressure and density profiles during foamed cementing operations by considering plug flow. Hanachi et al (2018) developed a similar model and in addition a small gap 2D asymptotic model for foamed cementing simulations in an eccentric annular space that considers the foamed cement as a one-phase compressible fluid and a miscible mixture model. The model succeeds to consider the compressibility of foamed cement and the change in rheological parameters with pressure changes. The study from Hanachi (2018) indicated density-driven instabilities in the flow, however, the best practice should ensure the foamed cement density will be higher than the one of the displaced drilling fluids and spacers, which doesn't occur in one of the cases analyzed.

## **2.4.**

### **General remarks and gaps from literature review**

The stability, state properties and the rheological behavior of foamed fluids (spacers and cement) are quite complex, and many studies have been performed with different conclusions. Another conclusion is that the application involving foamed fluids needs to be known to allow a better selection of correlations to be considered. For instance, a high-quality foam applied as a drilling fluid during drilling will behave very differently than a low-quality cement slurry in an annular flow. The methods for measuring foams at high temperature and high pressure are still limited for obtaining accurate data for well cementing applications.

As for the design of foamed cementing operations, the prediction of pressure

and temperature profiles are vital for the correct placement in the annulus. The modeling strategy of the foamed cement as a single, one-phase compressible fluid with dispersed bubbles has been successfully applied throughout many decades for the estimation of such pressure and temperature profiles without considering the modeling of interfaces during the flow.

However, the displacement flow modeling with interface capturing usually doesn't consider the compressibility of foamed fluids, because of the complexity and computational cost involved. Different approaches may be applied, but few have been performed and published in the literature. At this point, no work related to fully 3 dimensional models to account for large-gap and high eccentricity in the annular domain for compressible and non-Newtonian fluids flow were encountered in the literature.

### 3

## Methodology - Development of numerical model

### 3.1.

#### Problem Definition and Governing Equations

A schematic section of the well appears in Figure 3-1. The annular space starts filled with the fluid to be displaced (*Fluid 1*) and the displacing fluid (*Fluid 2*) enters from the bottom with a constant mass flow rate ( $\dot{m}_{in}$ ) which represents a condition during the well cementing at a certain depth. At the top of the section, the boundary condition consists of a known absolute pressure ( $P_{out}$ ). The geometric parameters are the radius of the well ( $R_w$ ), radius of the casing ( $R_c$ ), eccentricity ( $e$ ), length of the section ( $L$ ) and well deviation ( $\beta$ ).

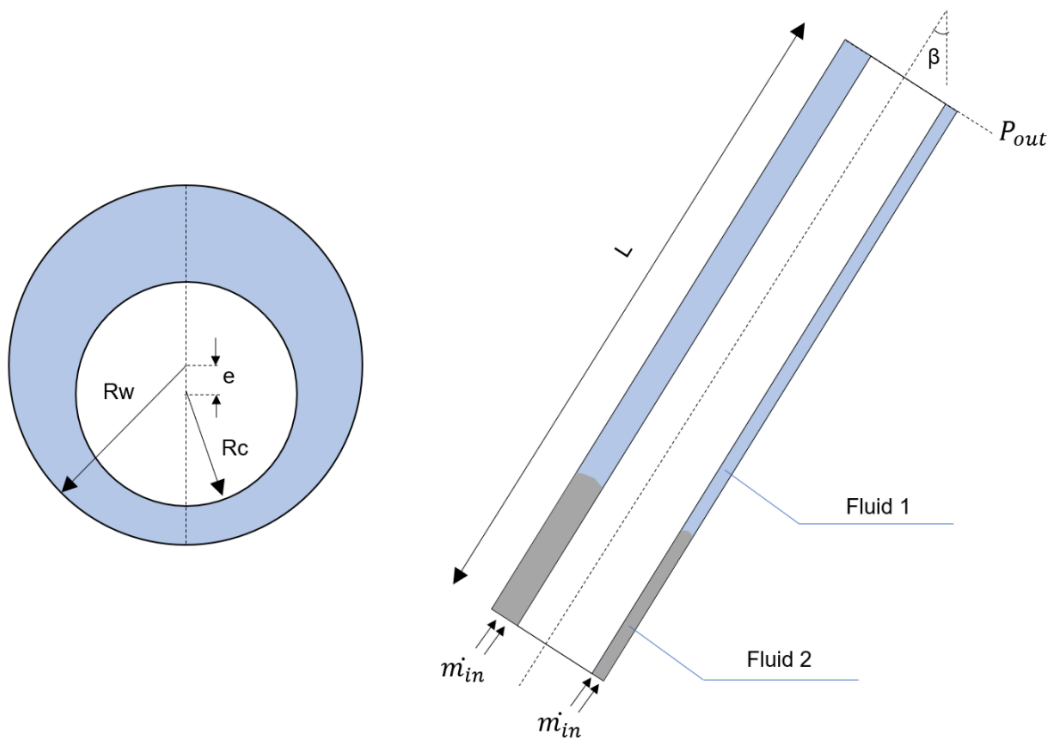


Figure 3-1. Schematic of the simplified geometric and flow model of well cementing

The eccentricity is considered constant and uniform during the flow as a simplifying hypothesis. Therefore, the eccentricity changes along the well central

axis due to (i) nonuniformities and tortuosity of the wellbore; (ii) casing deflection between centralizers; and (iii) buoyancy of the casing with the density changes of fluids in the well are not considered in this work and will be addressed in the future work proposals section.

The conservation equations of mass (Eq. 3-1) and momentum (Eq. 3-2) are applied using the Volume of Fluid (VoF) method for modeling the multiphase flow problems. This method solves the governing equations averaging constitutive and flow properties of the phases for each control volume, while the volumetric phase concentration is calculated through the mass conservation for each phase (Eq. 3-3). The sum of the volume fractions must be equal to the unity ( $\sum_1^n \alpha_i = 1$ ).

$$\frac{\partial(\rho)_{mix}}{\partial t} + \nabla \cdot (\rho \vec{U})_{mix} = 0 \quad (3-1)$$

$$\frac{\partial(\rho \vec{U})_{mix}}{\partial t} + \nabla \cdot (\rho \vec{U} \vec{U})_{mix} = -\vec{\nabla} p + \rho_{mix} \cdot \vec{g} + (\nabla \cdot \bar{\tau})_{mix} + F_{st} \quad (3-2)$$

$$\frac{\partial(\alpha_i \rho_i)}{\partial t} + \nabla \cdot (\alpha_i \rho_i \vec{U}) + \nabla \cdot (\rho_i U_c \alpha_i (1 - \alpha_i)) = 0 \quad (3-3)$$

Where the variables are defined as:

$\alpha_i$  – Volumetric concentration of Fluid i

$\rho_i$  – Density of Fluid i

$\vec{U}$  – Velocity vector

$p$  – Pressure

$\bar{\tau}$  – Shear stress tensor

$F_{st}$  – Surface Tension Force

According to the VoF method implementation, the multiphase flow may be modeled as an effective homogeneous fluid moving with the velocity field  $\vec{U}$  and having pressure  $p$  (cell-averaged), and the fields may be described as per Eq. 3-4, Eq. 3-5, and Eq. 3-6.

$$\rho_{mix} = \sum_{i=1}^2 \alpha_i \cdot \rho_i \quad (3-4)$$

$$(\rho \vec{U})_{mix} = (\rho_{mix} \cdot \vec{U}) \quad (3-5)$$

$$(\rho \vec{U} \vec{U})_{mix} = (\rho_{mix} \cdot \vec{U} \vec{U}) \quad (3-6)$$

Thus, with no slip between the two phases, the homogeneous approach allows solving a single momentum equation (Eq. 3-2). Consequently, in the displacement simulations, the compression or expansion of the compressible fluid will slow down or accelerate the incompressible one in the domain, or vice-versa.

The third term in Eq. 3-3 follows from the interface compression method (Okagaki et al, 2021), which is implemented to give a negative diffusion coefficient, compressing the volume fraction profile in the direction normal to the fluid interface; hence, it can prevent interface dispersal due to numerical diffusion and maintain boundedness and conservation of the phase fraction, since both phases share the same velocity field.

Outside the interface region, this term will always be null because of a null concentration gradient. The term  $U_c$  is defined as follows Eq. 3-7 and  $C_\alpha$  is a user-defined parameter that  $0 \leq C_\alpha \leq 1$ .

$$U_c = U_2 - U_1 = \min(C_\alpha |\vec{U}|, |\vec{U}|) \cdot \frac{\nabla \alpha}{|\nabla \alpha|} \quad (3-7)$$

The term  $(\nabla \cdot \vec{\tau})_{mix}$  will be discussed in the 3.1.2 section and follows from the constitutional model selection and the term  $F_{st}$  will be discussed in 3.3 section regarding surface tension modeling. The equations of state and constitutive equations used must describe fluids with pressure and shear stress dependent behavior.

### 3.1.1.

#### Equation of state

In the case of the energized/foamed fluids, the density dependence with pressure follows from the definition of the volumetric fraction ( $\varphi$ ), shown in Eq. 3-8, and the gas-liquid volumetric injection ratio at standard conditions ( $GLR_{STD}$ ) in Eq. 3-9.

$$\varphi(p, T) = \frac{Q_{gas}}{Q_{gas} + Q_{liq}} \quad (3-8)$$

$$GLR_{STD} = \frac{Q_{gas,STD}}{Q_{liq}} \quad (3-8)$$

Since the mass flow rate of the gas of a certain pumped volume of foamed cement does not change with pressure and temperature during the operation, then Eq. 3-10 holds for every position of the foamed cement.

$$\dot{m} = (\rho_{gas}(P, T) \cdot Q_{gas}) = (\rho_{gas,STD} \cdot Q_{gas,STD}) \quad (3-10)$$

Consequently, the expression in Eq. 3-11 may be derived for the gas volumetric fraction  $\varphi$  at a given pressure and temperature.

$$\varphi(p, T) = \frac{\left( \frac{\rho_{gas,STD}}{\rho_{gas}(p,T)} GLR_{STD} \right)}{\left( 1 + \frac{\rho_{gas,STD}}{\rho_{gas}(p,T)} GLR_{STD} \right)} \quad (3-11)$$

With the volume fraction of the gas in the foamed fluid for every pressure and temperature, an Equation of State (EoS) can be derived by considering the foam as a stable, single-phase fluid with a weighted density of the base fluid (unfoamed cement slurry or spacer) and the inert gas (small, dispersed bubble hypothesis). The expression for the density of the foamed fluid can be expressed by Eq. 3-12:

$$\rho_{foam} = (1 - \varphi) \cdot \rho_{liq} + \varphi \cdot \rho_{gas}(p, T) \quad (3-12)$$

Where  $\rho_{liq}$  is the density of the base liquid fluid and  $\rho_{gas}(p, T)$  is the gas density at a given pressure and temperature condition.

For isothermal flow and considering that the injected gas behaves as an ideal gas, the quality  $\varphi$  and the density  $\rho_{foam}$  can be obtained in Eq. 3-13 and Eq. 3-14.

$$\varphi(p) = \frac{\left( GLR_{STD} \cdot \frac{P_{STD}}{p} \right)}{\left( 1 + GLR_{STD} \cdot \frac{P_{STD}}{p} \right)} \quad (3-13)$$

$$\rho_{foam} = (1 - \varphi) \cdot \rho_{liq} + \varphi \cdot \rho_{gas,STD} \cdot \left(\frac{p}{p_{STD}}\right) \quad (3-14)$$

### 3.1.2.

#### Constitutive transport model

Finally, the constitutive equation for energized/foamed fluids is obtained by establishing dependence to the rate of strain-rate tensor ( $\bar{\bar{D}}$ ) given by Eq. 3-15 and the strain rate magnitude ( $|\dot{\gamma}|$ ) in Eq. 3-16.

$$\bar{\bar{D}} = (1/2) \cdot (\overline{\nabla \vec{U}} + \overline{\nabla \vec{U}^T}) \quad (3-15)$$

$$|\dot{\gamma}| = \sqrt{2} \cdot |\bar{\bar{D}}| \quad (3-16)$$

The stress tensor ( $\bar{\bar{\tau}}$ ) may then be computed as per Eq. 3-17 for laminar flow where  $\eta(\dot{\gamma}, \varphi)$  is the viscosity function with strain rate and gas fraction dependence.

$$\bar{\bar{\tau}} = 2\eta(\dot{\gamma}, \varphi)\bar{\bar{D}} \quad (3-17)$$

Now the treatment for the viscous stress term in the momentum equation may be explicated as per Eq. 3-18 below. It is important to mention that this method considers a well-behaved mixing of the two fluids (i.e. the dilution between the two fluids provides averaged density and rheological properties).

$$(\nabla \cdot \bar{\bar{\tau}})_{mix} = 2[\alpha_1 \eta_1(\dot{\gamma}) + \alpha_2 \eta_2(\dot{\gamma}, \varphi)](\nabla \cdot \bar{\bar{D}}) \quad (3-18)$$

The first viscosity function type considered in this work is a direct adjustment in the parameters of generalized Newtonian constitutive models, such as the Herschel-Bulkley model given by Eq. 3-19.

$$\eta(\dot{\gamma}, \varphi) = \begin{cases} \frac{\tau_y(\varphi)}{|\dot{\gamma}|} + K(\varphi) \cdot |\dot{\gamma}|^{n-1}, & \text{if } \tau > \tau_y(\varphi) \\ \infty, & \text{if } \tau < \tau_y(\varphi) \end{cases} \quad (3-19)$$

Where the parameters  $K$  and  $\tau_y$  relate to the 3-parameter base fluid Herschel-Bulkley model ( $K_0, \tau_{y,0}, n$ ) according to Eq. 3-20 (Ducloué, 201), where  $\varphi$  is the gas volumetric fraction as Eq. 3-13.

$$\begin{cases} k(\varphi) = K_0 \cdot \left(\frac{5+3\varphi}{5-2\varphi}\right)^{\frac{n+1}{2}} \cdot (1-\varphi)^{\frac{1-2n}{2}} \\ \tau_y(\varphi) = \tau_{y,0} \sqrt{\frac{(1-\varphi)(5+3\varphi)}{5-2\varphi}} \end{cases} \quad (3-20)$$

The second implemented model for the foam viscosity considers a direct relation of the apparent viscosity of the foamed fluids with gas fraction ( $\varphi$ ) dependance, with the form of Eq. 3-21.

$$\eta(\dot{\gamma}, \varphi) = \begin{cases} \left(\frac{\tau_0}{|\dot{\gamma}|} + K_0 \cdot |\dot{\gamma}|^{n-1}\right) f(\varphi), & \text{if } \tau > \tau_y(\varphi) \\ \infty, & \text{if } \tau < \tau_y(\varphi) \end{cases} \quad (3-21)$$

Where  $f(\varphi)$  is a function determined by fitting experimental data or theoretical models. In this work the function described in Eq. 3-22 (Rosenbaum, 2019) was used in the simulations.

$$f(\varphi) = 1 + 1958\varphi + 15810\varphi^2 \quad (3-22)$$

The choice of the models proposed by Ducloué et al (2014) and used by Hanachi (2018) and Rosenbaum et al (2019) in the studies conducted in this dissertation comes from a relatively straightforward way to adjust the viscosity model of energized fluids with variation of the gas fraction. However, any other correlation  $\eta(\dot{\gamma}, \varphi(p, T))$  can be implemented if sufficient data is available.

### 3.2.

#### Finite Volume Method and Interface capturing modeling of multiphase flow

The finite volume method became relevant in solving fluid flow due to its high flexibility for solving the coupled partial differential equations. The basis for the method discretizes the physical domain into discrete elements and integrate the partial differential equations and transform into balance equations. In the following step, the variation of the scalars and vectors in the element are approximated with the use of interpolation profiles to allow the integration and then transform the balance equations into a system of algebraic equations (Moukalled, 2015). Consequently, this method maintains the conservation of all scalars and vector fields over the domain (Figure 3-2).

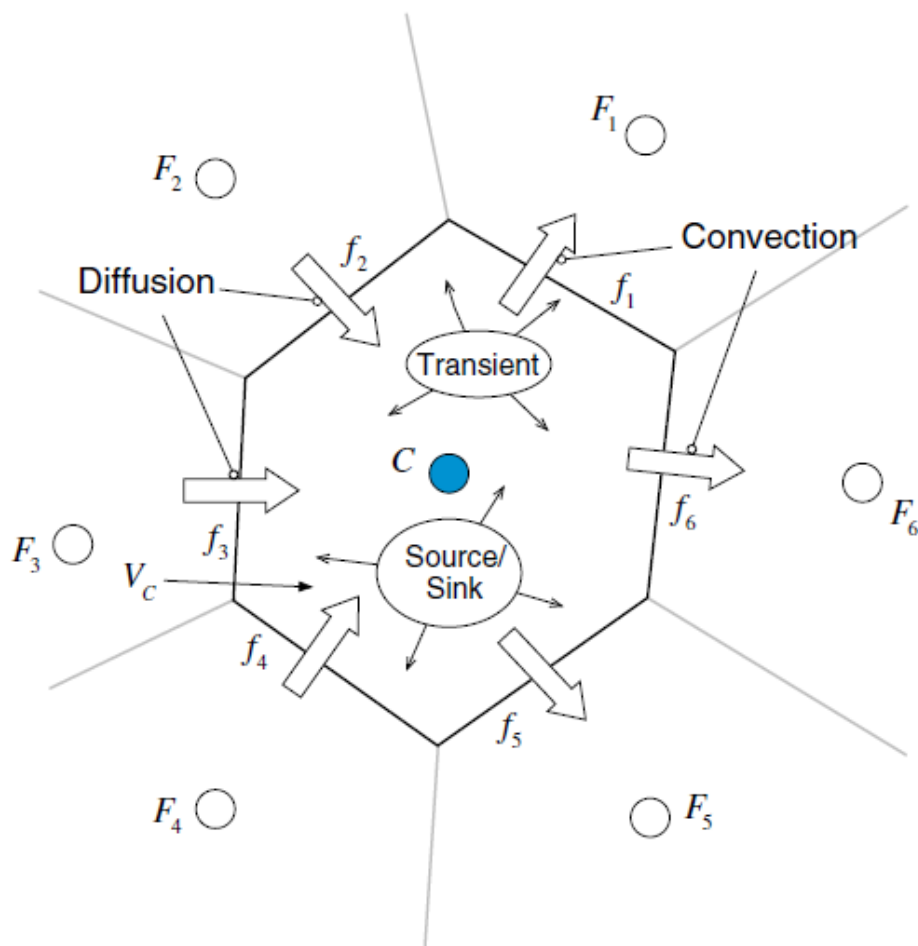


Figure 3-2. Conservation of a quantity “F” in a discrete element

The integration process of transforming the partial differential equation (Eq. 3-23) into balance equations (Eq. 3-24) for a scalar  $\Phi$  over an element  $C$  with

$nb(C)$  boundaries is described.

$$\underbrace{\frac{\partial(\rho\Phi)}{\partial t}}_{\text{transient term}} + \underbrace{\nabla \cdot (\rho\vec{U}\Phi)}_{\text{convective term}} = \underbrace{\nabla \cdot (\Gamma^\Phi \nabla\Phi)}_{\text{diffusion term}} + \underbrace{Q^\Phi}_{\text{source term}} \quad (3-23)$$

$$\underbrace{\int_t^{t+\Delta t} \int_{V_C} \frac{\partial(\rho\Phi)}{\partial t} \cdot dV dt}_{\text{transient term}} + \underbrace{\int_t^{t+\Delta t} \left( \sum_{f \sim nb(C)} \left( \int_f (\rho\vec{U}\Phi)_f \cdot d\vec{S} \right) \right) dt}_{\text{convective term}} =$$

$$\underbrace{\int_t^{t+\Delta t} \left( \sum_{f \sim nb(C)} \left( \int_f (\Gamma^\Phi \nabla\Phi)_f \cdot d\vec{S} \right) \right) dt}_{\text{diffusion term}} + \underbrace{\int_t^{t+\Delta t} \left( \int_{V_C} Q^\Phi dV \right) dt}_{\text{source term}} \quad (3-24)$$

The selection of the interpolation functions and time step for the integration will be covered later. The discretized system of algebraic equations is solved using, for instance, a geometric-algebraic multi-grid method (GAMG) considering the boundary conditions of the flow.

To track the interface between the fluids, the Volume of Fluid (VoF) method solves the volume fraction equation (Eq. 3-3) in each cell to describe the shape and position of the interface. In Figure 3-3 the schematics shows the interface reconstruction from the volume fraction of the fluids (represented in different colors) with a piecewise linear method (PLIC) fraction field distributed in the domain is defined in advance.

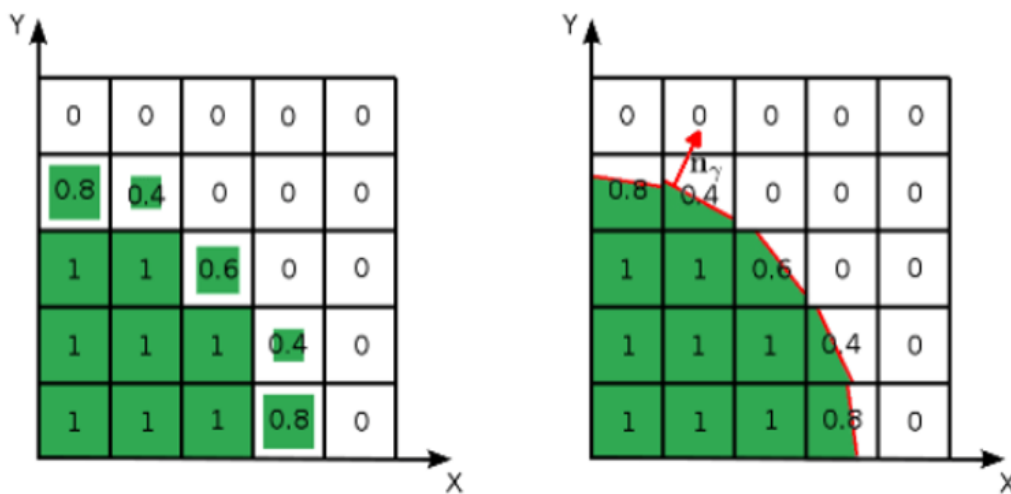


Figure 3-3. VOF interface (Source: NPTEL)

To the research described in this dissertation, the OpenFOAM® (Open-Source Field Operation and Manipulation) toolbox was selected to perform the development of the models for foamed cementing. The development of OpenFOAM started in 1993 for solving computational fluid dynamics (CFD) in open-source C++ code, which allows relatively simple user customization.

The conservation equations solvers with the FVM method are implemented in the software with a large library of classes and functions for selecting interpolating functions, discretization schemes and linear solvers.

The Solver *compressibleInterFoam* can solve fluid flow scalar and vector fields involving multiphase, non-isothermal and compressible flow. However, the libraries for Equations of State and constitutive models are not fully complete and there are no implemented options of fluids comprising bubbly liquids and shear rate dependent viscosity. To account for this limitation, the methodology described by Westermaier (2020) succeeds in including the assessment of shear rate in the solver, which contributes to describing in detail the editing of the C++ files. A summary of the process of the compilation of the new solver with new equations of state and viscosity models is shown in Figure 3-4, and further details may be found in Appendix A.

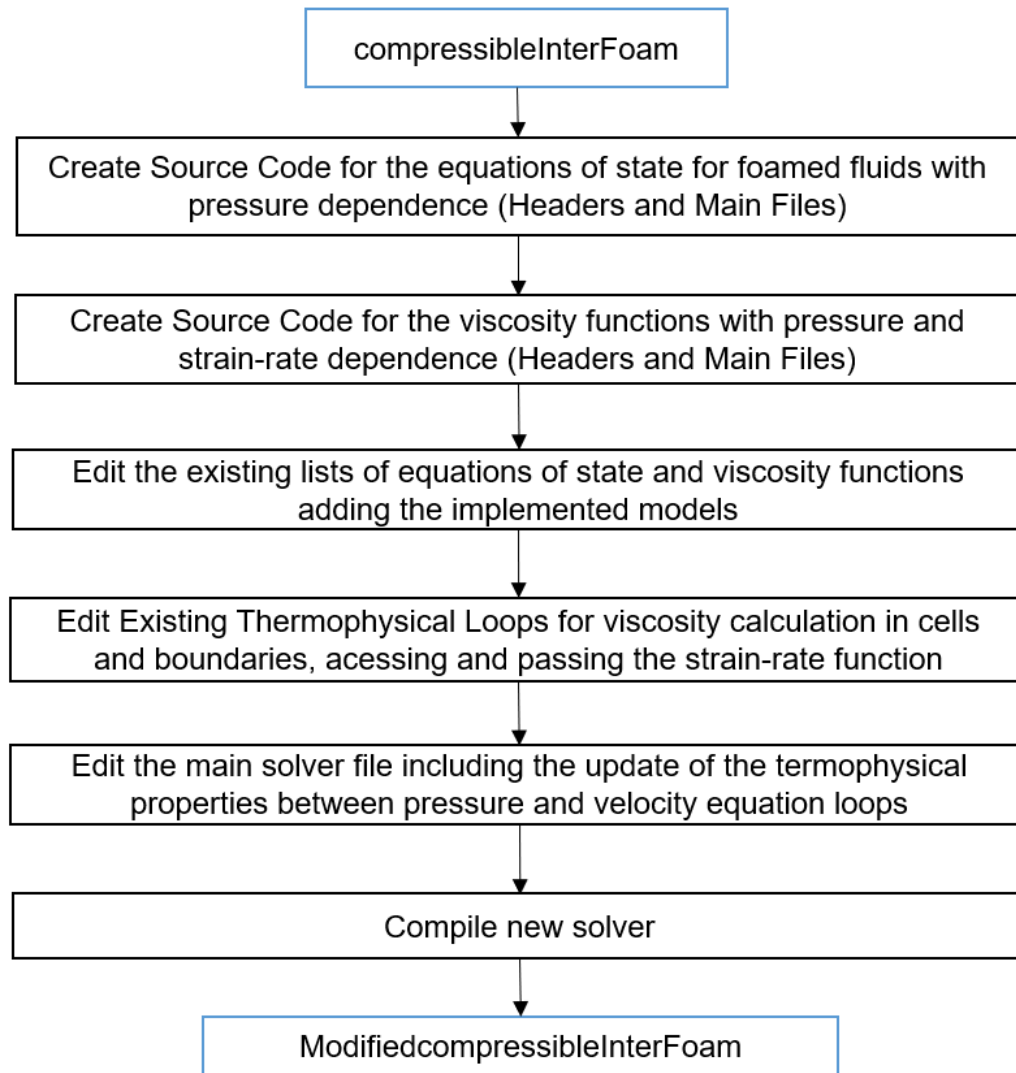


Figure 3-4. Workflow development of a custom solver in OpenFOAM with new equations of state and viscosity functions

The energy conservation equation – not included in the studies conducted – is implemented in the solver, and it can be included if data from the fluid flow in annulus and temperature dependence for physical properties are available. However, in this research, the fluid flow is considered isothermal.

### 3.3.

#### Surface tension modeling

The effect of surface tension in VOF model implemented in OpenFOAM®

from the model proposed by Brackbill (1991) that considers a continuous surface force (CSF) which provides a volumetric representation of surface tension and replaces a discontinuous interface for a continuous region where the forces are non-zero (Figure 3-5). The surface tension force calculated at each cell is given by Eq. 3-25 below.

$$F_{st} = \sigma \cdot \kappa \cdot \nabla \alpha_1 \quad (3-25)$$

The curvature at the interface is calculated by Eq. 3-26 below.

$$\kappa = -\nabla \cdot \hat{n} \quad (3-26)$$

Where  $\hat{n}$  is the unit normal vector at the interface given by Eq. 3-27.

$$\hat{n} = \frac{\nabla \alpha_1}{|\nabla \alpha_1| + \delta} \quad (3-27)$$

Where  $\delta = \frac{10^{-8}}{\bar{V}_e}$  a parameter used to avoid computation errors and  $\bar{V}_e$  is the average volume of the cells to account for non-uniform meshes.

Finally,  $\hat{n}$  is corrected to account for the contact angle at the wall as Eq. 3-28.

$$\hat{n} = \hat{n}_w \cdot \cos\theta + \hat{t}_w \sin\theta \quad (3-28)$$

Where the normal ( $\hat{n}_w$ ) and tangential ( $\hat{t}_w$ ) components to the wall and the contact angle ( $\theta$ ) at the wall are considered.

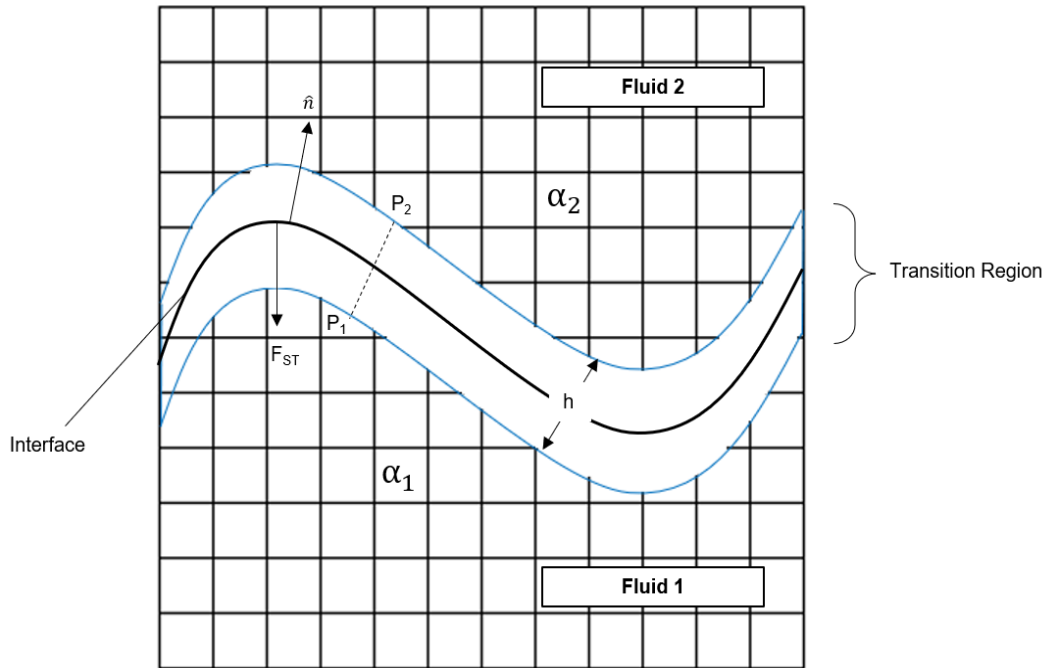


Figure 3-5. Surface tension modeling as a CSF (adapted from Brackbill, 1991)

### 3.4.

#### Numerical schemes, discretization, and boundary conditions

##### 3.4.1.

#### Geometry Discretization

The physical domain discretization follows as described.

For the concentric case, a 2-dimensional geometry may be used to simplify the model considering the symmetry of the flow in the azimuthal and radial direction. A section of 6 degrees was used to represent the geometry as Figure 3-6 and Figure 3-7, discretized in the Z direction (well axis, axial direction) and X direction (radial direction of the well) with different internal and external radii. Regarding Figure 3-6, OpenFOAM needs the geometry in the Y direction for consistency of the code implemented, but no transport will occur in this direction. A geometric progression function produces a refinement near the internal and external walls. The symmetry planes are represented in the Y (azimuthal) axis.

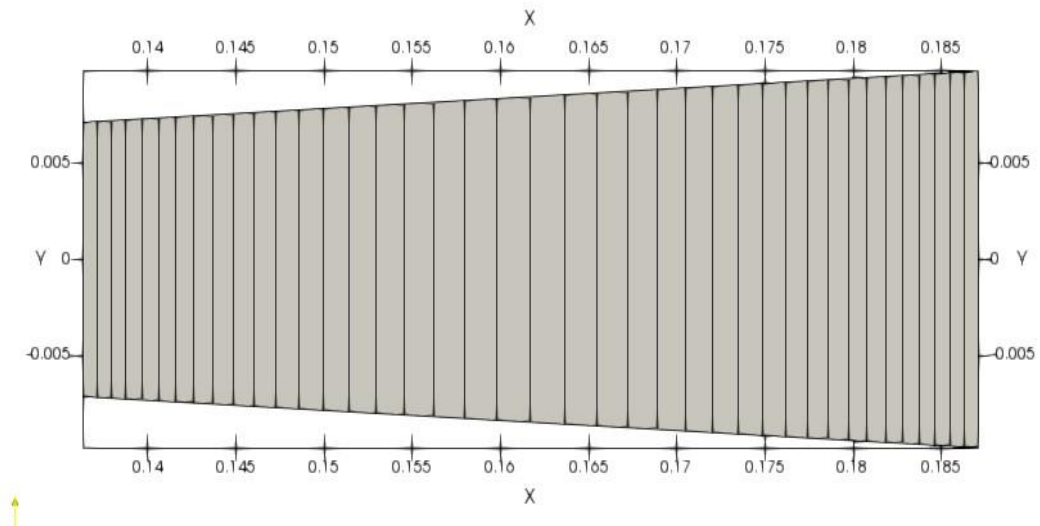


Figure 3-6. Basic mesh of the concentric case ( $Z$  normal)

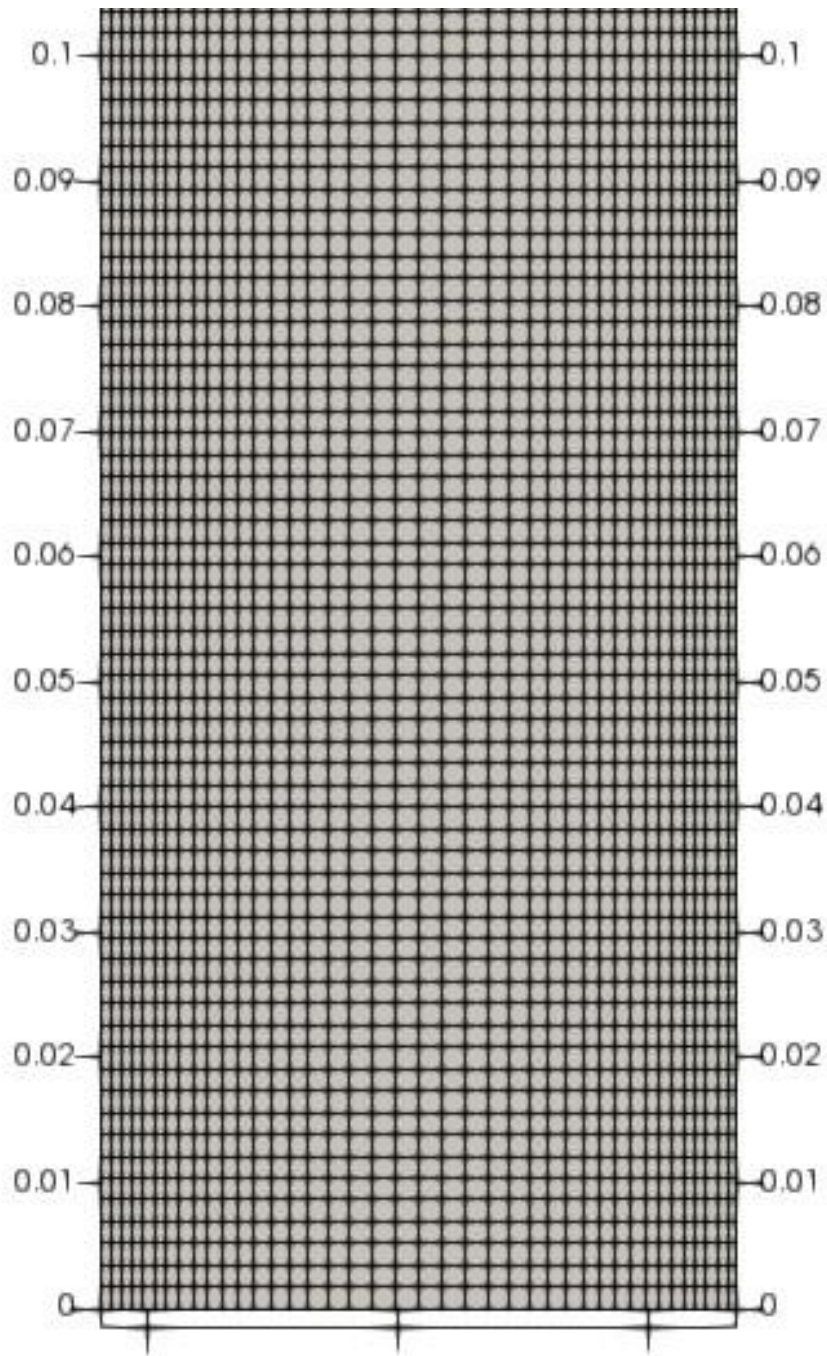


Figure 3-7. Basic mesh of the concentric cases (Y direction normal)

The boundary surfaces described in Figure 3-8 for the 2D model represents the concentric cases to be run (null eccentricity). Still, the same nomenclature of surfaces is applied in the 3D geometry.

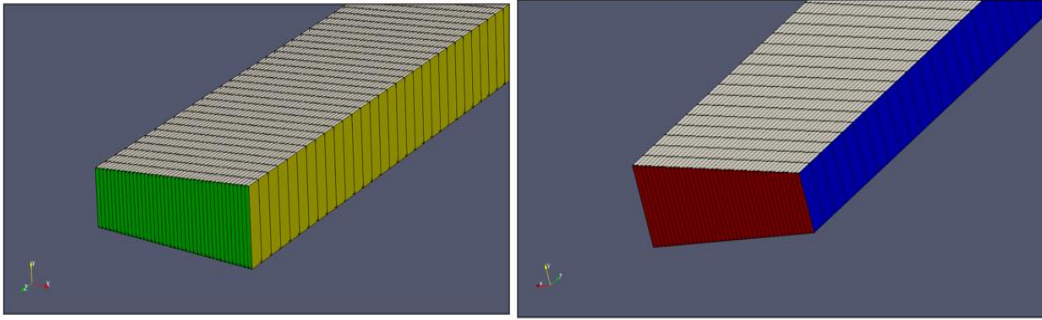


Figure 3-8. Boundary surfaces for 2D simulations. (Green: Inlet; Yellow: External wall; White: Symmetry; Blue: Internal wall; Red: Outlet)

In the 3-dimensional eccentric case the geometry considers a non-zero eccentricity between the casing and the wellbore, and Figure 3-9 shows the discretization executed. A structured mesh is considered which refines in the narrow region, also considering a geometric progression function in the radial direction.

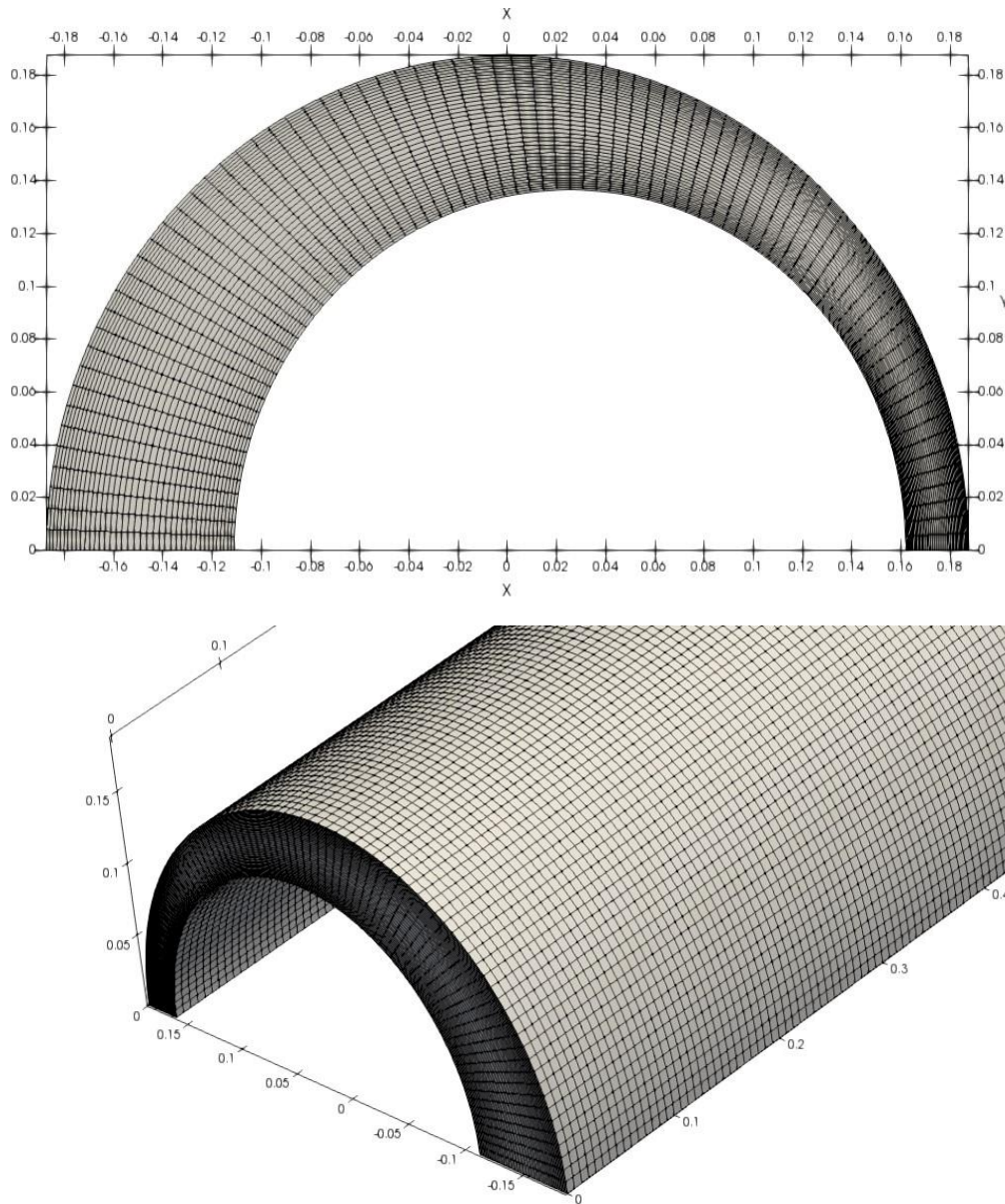


Figure 3-9. 3-dimensional discretization (eccentric cases)

Discretization is important for the interface capturing, and the mesh quality parameters (element aspect ratio, skewness, and orthogonality) are important to avoid convergence difficulties and the precision in the solution. The mesh discretization and quality properties are shown in Table 3-1 and

Table 3-2 for the 2D and 3D simulations.

The selection of the mesh for the parametric simulations considered the test and validation cases with exact solutions for single fluid simulations and to ensure adequate capturing of the interface with the VoF method. In the X-direction, 40

elements showed proper agreement with representing the shear-surface in the velocity profile for non-Newtonian fluids, as will be shown in section 4.1. The Y-direction represents the discretization in the azimuth (around the circumference) and 80 elements were selected to minimize the aspect ratio of the elements. The Z-direction represents the direction of the principal flow and the discretization considered the minimizing of the aspect ratio of elements and the trade-off with computational efficiency.

Table 3-1. Mesh discretization

<b>Mesh discretization</b>	<b>2D mesh</b>	<b>3D mesh</b>
<b>X discretization</b>	40	40
<b>Y discretization</b>	2	80
<b>Z discretization</b>	800	600
<b>Total number of elements</b>	64.000	1.920.000

Table 3-2. Mesh quality properties for hexahedral elements

<b>Mesh discretization</b>	<b>2D mesh</b>	<b>3D mesh</b>
<b>Max Aspect Ratio</b>	8.82	7.15
<b>Non orthogonality</b>	1.11	1.13
<b>Max Skewness</b>	0.127	0.156

Where the quality parameters are described as follows.

- Aspect ratio: Relation between the longest edge of the element over the shortest edge. The best practices consider values below 10.
- Non-orthogonality: Angle between the normal face vector between two elements and the vector connecting the two centroids.
- Skewness: Deviation between the angles in two faces in the elements and the straight angle.

### 3.4.2.

#### Boundary conditions

Inlet:

At inlet, a constant mass flow rate is specified ( $\dot{m}_{in}$ ) that generates a uniform velocity profile given by Eq. 3-29, where  $\hat{k}$  is the unit vector in well axial direction (Z-axis). As the displacing fluid (*Fluid 2*) enters the annulus, the pressure changes due to the density contrast of the two fluids in the domain, and consequently the inlet density and the inlet velocity are modified. Thus, the constant mass flow rate represents the consideration of a constant liquid pump rate of cement slurry at surface conditions, and a constant gas mass flow rate added to the cement slurry.

$$\vec{U}(x, y, 0) = \frac{\dot{m}_{in}}{\rho_{in} A_{in}} \hat{k} \quad (3-29)$$

Walls:

In the walls (internal and external) the condition applied considers no-slip and no-penetration, which means that all components of the velocity are equal to zero as Eq. 3-30.

$$\vec{U}_{wall} = 0 \quad (3-30)$$

Outlet:

The outlet pressure prescribed corresponds to a reference depth to allow the calculation of the density of the foamed fluids to a particular depth in a well, as Eq. 3-31.

$$p(x, y, L) = P_{out} \quad (3-31)$$

Symmetry Plane:

At the symmetry planes a consideration derived from a Neumann boundary condition specifies the normal derivative ( $\hat{n}_{symmetry}$  as the normal direction) at a boundary to be zero and is shown in Eq. 3-32 and Eq. 3-33. This condition is valid

in the 2-dimensional cases (radial and azimuthal symmetry), and valid in the 3-dimensional cases if the maximum eccentricity of the casing occurs in the gravity direction, which is normally the case when the well deviation profile is well behaved with little tortuosity.

$$\nabla_n p = \hat{n}_{symmetry} \cdot \nabla p = 0 \quad (3-32)$$

$$\nabla_n \vec{U}_i = \hat{n}_{symmetry} \cdot \nabla \vec{U}_i = 0 \quad (3-33)$$

Initial conditions:

The initial velocity in the domain considers the displaced fluid (*Fluid 1*) flowing in the annulus upwards the annular. That is an expected condition when the displacing fluid (*Fluid 2*) enters the annulus. Thus, the velocity and pressure fields are defined as follows in Eq. 3-34 and Eq. 3-35 below, and the concentration field that contains the displacing fluid volume fraction given by Eq. 3-36.

$$\vec{U}(t = 0) = \frac{\dot{m}_{in}}{\rho_{in}(t=0)A_{in}} \hat{k} \quad (3-34)$$

$$p(t = 0) = P_{out} + \rho \cdot g \cdot (z - z_{REF}) \cdot \cos\beta \quad (3-35)$$

$$\alpha_2(t = 0) = 0 \text{ for the whole domain} \quad (3-36)$$

### 3.4.3.

#### Numerical Schemes

Transient term: An implicit, First-order Euler Scheme considers as per Eq. 3-37.

$$\frac{\partial(\rho\Phi)}{\partial t} = \frac{(\rho\Phi) - (\rho\Phi)^0}{\Delta t} \quad (3-37)$$

Convective term: The second order upwind was selected to achieve an optimized compromise between numerical stability and avoiding numerical

diffusion. It is therefore more accurate than first order upwind but less stable numerically by considering a correction of the values of flux in the faces from the gradient between the cells. To avoid numerical errors (which can occur if the extrapolated values of the quantity from the gradient exceed the values of neighboring cells), a geometrical correction parameter ( $\delta \leq 1$ ) is usually considered in most software applications (and considered in OpenFOAM), as per Eq. 3-38.

$$(\rho\Phi)_f = (\rho\Phi)_p + \delta \cdot \nabla(\rho\Phi)_p \cdot \Delta r \quad (3-38)$$

Diffusion term: As the diffusion (Laplacian) term is calculated Linear function interpolation with the Divergence Theorem (Eq. 3-23), the gradients of  $\Phi$  and the diffusion coefficient are calculated in the cell faces with linear central differences with neighboring cells.

#### 3.4.4.

#### Herschel-Bulkley Regularization

To avoid the discontinuity in Eq. 3-14 in the viscosity from Yield-stress fluids such as the Herschel-Bulkley model, a regularization parameter is considered to avoid numerical inconsistency and to capture the yield-surface in the flow.

For a non-Newtonian fluid with a flow-behavior index (API 13D), the characteristic shear-rate can be defined as Eq. 3-39, and a characteristic viscosity as Eq. 3-40.

$$\dot{\gamma}_c = \frac{4\dot{U}}{D_h} \frac{(2n+1)}{n} \quad (3-39)$$

$$\eta_c = \frac{\tau_y}{\dot{\gamma}_c} + \frac{k\dot{\gamma}_c^n}{\dot{\gamma}_c} \quad (3-40)$$

In addition, a modified equation (Eq. 3-41) was implemented in the Solver to consider the regularization parameters  $\Omega$  and  $\omega$ .

$$\eta(\dot{\gamma}, \varphi) = \min \left\{ \frac{\tau_y(\varphi)}{\max(|\dot{\gamma}|, \omega)} + K(\varphi) \cdot \max(|\dot{\gamma}|, \omega)^{n-1}, \Omega \cdot \eta_c \right\} \quad (3-41)$$

The implemented values  $\omega = 1e - 9$  and  $\Omega = 500$  ensure that below the critical strain-rate  $\dot{\gamma}_{crit} = \frac{\tau(\dot{\gamma}_c)}{500\eta_c}$  an acceptable maximum viscosity is considered in the Solver. These values follow from related experiences (Vargas, 2022) to balance the benefits between precision and numerical performance of the solution. Figure 3-10 below shows an example of the output of the regularization.

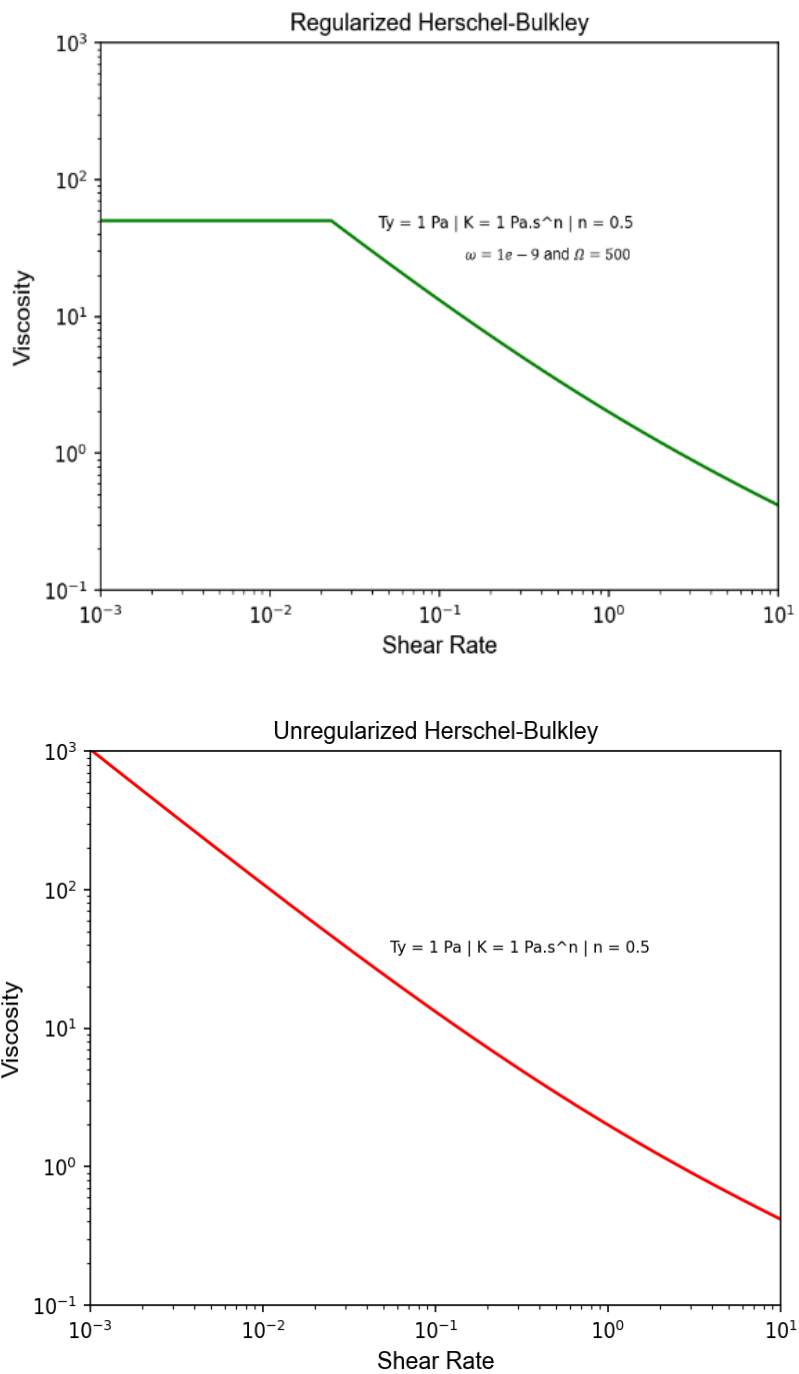


Figure 3-10. Regularized (top) and unregularized (bottom) examples of the Herschel-Bulkley Fluid Model

## 4

### Test cases and parametric analysis

This chapter details the verification and validation process of the models, comparing the model implemented of the foamed fluid flow with:

- Exact solution for single phase flow in axisymmetric annular geometry;
- Experimental data from literature;
- Correlations of single fluid flow in an eccentric annulus;

Further, the chapter details the parameters used in the analysis, from a relevant scenario in deepwater well construction.

#### 4.1.

#### 1D steady-state single-phase flow verification and validation

The code validation was based on solving analytically a 1-dimensional axisymmetric flow for a single-phase generalized non-Newtonian fluid (Power Law and Herschel-Bulkley models), which has known exact solutions for a slot and concentric cylinders (Grinchik and Kim, 1974; Hanks, 1979). The continuity and momentum equation for 1-dimensional steady-state flow simplifies to Eq. 4-1 and Eq. 4-2 and allows integration as an initial value problem, where the shear stress may be calculated at each depth analytically. More details may be found in Appendix B.

$$\dot{m} = \rho(p) \cdot Q(z) = \rho(p) \cdot A_T \cdot U_z(z) \quad (4-1)$$

$$\frac{\partial p}{\partial z} = \rho(p) \cdot g \cdot \cos(\beta) + \frac{\left(\frac{d\tau_w(p)}{dz}\right)}{(D_h/4)} + \left(\frac{\dot{m}}{H.b}\right)^2 \cdot \frac{1}{\rho^3} \cdot \frac{\partial \rho(p)}{\partial z} \quad (4-2)$$

Where  $p(z_0) = P_{out}$ .

The data used in the validation cases are described in Table 4-1 and Table 4-2.

Table 4-1. Fluid and flow parameters for incompressible validation cases

<b>Newtonian Fluid</b>	<b>Power-Law Fluid</b>	<b>Herschel-Bulkley Fluid</b>
$\rho = 1000 \text{ kg/m}^3$	$\rho = 1000 \text{ kg/m}^3$	$\rho = 1000 \text{ kg/m}^3$
$\mu = 0,1 \text{ Pa}\cdot\text{s}$	$k = 0,1 \text{ Pa}\cdot\text{s}^n$	$k = 0,1 \text{ Pa}\cdot\text{s}^n$
-	$n = 0,7$	$n = 0,7$
-	-	$\tau_y = 0,1 \text{ Pa}$
Inlet Velocity = 0,2 m/s		

Table 4-2. Fluid and flow parameters for compressible validation case

$\rho_{liq}$	1000 kg/m <sup>3</sup>
$GLR_{STD}$	5 m <sup>3</sup> -gas / m <sup>3</sup>
$\rho_{gas,STD}$	1,2506 kg/m <sup>3</sup> (N <sub>2</sub> in standard conditions)
$k_{base,liq}$	0.1 Pa·s <sup>n</sup>
$n$	0.7
$\tau_{y,base,liq}$	0,1 Pa
$\dot{m}_{in,liquid}$	0.1723 kg/s
<b>Outlet Pressure (<math>p_{out}</math>)</b>	1 Mpa

The pressure and velocity profiles are presented as follows in Figure 4-1, Figure 4-2 and Figure 4-3 for the incompressible fluid and Figure 4-4 for the compressible fluid. An annular geometry with an outer diameter of 0.37465m and inner diameter of 0.27305m is considered, thus the annular gap is 0.0508m.

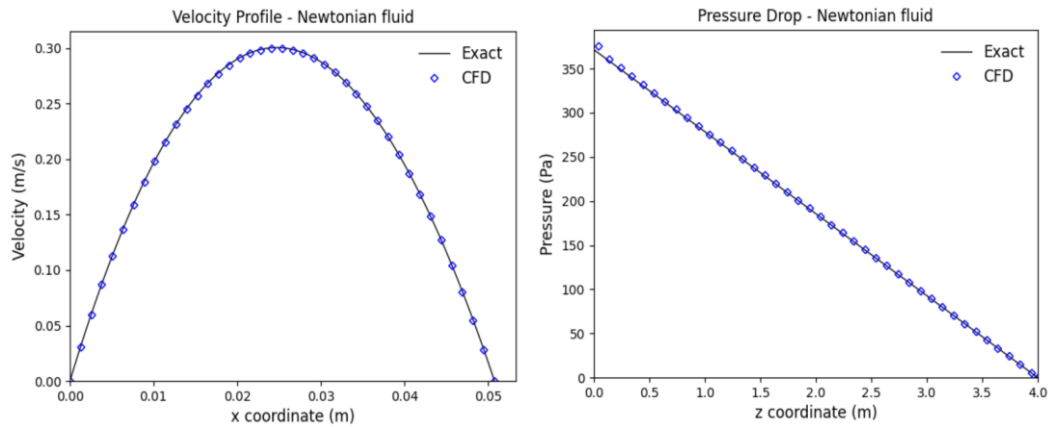


Figure 4-1. Validation case for Newtonian incompressible fluid

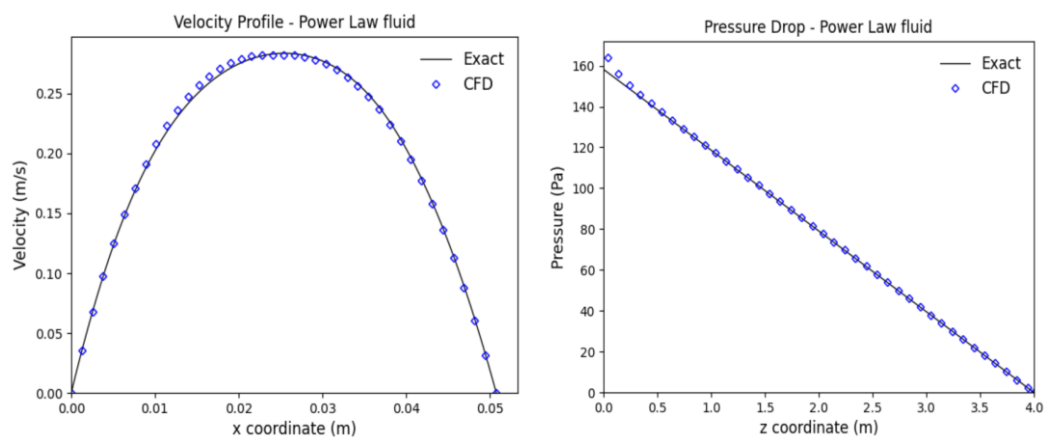


Figure 4-2. Validation case for non-Newtonian (Power-law) incompressible fluid

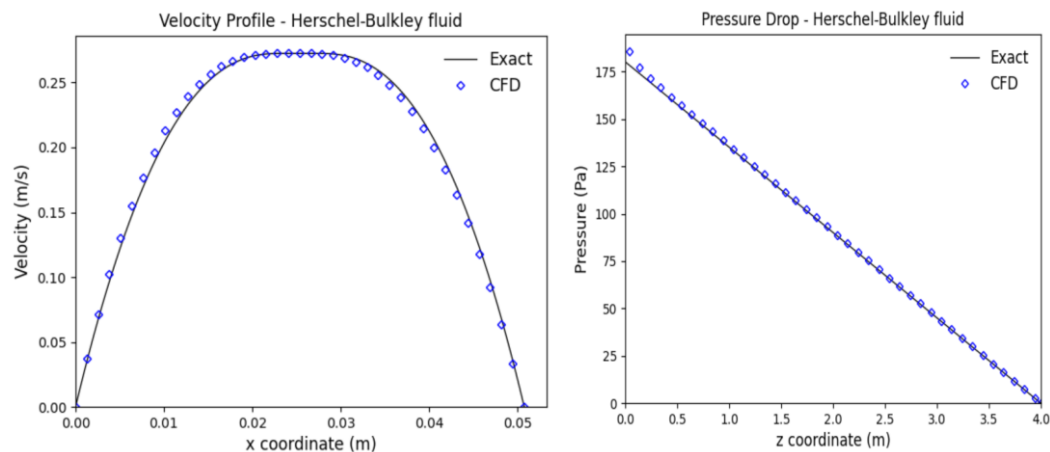


Figure 4-3. Validation case for non-Newtonian (Herschel-Bulkley) incompressible fluid

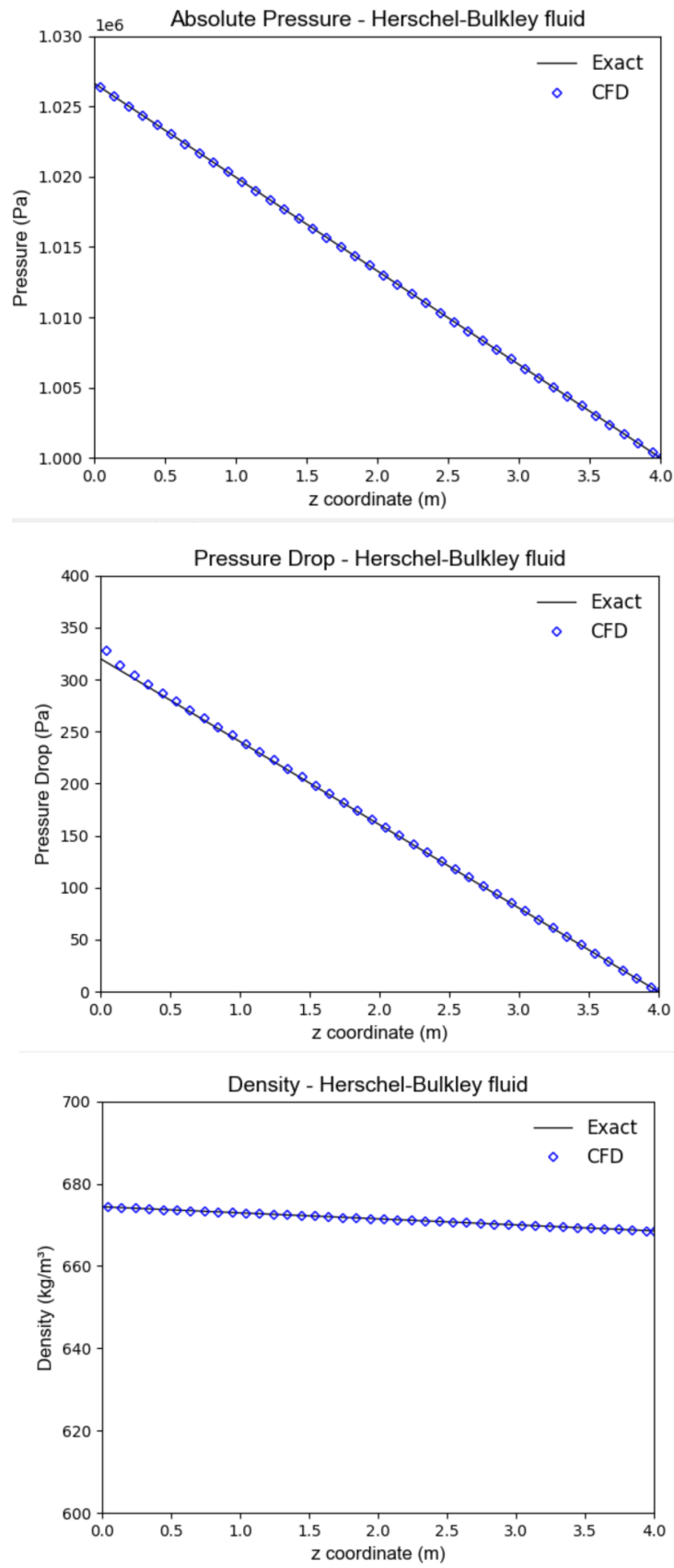


Figure 4-4. Validation case for non-Newtonian compressible fluid

Conversely, the average axial velocity in annulus gets automatically obtained from the mass conservation condition  $\dot{m} = \rho \cdot \bar{U}$ , and it is plotted in Figure 4-5.

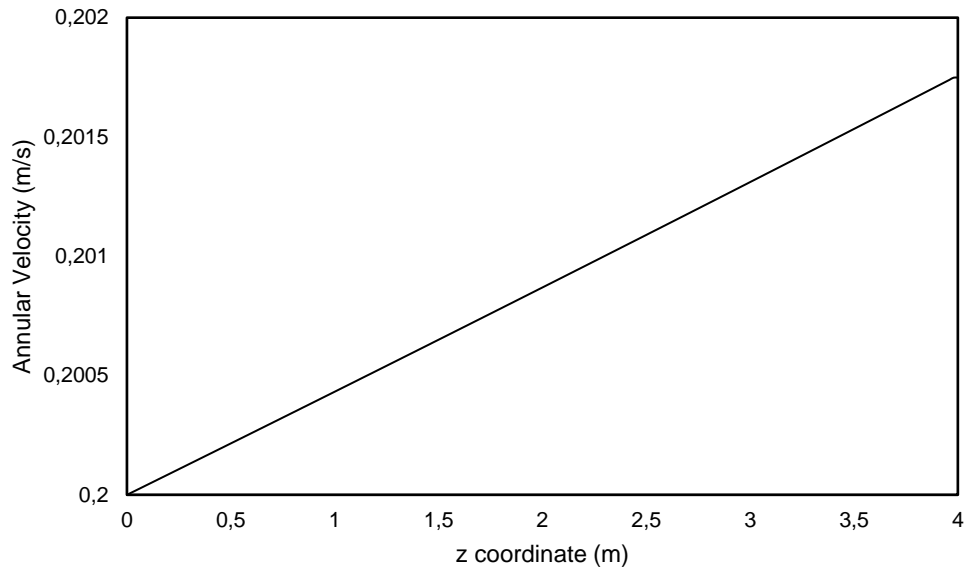


Figure 4-5. Validation case for non-Newtonian compressible fluid – annular velocity

The results indicate that the implemented modeling predicts accurately the velocity, pressure, and density fields from both incompressible and compressible fluids, with Newtonian and Non-Newtonian constitutive models. In the velocity profile in the annular geometry, the yield-surface in the Herschel-Bulkley fluid simulation was properly captured with the selection of the mesh and the regularization parameters. In addition, the pressure loss due to friction matched the exact solution, if the inlet effect is disconsidered.

## 4.2.

### Influence of the eccentricity on hydraulics of foamed fluids

Another relevant analysis concerned the flow in eccentric annuli. Hacıislamoglu and Langlinais (1990) and Bayley (2000) developed correlations to correct the pressure drop in an eccentric annulus as described in Eq. 4-3 for a Power-Law fluid. The same authors proposed a correction for the correlation in yield stress fluids, which is applied in the following comparisons.

$$(\Delta p)_{ecc} = \Delta L \cdot \left[ 1 - 0,072 \cdot \frac{e}{n^*} \cdot \kappa^{0,8454} - 1,5e^2 \cdot \sqrt{n^*} \cdot \kappa^{0,15852} + 0,96 \cdot e^3 \cdot \sqrt{n^*} \cdot \kappa^{0,2527} \right] \cdot (\Delta p)_{conc} \quad (4-3)$$

Where:

$$\kappa = \frac{D_i}{D_o}$$

$$n^* = \frac{n \cdot C_c}{3n(1-C_c)+1}$$

$$C_c = (1-x) \left[ \frac{2n^2}{(1+2n)} x^2 + \frac{2n}{1+2n} x + 1 \right]$$

$$x = \frac{\tau_y}{\tau(\dot{\gamma}_c)}$$

$$\dot{\gamma}_c = \left( \frac{4\bar{U}}{D_h} \right) \cdot \left( \frac{2n+1}{n} \right)$$

To account for this effect in the single-phase flow modeling in this work, 3-dimensional simulations were performed to obtain the velocity profiles in the annulus and the friction pressure across the length of the geometry, in a vertical ( $\beta = 0^\circ$ ) case, where the gravity vector is in the Z-direction only. The data used for the single fluid are the same of the validation cases in Table 4-1 and Table 4-2.

The results of the velocity plots and pressure drop for  $\kappa = 0,7288$  for eccentricities 75%, 50% and 25% are shown in Figure 4-6, Figure 4-7, Figure 4-8 and Figure 4-9.

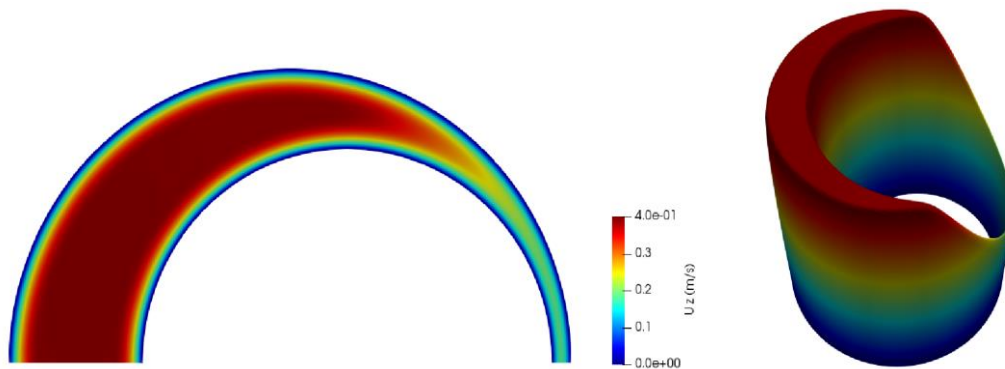


Figure 4-6. Velocity Profile for 75% eccentricity

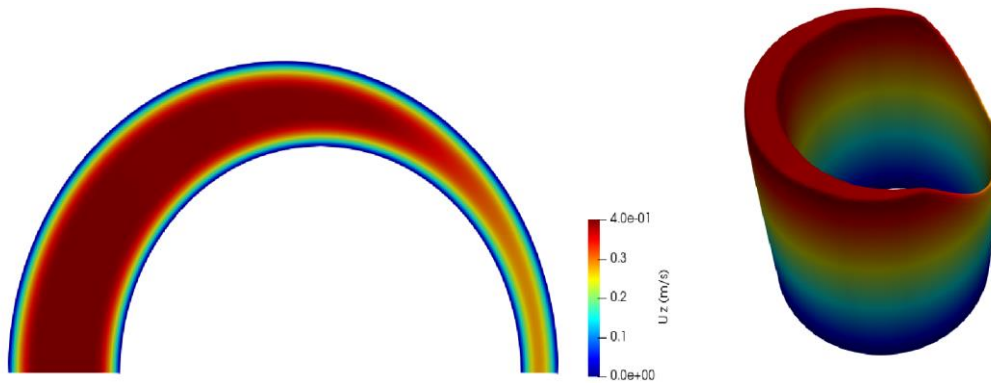


Figure 4-7. Velocity Profile for 50% eccentricity

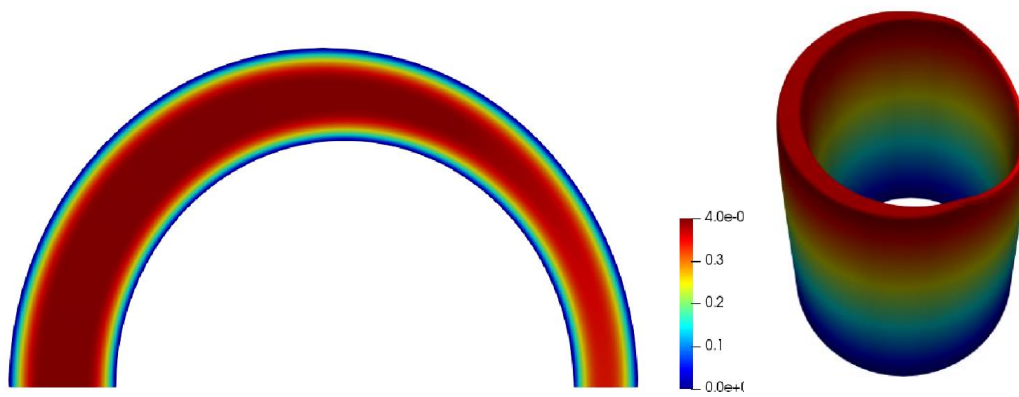


Figure 4-8. Velocity Profile for 25% eccentricity

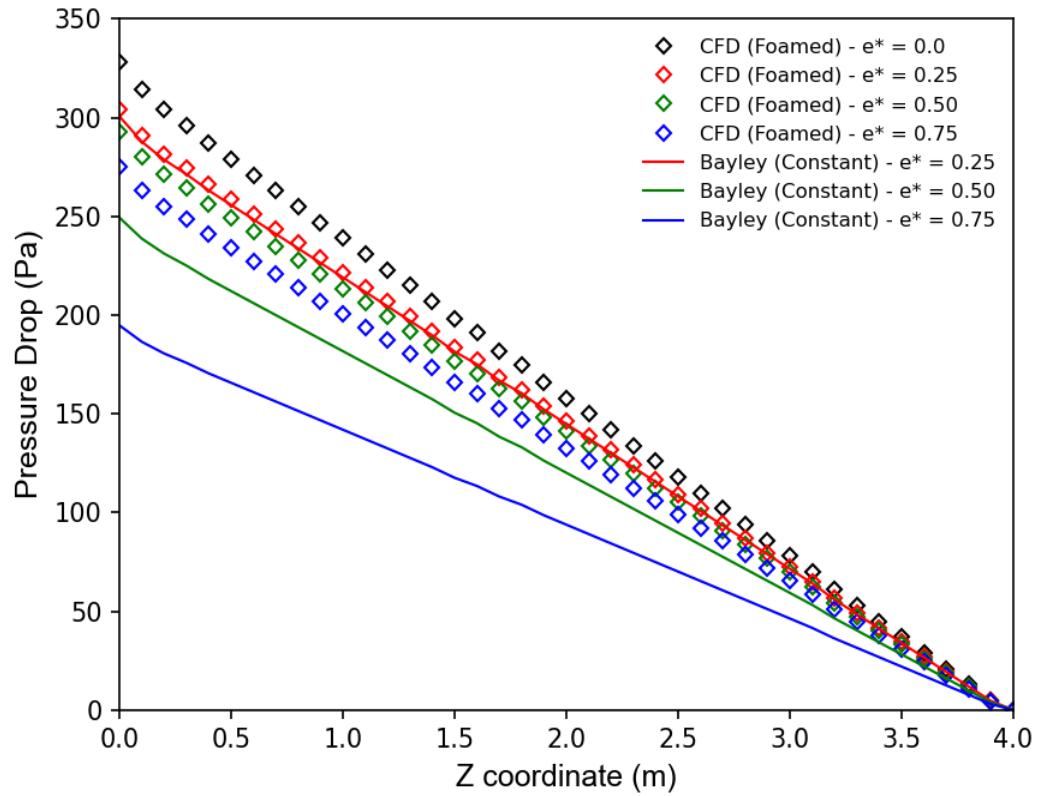


Figure 4-9. Pressure Drop for eccentric, 3D, single fluid simulations.

Compared with a fluid with constant density and rheology, the foamed fluid presented a less-affected friction pressure profile than the constant-density and rheology fluid, as shown in Figure 4-10.

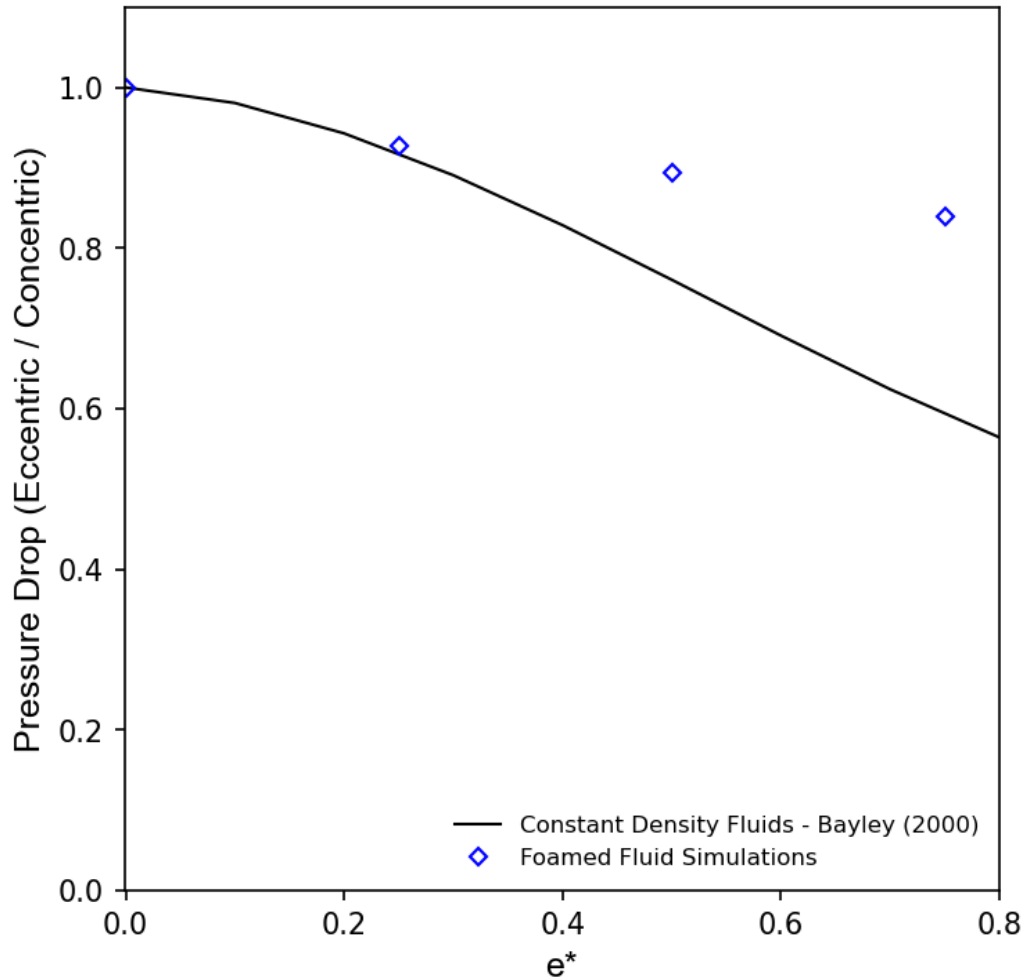


Figure 4-10. Pressure for eccentric annulus foamed fluid flow drop comparisons with Bailey correlation.

This result indicates the foamed fluid should perform better in the displacement simulations for highly eccentric casing in the wellbore, because of the ability to maintain a high viscosity in the narrow part of annulus. This indication will be executed in the next sections.

### 4.3.

#### Well cementing scenarios and test cases details

##### 4.3.1

##### Simple test case

At first, a simple test case will be considered for analysis. The simplistic aspect follows from a large density and viscosity contrast, and it is expected that the displacement of *Fluid 1* by *Fluid 2* occurs easily. The case is to be also relevant to check the velocity profile changes with pressure and to check the behavior of the interface shape in a large density contrast. Table 4-3 summarizes the data used for the test case simulation.

Table 4-3. Test case data

Property	Fluid 1 (displaced)	Fluid 2 (displacing)
<b>Fluid Type</b>	Constant density drilling fluid	Foamed cement
<b>Density (<math>\rho</math>)</b>	1000 kg/m <sup>3</sup>	$\rho_{liq} = 1900 \text{ kg/m}^3$ $RGL_{STD} = 4.5 \text{ m}^3/\text{m}^3$ Variable density
<b>Consistency Index (k)</b>	0.1 Pa.s <sup>n</sup>	$K_{base\_fluid} = 1.0 \text{ Pa.s}^n$
<b>Behavior Index (n)</b>	0,8	0,7
<b>Yield Stress (<math>\tau_y</math>)</b>	0.3 Pa	$\tau_{y\_base\_fluid} = 0.5 \text{ Pa}$
<b>Inlet Mass Flow Rate</b>	39,39 kg/s (total)	
<b>Outlet Pressure</b>	1,0 MPa	

Two cases were simulated:

- A 2-D case considering a fully centralized casing;
- A 3D case considering an eccentricity of 50%.

Figure 4-11 presents the velocity field and phase concentration for two different times at the flow. It is shown that, as long as the two fluids flow in the annulus, the interface distorts the velocity profile due to the expansion of the foamed fluid.

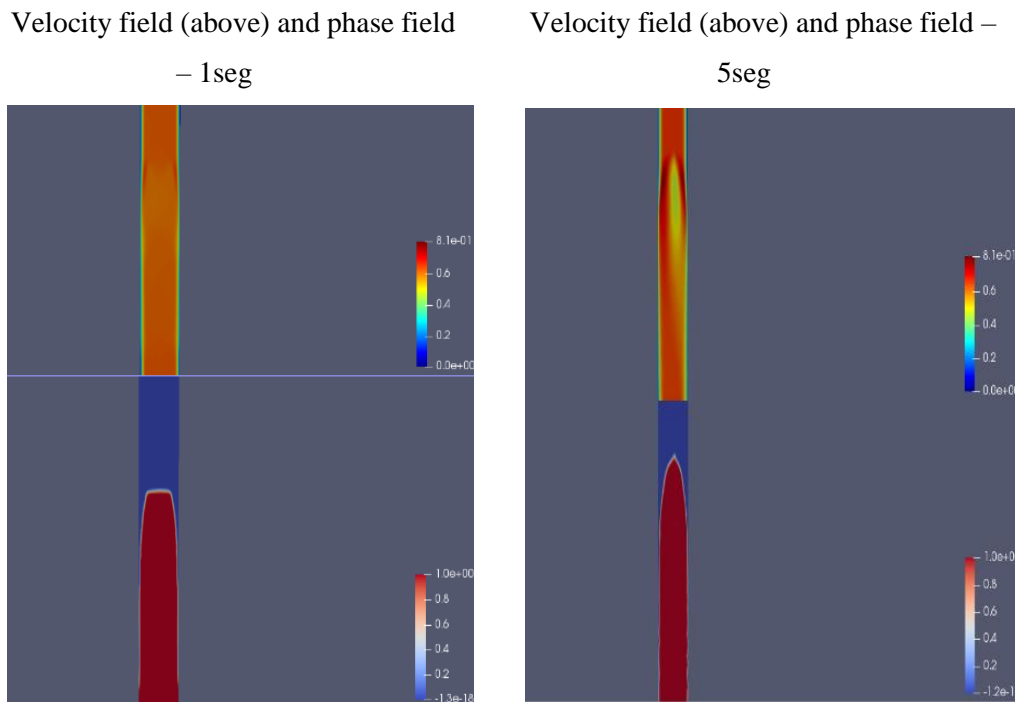


Figure 4-11. Velocity and phase concentration fields in 2D simulations showing interface evolution.

For the 3D case (eccentric), the results plotted are the density profile at the wide and narrow side of the eccentric annulus and the density profile in the case of fully concentric annulus; and the velocity contour in the sections filled with the foamed (displacing) fluid and in the sections filled with the displaced fluid. Both are presented in Figure 4-12 and Figure 4-13. As expected, the model correctly predicts the preferred flow in the wide side but still shows some displacement in the narrow side, due to the expanding effect that leads to an increase of the velocity as the fluids flow upwards.

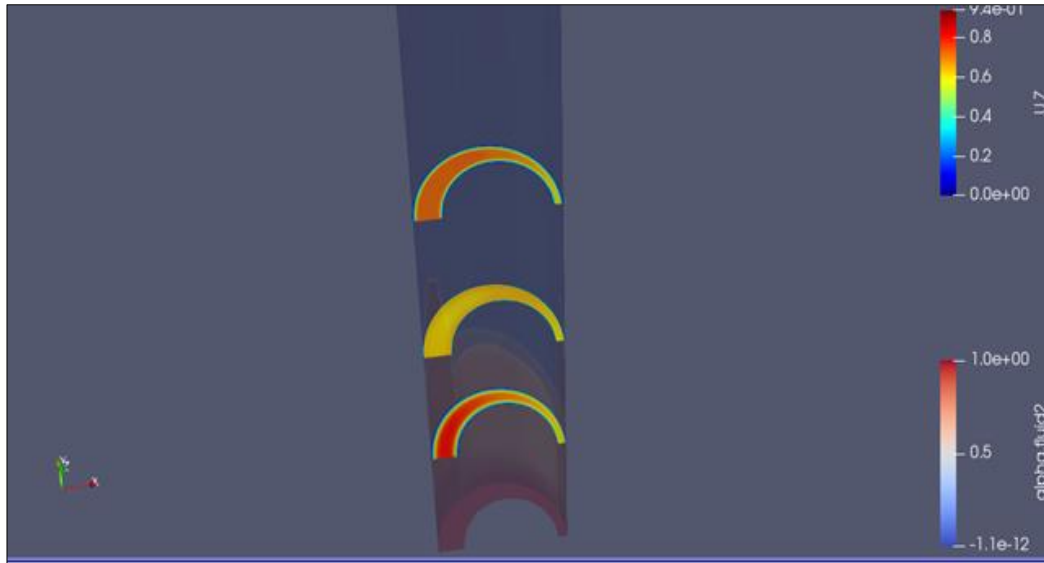


Figure 4-12. Velocity profile evolution with the density and rheology pressure dependence at  $t = 2,6s$  for sections at  $z = 0,5m$ ;  $z = 1,0m$  and  $z = 2,0m$ .

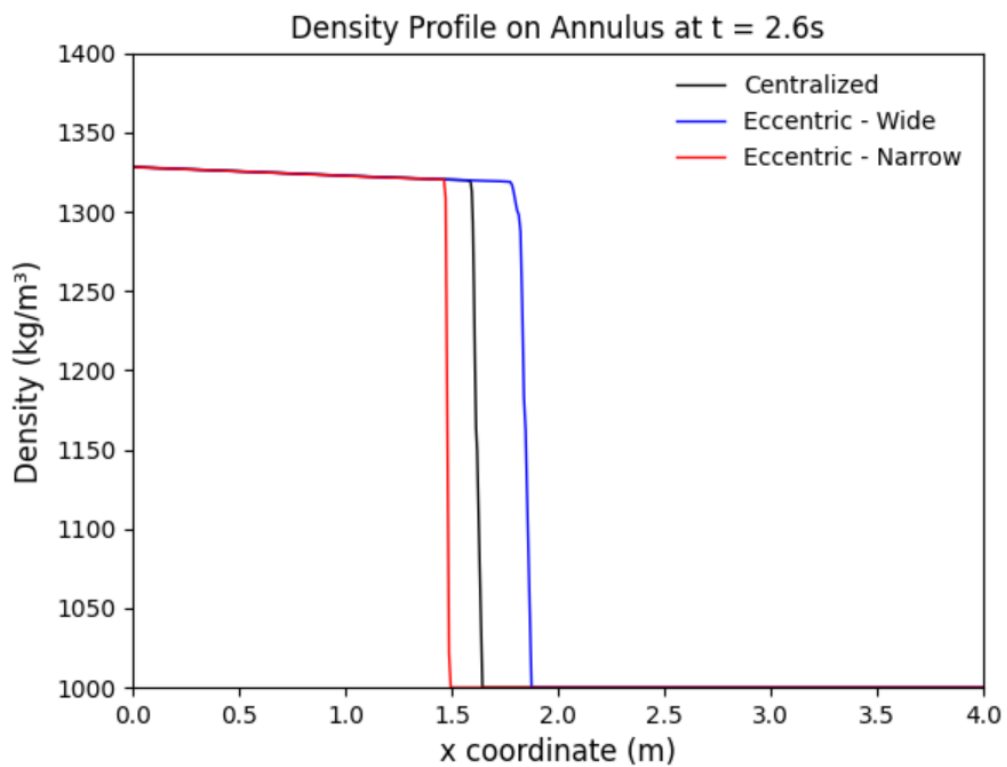


Figure 4-13. Average density profile at wide and narrow side of annular space

The evolution of the displacement efficiency is another result of interest to evaluate the proper substitution of the fluids. The Total Displacement Efficiency (TDE) is defined as Eq. 4-4.

$$TDE = \frac{V_{displacing\ fluid}}{V_{control}} = \frac{\left[ \int_0^t \left( \int_{V_{control}} \alpha_2 \cdot dV \right) dt \right]}{[V_{control}]} \quad (4-4)$$

Where  $V_{control}$  is the first half ( $0 \leq z \leq \frac{L}{2}$ ) of the annular space in the domain, called the control volume, as shown in Figure 4-14. The control volume represents, in this case, the section of the well where zonal isolation is required, even if more cement slurry volume is necessary.

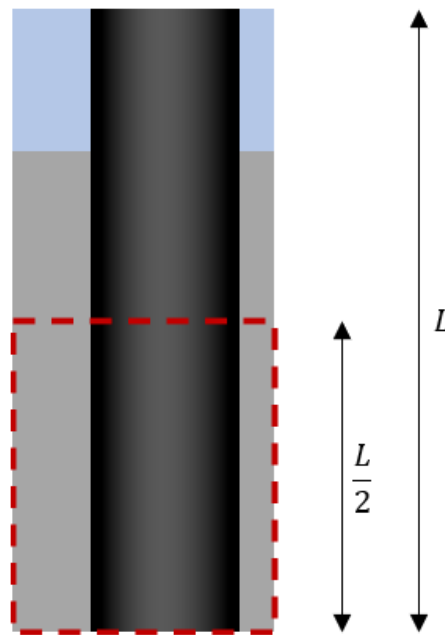


Figure 4-14. Control Volume definition for TED calculations

The displacement efficiency for a fully concentric annulus and a 50% eccentricity is plotted in Figure 4-15.

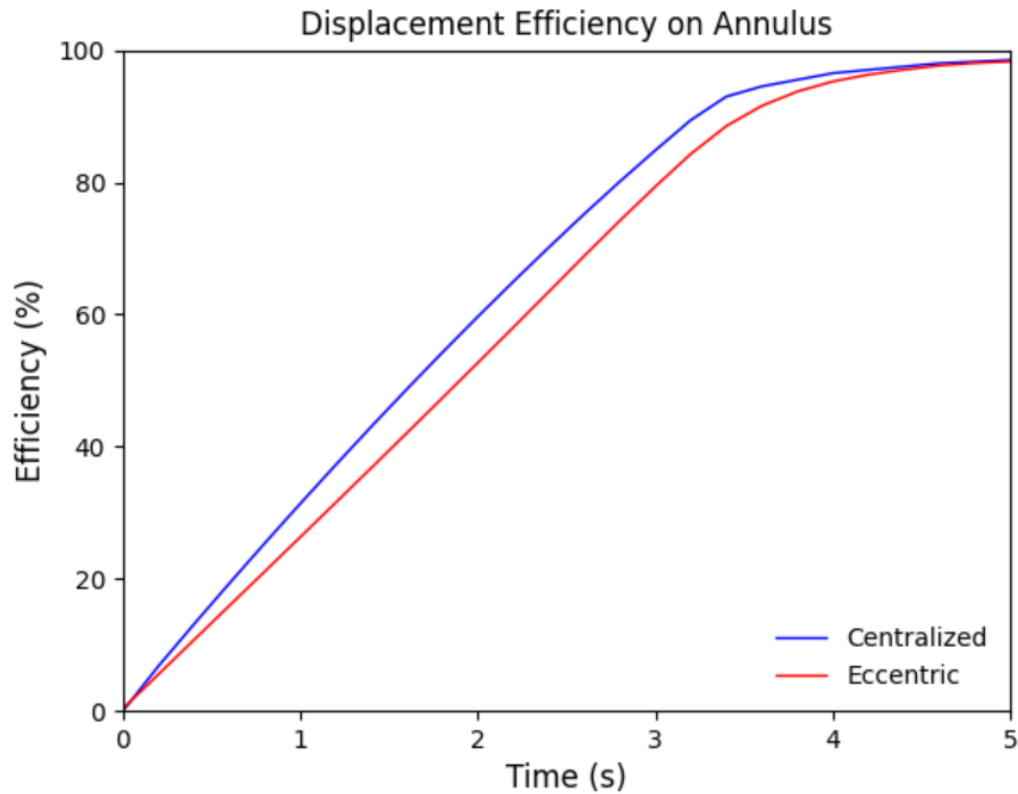


Figure 4-15. Displacement efficiency curves for the control volume in annular space

### 4.3.2

#### Realistic scenario case

The second analysis focused on evaluating a more realistic and challenging scenario for well cementing in deepwater wells, considering typical drilling fluid density and rheology. Typically, the density contrast for long cemented sections – which require lightweight cement slurries – should be lower than the previous case to ensure the annular pressure does not exceed the fracture gradient.

The parameters to be evaluated consider a common well configuration of a deepwater well 10 3/4" surface-production casing (Figure 4-16) in a well drilled with a 14 3/4" bit, as Table 4-4.

Table 4-4. Basic data for the deepwater well case study

Variable	Value
Total Depth of casing shoe	3110 m
Casing size OD	10 ¾" (0,27305 m)
Well diameter	14 ¾" (0,37465 m)
Fluid 1	Aqueous drilling fluid
Fluid 2	Cement slurry
Basic liquid pump rate	8 bpm ( $2.65 \times 10^{-3} \text{ m}^3/\text{s}$ )
Outlet Pressure	1450 psi (10 Mpa)

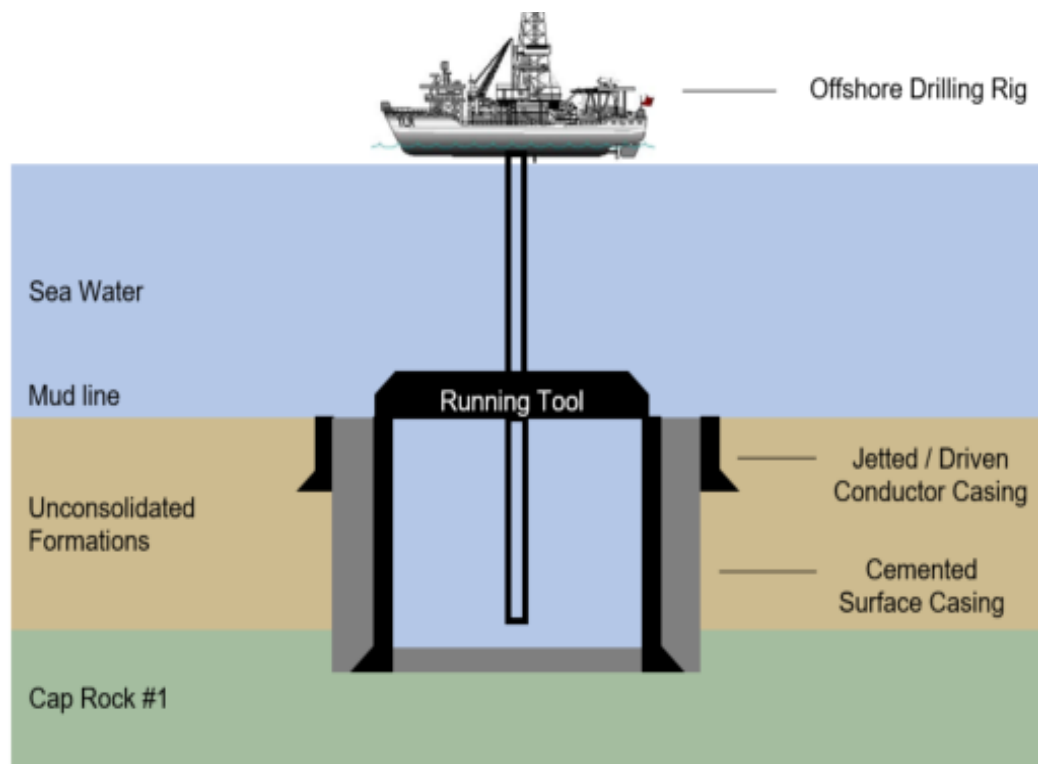


Figure 4-16. Well configuration for simulations.

The basic data for the fluid density and rheology are considered in Table 4-5 below, and the flow curves for the inlet conditions (initial pressure and velocity) are shown in Figure 4-17.

Table 4-5. Fluid data for deepwater well case study

Property	Fluid 1 (displaced)	Foamed Fluid 2 (displacing)	Constant Fluid 2 (displacing)
<b>Fluid Type</b>	Constant density drilling fluid	Foamed cement	Lightweight cement
<b>Density (<math>\rho</math>)</b>	1400 kg/m <sup>3</sup> (11.7 ppg)	$\rho_{liq} = 1900$ kg/m <sup>3</sup> (15.9 ppg) $RGL_{STD} = 28$ m <sup>3</sup> /m <sup>3</sup> Variable density	1500 kg/m <sup>3</sup> (12.5 ppg)
<b>Consistency Index (k)</b>	2.0 Pa.s <sup>n</sup>	$K_{base\_fluid} = 0.5$ Pa.s <sup>n</sup>	$K_{base\_fluid} = 0.5$ Pa.s <sup>n</sup>
<b>Behavior Index (n)</b>	0.4	0.85	0.85
<b>Yield Stress (<math>\tau_y</math>)</b>	0.4 Pa	$\tau_{y\_base\_fluid} = 4.0$ Pa	$\tau_{y\_base\_fluid} = 4.0$ Pa
<b>Surface tension</b>	0.07 Pa/m (all cases)		

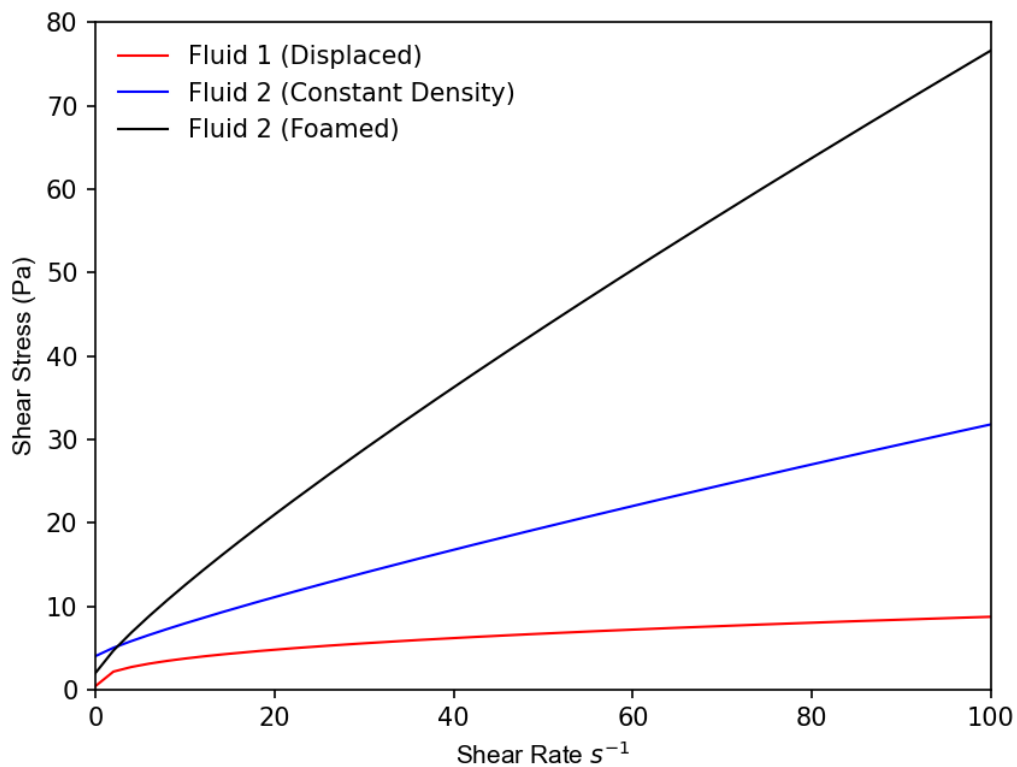


Figure 4-17. Flow curves for the fluids in the case study, considering the inlet conditions.

#### 4.4.

#### Parametric analysis of displacement flow, dimensional analysis

The flow under analysis is scaled based on the following dimensional and dimensionless variables.

The hydraulic diameter  $D_h$  is defined from external and internal radius in Eq. 4-5. Dimensional eccentricity  $e$  and dimensionless eccentricity  $e^*$  are defined in Eq. 4-6.

$$D_h = 2(R_o - R_i) \quad (4-5)$$

$$e^* = \frac{e}{(R_o - R_i)}, \text{ where } 0 \leq e \leq (R_o - R_i) \quad (4-6)$$

The characteristic shear rate  $\dot{\gamma}_c$  for a concentric annular flow from Eq. 4-7 is used to determine the Reynolds Number (Re) as per Eq. 4-8.

$$\dot{\gamma}_c = \left(\frac{4\bar{U}}{D_h}\right) \cdot \left(\frac{2n+1}{n}\right), \text{ where } \bar{U} = \frac{\dot{m}_{in}}{\rho_{in} \cdot Area} \quad (4-7)$$

$$Re = \frac{8 \cdot \rho \cdot \bar{U}^2}{\tau_w} \quad (4-8)$$

The Reynolds number represents the ratio of inertia forces and viscous forces. To evaluate the relation between the gravitational (buoyancy) forces and viscous forces, the Galilei Number (Ga) is considered as dimensionless parameter, described as Eq. 4-9. The buoyancy force considers the density of the displacing fluid at inlet ( $\rho_{2,inlet}$ ) and the density of the displaced fluid ( $\rho_1$ ).

$$Ga = \frac{(\rho_{2,inlet} - \rho_1)gD_h^2}{\eta_2\bar{U}} \quad (4-9)$$

The dimensionless density contrast is given by Atwood number ( $At$ ) as per Eq. 4-10, and an expansion ratio ER is used to consider density difference in inlet and outlet for the foamed fluids as per Eq. 4-11.

$$At = \frac{\rho_{2,inlet} - \rho_1}{\rho_{2,inlet} + \rho_1} \quad (4-10)$$

Where  $\rho_1$  and  $\rho_2$  are, respectively, the density of the displaced and displacing fluid. When the displacing fluid is compressible, the density at inlet ( $\rho_{2,inlet}$ ) in the beginning of the simulation is considered.

$$ER = \frac{\rho_{2,inlet}}{\rho_{2,outlet}} \quad (4-11)$$

A dimensionless viscosity ratio  $\eta^*$  and dimensionless shear stress  $HB_{N1}$  and  $HB_{N2}$  are defined as per Eq. 4-12, Eq. 4-13, and Eq. 4-14.

$$\eta^* = \frac{\tau_{w2}}{\tau_{w1}} \quad (4-12)$$

$$HB_{N1} = \frac{\tau_{01}}{\tau_{w1}} \quad (4-13)$$

$$HB_{N2} = \frac{\tau_{02}}{\tau_{w2}} \quad (4-14)$$

For the results presentation, parameters to be considered are:

- The dimensionless pumped volume  $V^*$  which is the relation between the pumped volume of the displacing fluid and the control volume, defined in Eq. 4-15;
- The total (volumetric) displacement efficiency TDE, defined in Eq. 4-16;
- And wall displacement efficiency (at wall surfaces) WDE are defined as Eq. 4-17.

$$V^* = \frac{V_{displacing\ fluid, pumped}}{V_{control}} = \frac{\left[ \int_0^t \left( \int_{Inlet} \vec{U} \cdot dA \right) dt \right]}{[V_{control}]} \quad (4-15)$$

$$TDE = \frac{V_{displacing\ fluid}}{V_{control}} = \frac{\left[ \int_{V_{control}} \alpha_2 \cdot dV \right]}{[V_{control}]} \quad (4-16)$$

$$WDE = \frac{A_{displacing\ fluid}}{A_{control}} = \left[ \int_{A_{control}} \alpha_2 \cdot dA \right] / [A_{control}] \quad (4-17)$$

Both results are of interest in this work regarding zonal isolation in cementing operations. TDE shows the total volumetric displacement in the annulus (overall concentration of cement slurry), where low values may indicate that severe channeling occurred or that the interface between the two fluids is too elongated. Thus, zonal isolation would be compromised in the short term (API, 2010).

WDE will relate to the effectiveness of the displacement to remove the film of the displaced fluid near casing or formation walls. When a small density contrast is present, that lead to low buoyancy effects (Nelson, 2006; Foroushan, 2021) filling the walls with the displacing fluid will be more challenging. Consequently, the micro annulus risk will be higher, and possible consequences are surface casing pressure and loss of zonal isolation in the long term (Ahmady, 2020). A micro annulus may also impact the interpretation of cement bond logs due to the lower attenuation provided (Kalyanraman, 2021).

For this work 28 simulation cases were defined, considering changes in the fluid properties and boundary conditions. Table 4-6, Table 4-7 and Table 4-8 summarize the cases which considers the base cases “Foam#1” and “Constant#2” which takes the data from Table 4-4 and Table 4-5. The detailed data for the other simulation cases are described in Appendix C.

Table 4-6. Cases with Ducloué Correlation – Reference Flow parameters, changing geometry.

Case	$\eta^*$	At	Re	Ga	$e^*$	$\beta$
Foam #1	2.1	0.038	118	65.9	0	0°
Constant #2	1.57	0.038	118	77.8	0	0°
Foam #3	2.1	0.038	118	65.9	0.50	0°
Constant #4	1.57	0.038	118	77.8	0.50	0°
Foam #5	2.1	0.038	118	65.9	0.75	0°
Constant #6	1.57	0.038	118	77.8	0.75	0°
Foam #7	2.1	0.038	118	46.6	0.50	45°
Foam #8	1.57	0.038	118	0.0	0.50	90°

Table 4-7. Cases with Ducloué Correlation, changing flow parameters.

Case	$\eta^*$	At	Re	Ga	$e^*$	$\beta$
Foam #9	1.07	0.038	118	65.9	0.0	0°
Constant #10	0.78	0.038	118	77.8	0.0	0°
Foam #11	1.77	0.038	118	65.9	0.0	0°
Constant #12	1.30	0.038	118	77.8	0.0	0°
Foam #13	2.1	0.0	118	0.0	0.0	0°
Constant #14	1.57	0.0	118	0.0	0.0	0°
Foam #15	2.1	0.076	118	127.4	0.0	0°
Constant #16	1.57	0.076	118	150.7	0.0	0°
Foam #17	2.1	0.163	118	257.1	0.0	0°
Constant #18	1.57	0.163	118	304.2	0.0	0°
Foam #19	2.1	0.038	59	93.7	0.0	0°
Constant #20	1.57	0.038	59	108.7	0.0	0°
Foam #21	2.1	0.038	236	44.3	0.0	0°
Constant #22	1.57	0.038	236	53.1	0.0	0°

Table 4-8. Simulation of eccentric cases from the worst cases in the concentric simulations

<b>Case</b>	$\eta^*$	<b>At</b>	<b>Re</b>	<b>Ga</b>	$e^*$	$\beta$
Foam #23	1.07	0.038	118	65.9	0.50	45 °
Constant #24	0.78	0.038	118	77.8	0.50	45 °

Table 4-9. Cases considered to evaluate the correlation effect from Eq. 3-22

<b>Case</b>	$\eta^*$	<b>At</b>	<b>Re</b>	<b>Ga</b>	$e^*$	$\beta$
Foam #25	3.7	0.038	118	44.3	0.0	0°
Foam #26	1.8	0.038	118	44.3	0.0	0°
Foam #27	3.7	0.0	118	0.0	0.0	0°
Foam #28	3.7	0.038	118	44.3	0.50	0°

The Capillary Number ( $Ca = \eta_2 \bar{U} / \sigma$ ) represent the ratio of viscous forces and surface tension. It ranges from 1.85 and 5.01 in the cases, above the range where capillary forces are dominant (<0.1). The dimensionless expansion rate ER was lower than 1.01 in all cases due to the length of the annulus.

## 5

### **Results and discussions**

#### 5.1.

##### **Results from the foamed cement displacement simulations**

This section presents the results obtained from the displacement simulations. The displaced fluid (Fluid 1) has constant density, and the displacing fluid (Fluid 2) is a foamed fluid (representing a foamed spacer or foamed cement). The changes in geometry, fluid properties and flow parameters are considered and presented separately or combined.

##### 5.1.1.

###### **Eccentricity effect in the displacement efficiency**

The first analysis considers the base case (Foam #1) and different eccentricities. The impact on the eccentricity on the interface evolution are shown in Figure 5-1 and Figure 5-2 for different pumped volumes . The impact on the TDE (Total Displacement Efficiency) is shown in Figure 5-3 where the evolution is compared to each other and a “perfect plug” flow (where the displacement front is a linear flat surface without any mixing).

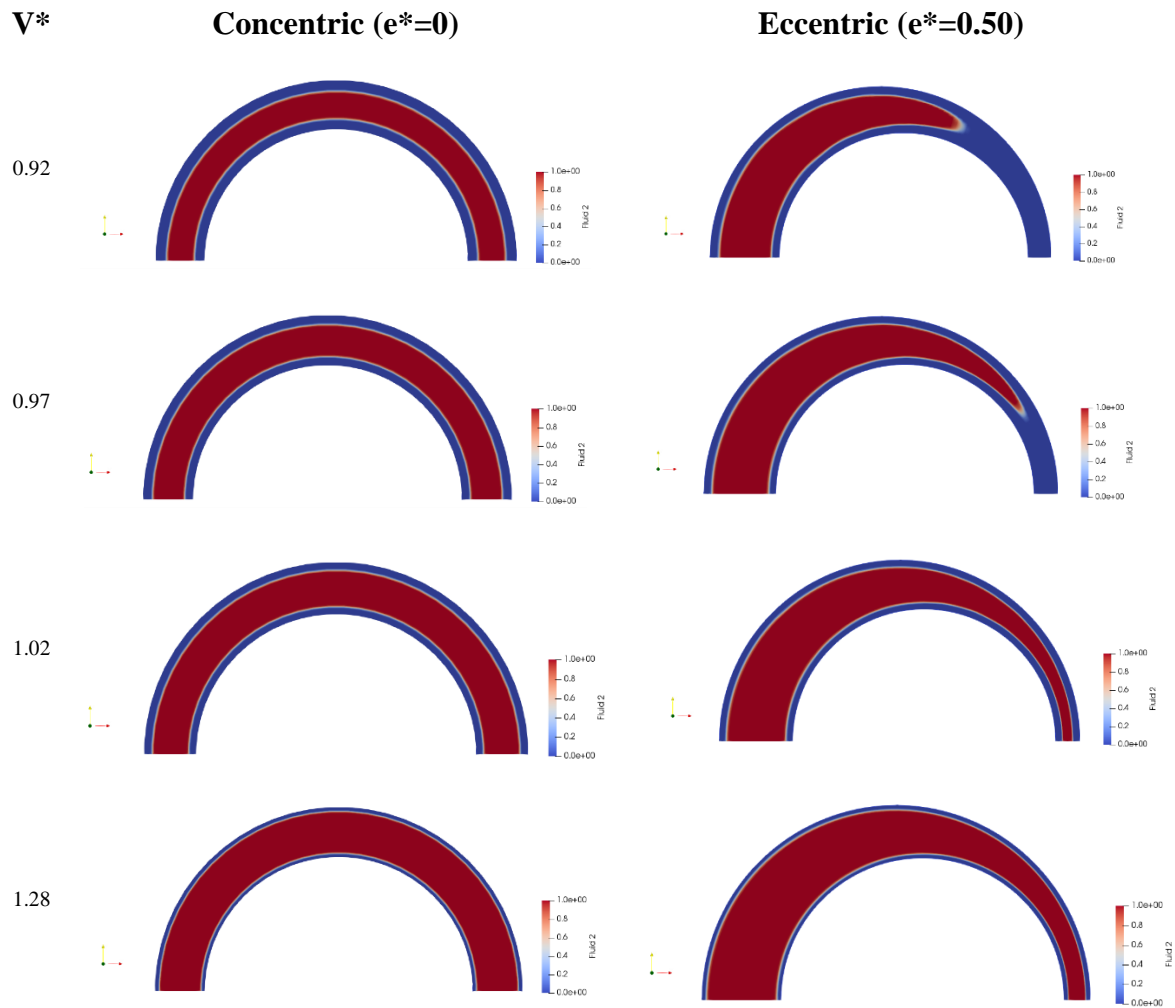


Figure 5-1. Foamed fluid Fluid 2 concentration (Reference Case) for concentric (Foam #1) and eccentric (Foam #3) annulus at  $z = 2.0\text{m}$  for different pumped volumes

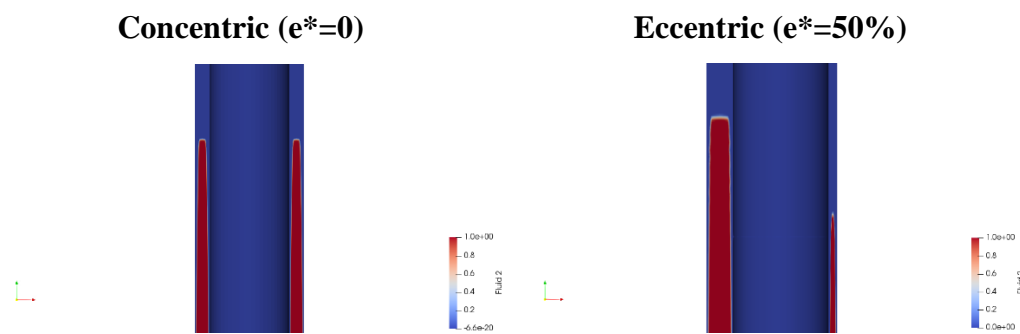


Figure 5-2. Interface shape at  $V^*=1.02$  around  $z=2.0\text{m}$  (Reference Case) for concentric (Foam #1) and eccentric (Foam #3) annulus

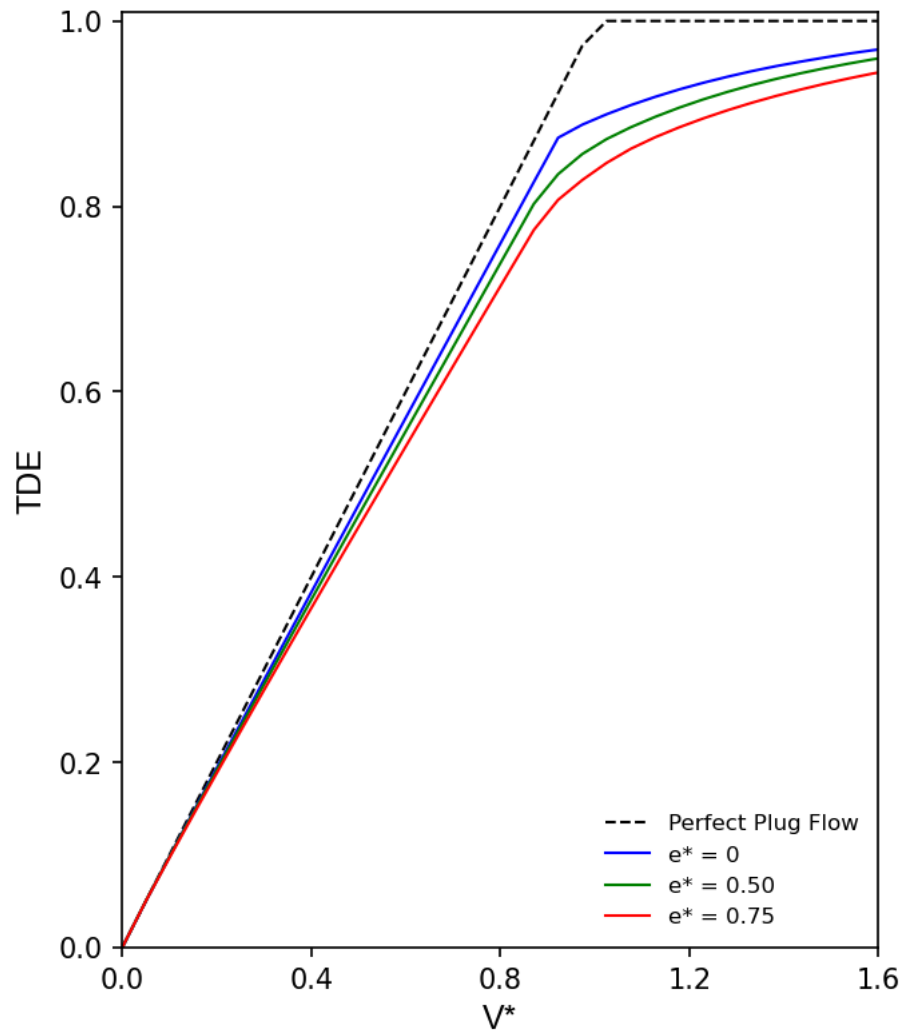


Figure 5-3. Eccentricity effect for basic case simulations on TDE (cases Foam #1, Foam #3, and Foam #5)

The displacement front remains stable in all the three conditions, with an almost flat interface. However, the difference appears in the displacement at the wall where the removal of the displaced fluid (Fluid 1) occurs slowly. Figure 5-4 shows the phase fraction near the wall for the three considered eccentricities. As expected, the higher eccentricities lead to forming a channel near the narrow side of the wellbore due to the preferred flow in the wide side.

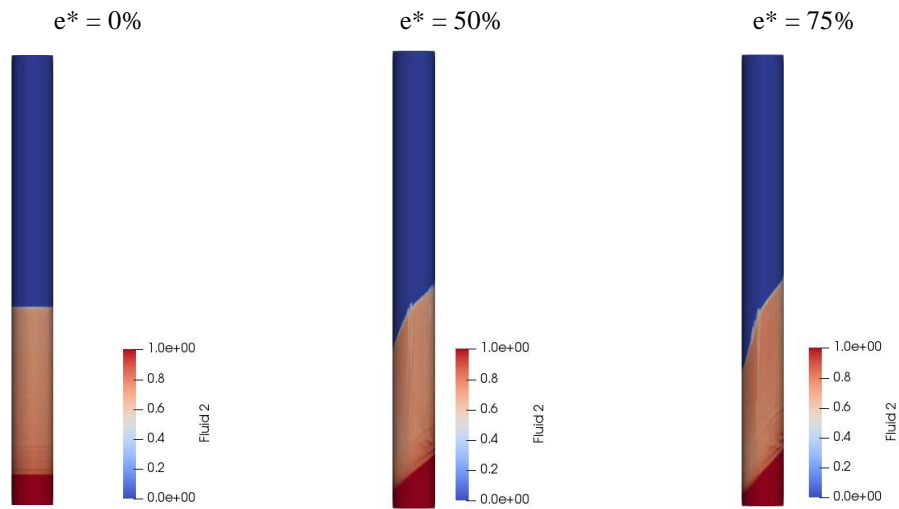


Figure 5-4. External wall fluid concentration for base case at  $V^*=1.64$  (cases Foam #1, Foam #3, and Foam #5)

The evolution of the displacing front in the external wall may be visualized in Figure 5-5 for the 75% eccentricity case, where the channeling in the narrow side of the well may be visualized.

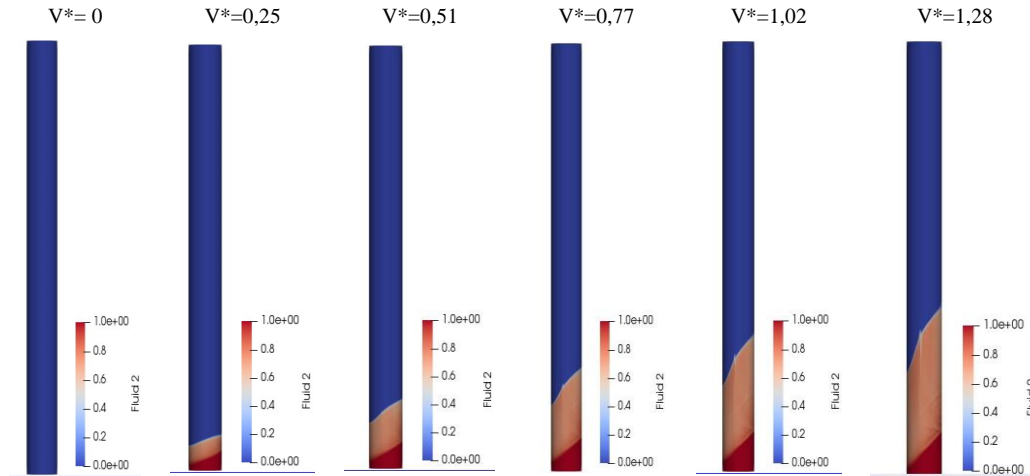


Figure 5-5. Fluid Concentration evolution in the external wall for base case at  $e^* = 0.75$  (Foam #5)

Quantitatively, the evolution of the Wall Displacement Efficiency (WDE) in the control volume is shown in Figure 5-6 and the final ( $V^* = 1.64$ ) efficiency summary is shown in Table 5-1.

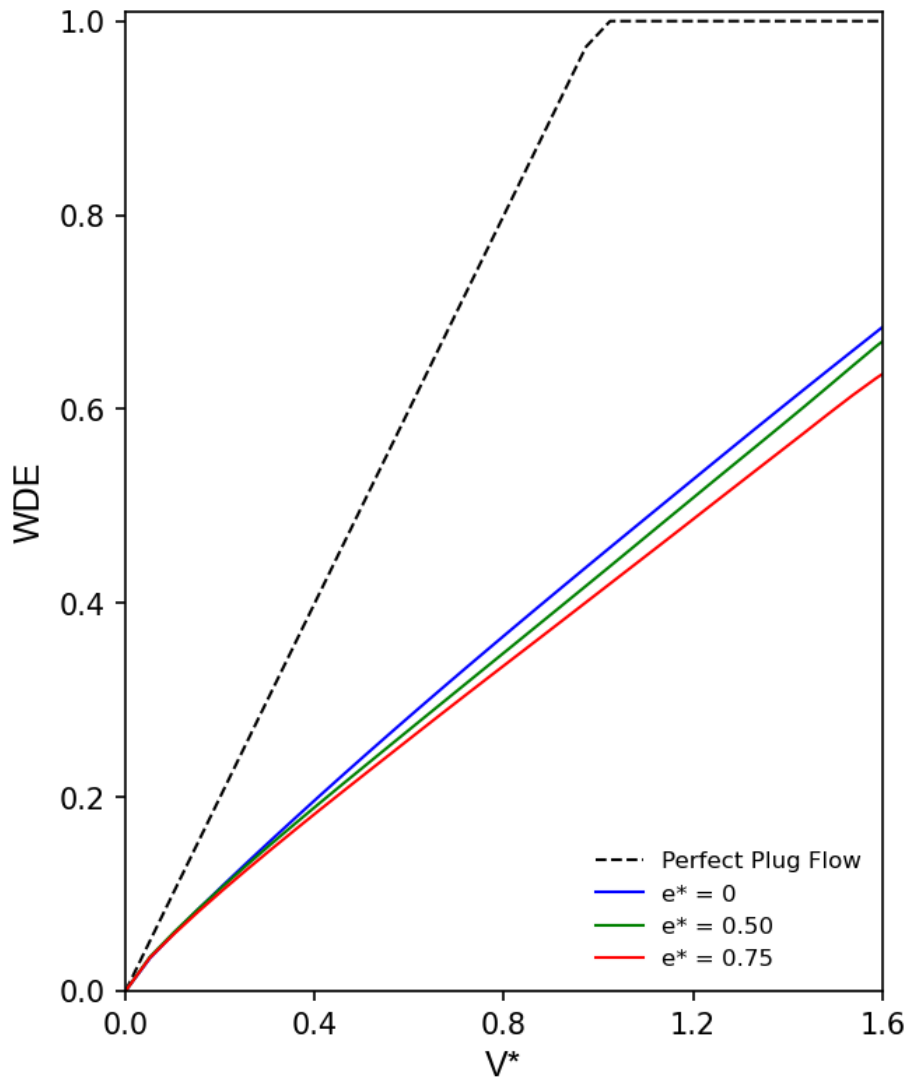


Figure 5-6. Wall displacement efficiency (WDE) for the base case and different eccentricities

Table 5-1. Summary results for base case at different eccentricities

Eccentricity	TDE ( $V^* = 1.64$ )	WDE ( $V^* = 1.64$ )
$e^* = 0.0$ (Foam #1)	0.9717	0.6995
$e^* = 0.50$ (Foam #3)	0.9628	0.6839
$e^* = 0.75$ (Foam #5)	0.9480	0.6483

### 5.1.2.

#### Deviation angle effect in the displacement efficiency

In this section the influence of the deviation angle of the well on the

displacement efficiency (total and in the wall) is evaluated for the base case with no eccentricity and with eccentricity of 50% ( $e^* = 0.50$ ). Although the deviation itself influences the eccentricity due to force balance of the casing weight and buoyancy forces, this coupled effect is not considered, i.e., the eccentricity is kept fixed for all the simulations.

With well deviation the gravitational component in the direction of flow will be lower and the effectivity of the density contrast is expected to be reduced. However, the velocity component in the direction of the narrower gap will induce a new effect. The importance of each will follow from the displacement results. Figure 5-7 shows the difference in the X-component in the velocity for a vertical and horizontal well, where it can be identified that in the horizontal (right) case more fluid is directed to the narrow side compared to the vertical case (left).

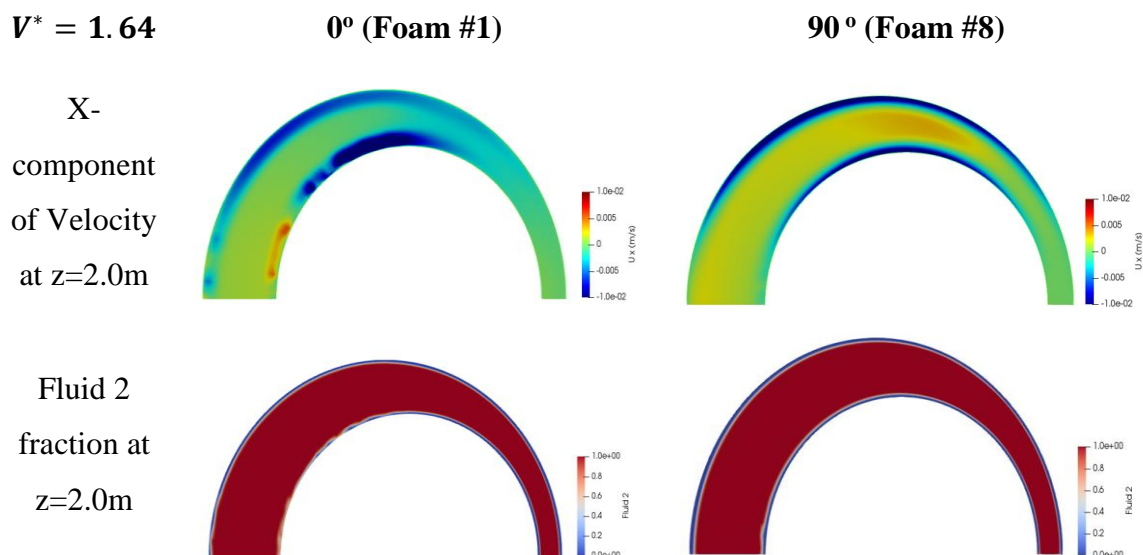


Figure 5-7. Velocity and volume fraction for 0° and 90° with  $e^*=0.50$

Figure 5-8 and Figure 5-9 show the Total Displacement Efficiency (TDE) and the Wall Displacement Efficiency (WDE), respectively.

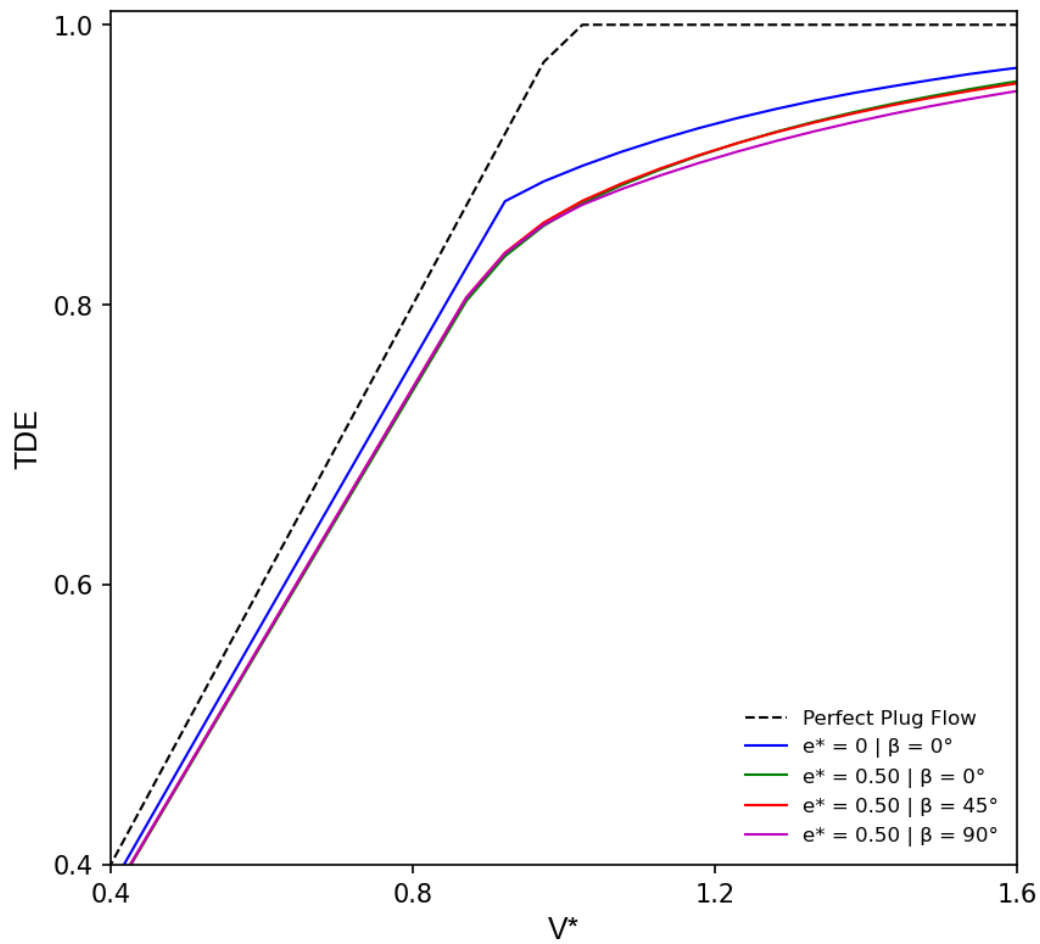


Figure 5-8. Total displacement efficiency (TDE) for basic case simulations considering well deviation effect (cases Foam #1, Foam #3, Foam #7 and Foam #8)

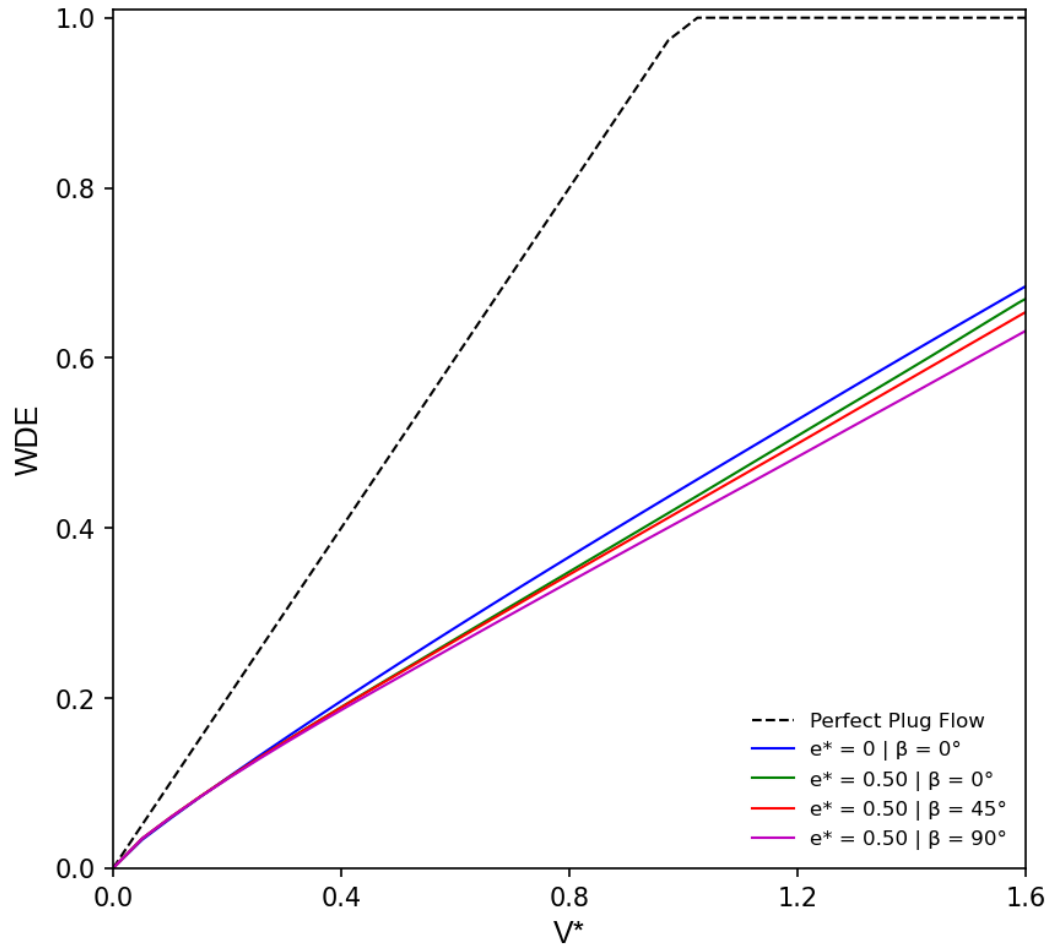


Figure 5-9. Wall displacement efficiency (WDE) for the base case and different well deviations (cases Foam #1, Foam #3, Foam #7, and Foam #8)

In conclusion, it was described the influence of the isolated effect of well deviation on the displacement efficiencies, which show a small difference on the final values as summarized in Table 5-2. Still, the displacement process is more efficient in low deviations because of the increase of buoyancy forces due to density contrast.

Table 5-2. Results for the simulations at  $V^* = 1.64$  with variable deviation angles  
(cases Foam #1, Foam #3, Foam #7, and Foam #8)

	$e^* = 0.0$	$e^* = 0.50$		
	$0^\circ$	$0^\circ$	$45^\circ$	$90^\circ$
<b>TDE</b>	0.9717	0.9628	0.9613	0.9560
<b>WDE</b>	0.6994	0.6839	0.6689	0.6463

### 5.1.3.

#### Effects from density and viscosity contrast in the displacement efficiency

This section considers the effect of density and viscosity contrast value between the fluids for a fully centralized geometry ( $e^* = 0.0$ ) and, for the worst case identified, considering an eccentricity of 50% ( $e^* = 0.50$ ). All cases are compared to the base case and between each other regarding the Total Displacement Efficiency (TDE) and Wall Displacement Efficiency (WDE). The results may be found in:

- Figure 5-10 for the effect of the viscosity contrast;
- Figure 5-11 for the effect of the density contrast.

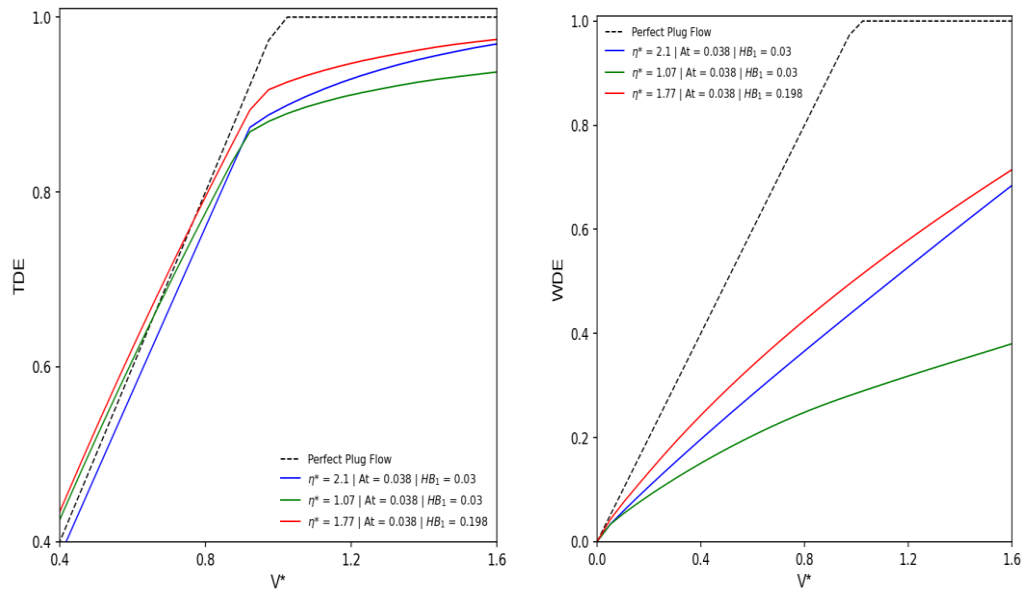


Figure 5-10. Results from centralized ( $e^*=0$ ) and variations in the Fluid 1 Rheology (cases Foam #1, Foam #9 and Foam #11)

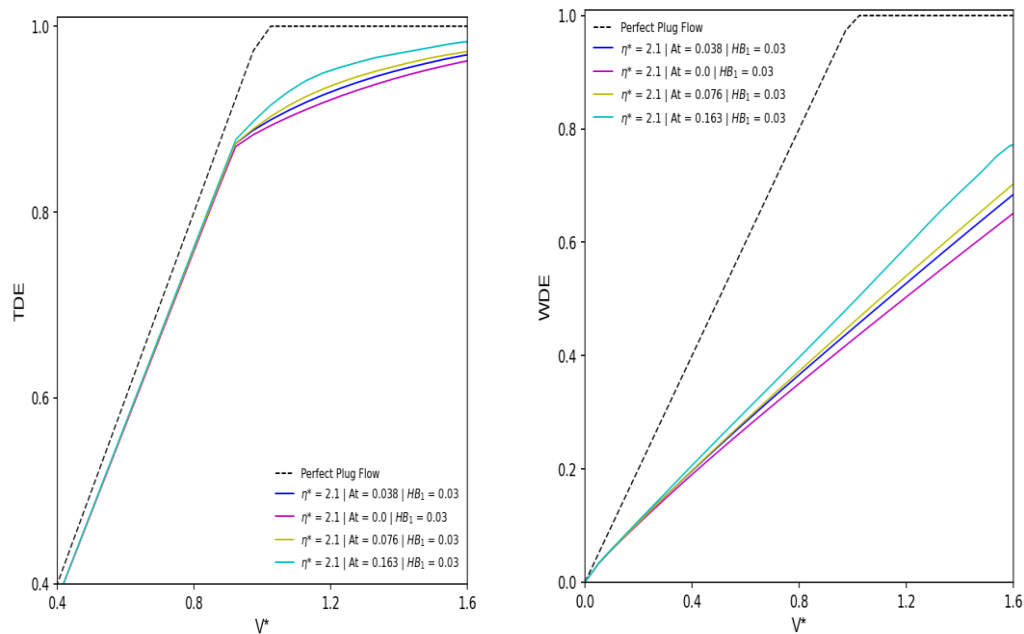


Figure 5-11. Results from centralized ( $e^*=0$ ) and variations in the Fluid 1 Density (cases Foam #1, Foam #13, Foam #15, and Foam #17)

The displacement efficiencies suffer from lower viscosity ratio but also are susceptible to the flow behavior of the displaced fluid, which interferes with the interface shape. This effect is also discussed in Foroushan et al (2021) and illustrates how non-Newtonian behavior influences efficiency.

The results suggest that increasing the viscosity contrast and optimizing the displaced fluid rheology is as impactful and effective as increasing the density contrast. However, at very low Atwood number conditions, the displacement efficiency exhibits high sensitivity to the decrease in viscosity contrast.

The final case simulated couples the eccentricity at  $e^* = 0.50$ ,  $45^\circ$  deviation angle and a lower viscosity ratio. The results are shown in Figure 5-12 below.

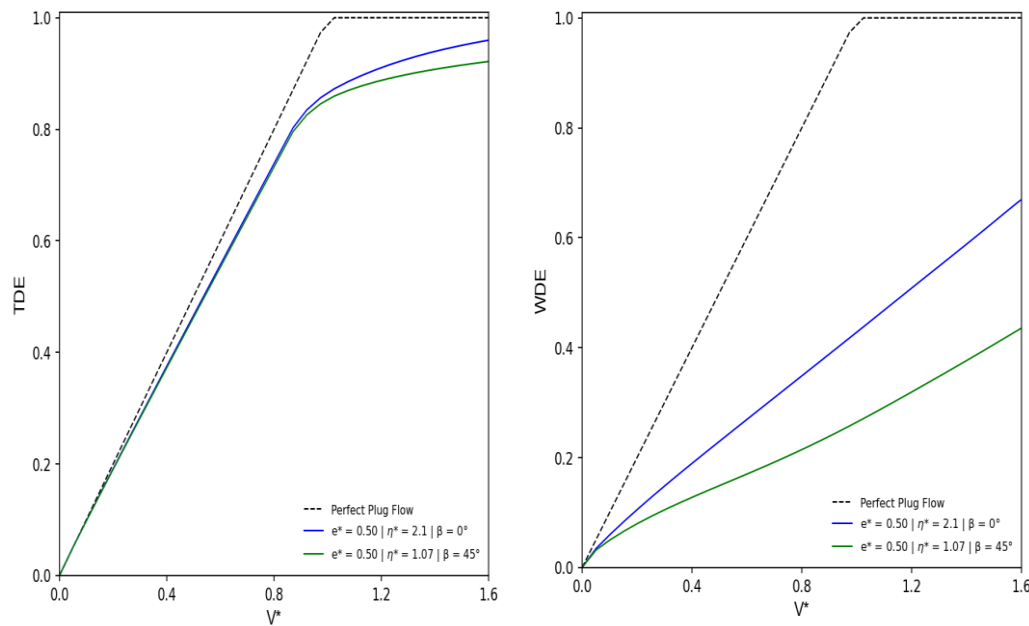


Figure 5-12. Results from eccentric base case ( $e^*=0.50$ ) and combined eccentric, inclined and with lower viscosity ratio (cases Foam #3 and Foam #23)

The combined effect of eccentricity and viscosity ratio also shows a decay in the displacement efficiency, dropping from 0.963 to 0.923, a 4% difference in the total volumetric displacement. However, in the wall the displacement is drastically reduced from 0.684 to 0.447, a 23,7% difference.

Both parameters – viscosity contrast and density contrast – are key to the success of the cementing job and shall be engineered to achieve adequate displacement efficiency. Thus, controlling and selecting properly the rheology and density of the drilling fluid, spacers, and cement slurries according to the simulation results will benefit the process.

#### 5.1.4.

## Effect of Reynolds Number in the displacement efficiency

In this section the effect on the liquid pumping flow rate changes will be evaluated, which affects the Reynolds number of the flow. The base case ( $Re = 118$ ) is compared to increased and decreased liquid pump rates cases with no eccentricity ( $e^* = 0.0$ ) regarding the Total and Wall Displacement Efficiencies (TDE and WDE), and the results are shown in Figure 5-13.

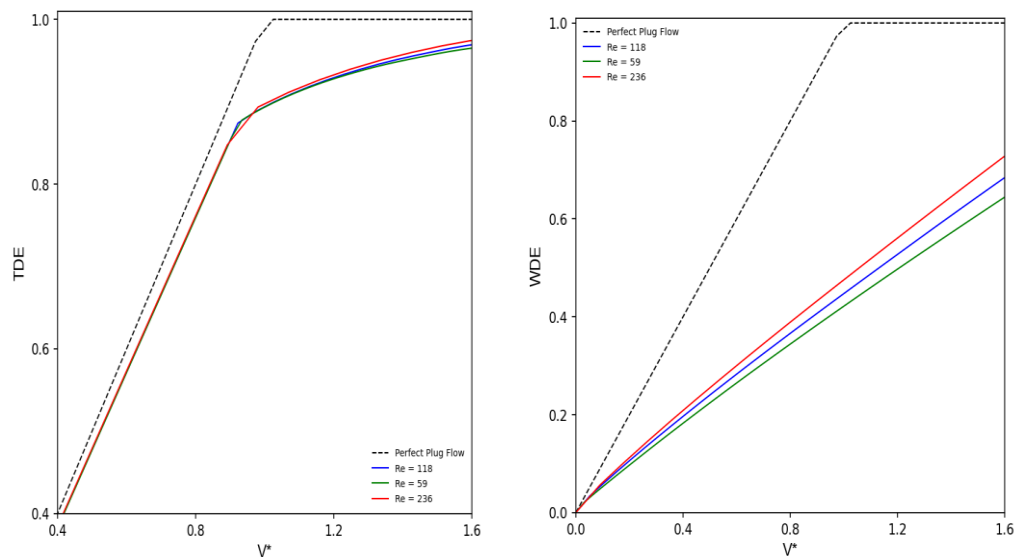


Figure 5-13. Results from centralized ( $e^* = 0$ ) and variations in the Reynolds Number (cases Foam #1, Foam #19, and Foam #21)

The change in the Reynolds number slightly impacted the TDE (less than 1%) and affected a little more the WDE output. The result is consistent with the faster movement of the interface and increase in the rate that the foamed fluid expands in the annulus. The difference observed in the results are:

- $Re = 236 \rightarrow$  WDE increased by 7,17% compared to  $Re = 118$ ;
- $Re = 59 \rightarrow$  WDE decreased by 5,81% compared to  $Re = 118$ .

### 5.1.5.

## Effect of foam constitutive model in the displacement efficiency

In this section the effect of a different correlation for the foamed fluid rheology will be evaluated. The correlation considered in Rosenbaum study (2019)

– presented in Eq. 3-31 and Eq. 3-22 estimates the foamed viscosity from the viscosity of the base fluid from a quadratic fit with experimental data and numerical modeling.

Figure 5-14 and Figure 5-15 show the TDE and WDE for selected cases including the base case and variations in the displaced fluid rheology and density and variation in casing eccentricity.

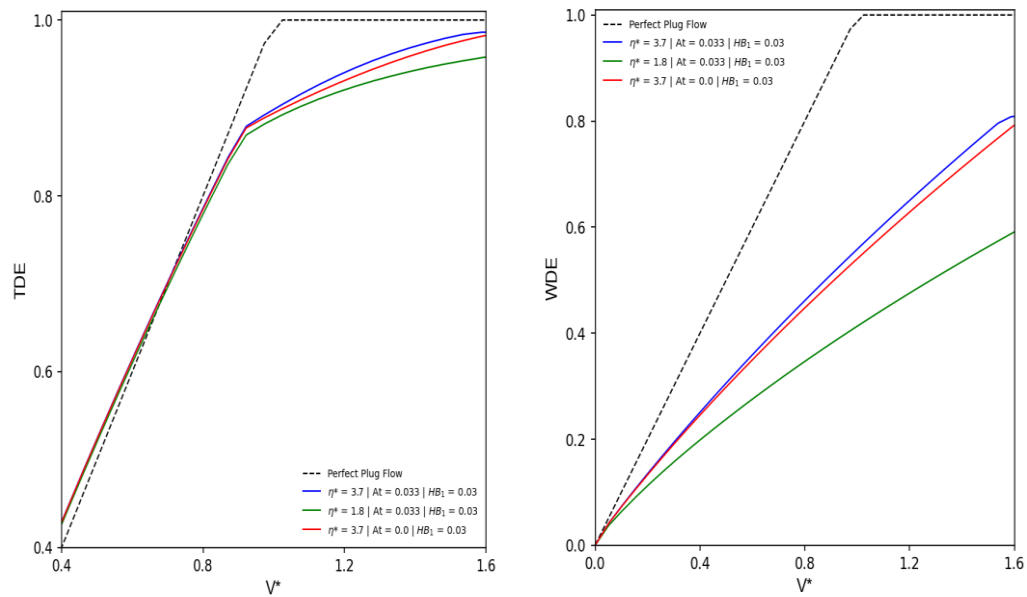


Figure 5-14. Effect from foam rheological correlation for concentric ( $e^*=0$ ) cases (Foam #25, Foam #26, and Foam #27)

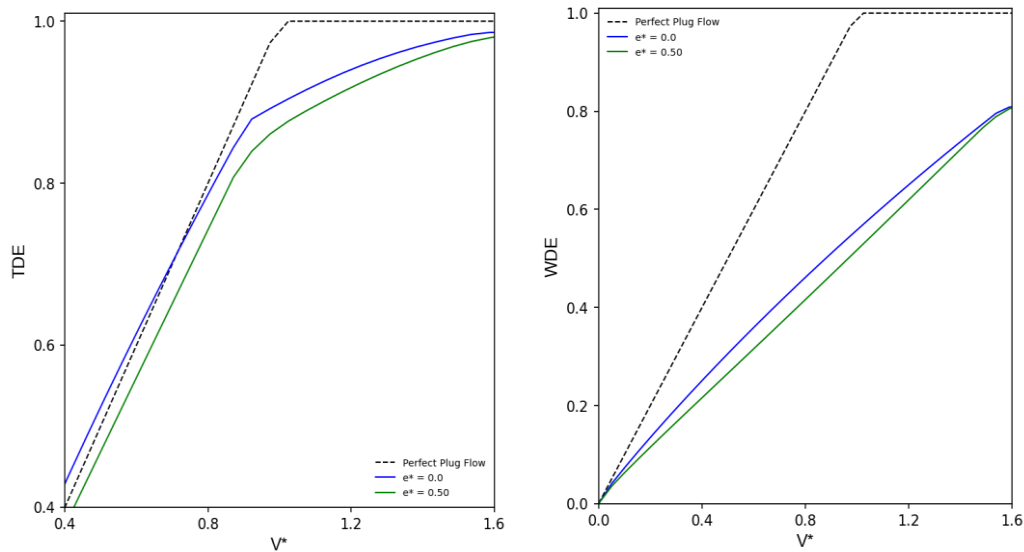


Figure 5-15. Effect from eccentricity for the simulations with the base case fluids and correlation from Rosenbaum et al. (cases Foam #3 and Foam #28)

The cases with the correlation from Eq. 3-21 and Eq. 3-22 showed the minimum difference between the variations in the fluid density, rheology, and casing eccentricity. It can be explained that because the increase in the foam viscosity highly exceeds the one of the displaced fluids, which leads to an intrinsically good displacing process.

The improvement in the displacement efficiency occurred in the TED, but the increase was particularly relevant for the WDE output, where the displacement in the walls were evaluated.

By considering the Eq. 3-21 and Eq. 3-22 correlation, improvements from 15,8% up to 55,7% were observed compared to the previous correlation used (from Eq. 3-20), as shown in Figure 5-16 and Table 5-3.

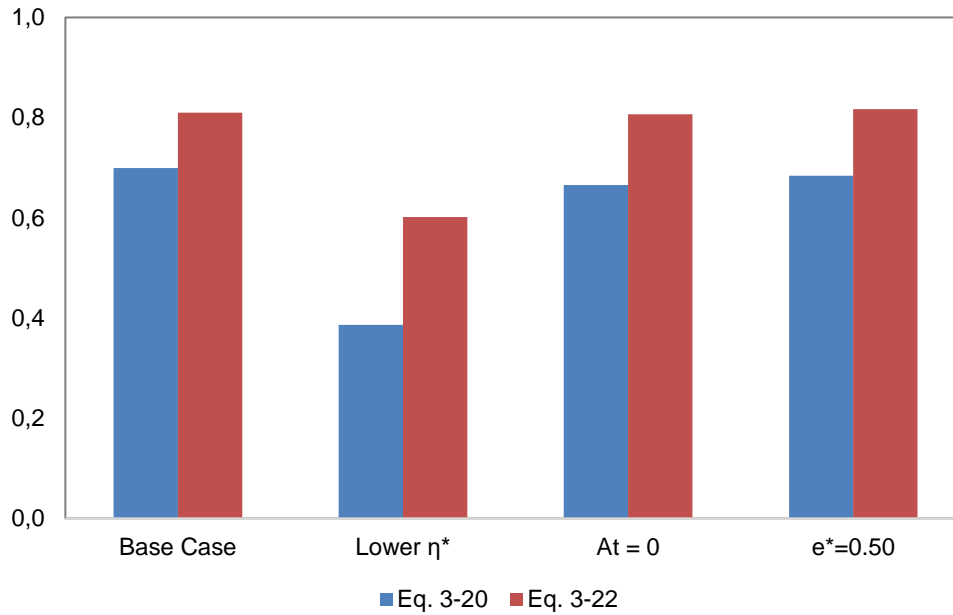


Figure 5-16. Difference in Wall Displacement Efficiency (WDE) for the two constitutional models considered in the simulations (at  $V^* = 1.6$ ).

Table 5-3. Difference in displacement efficiency results with correlation from Eq. 3-22 in relation to the correlation from Eq. 3-20

Simulation Case	Difference in TDE	Difference in WDE
<b>Base case</b>	+1,5%	+15,8%
<b>Lower <math>\eta^*</math></b>	+2,3%	+55,7%
<b><math>At = 0</math></b>	+2,0%	+21,3%
<b><math>e^* = 0.50</math></b>	+2,1%	+19,5%

Also, a qualitative view of this improvement can be observed in Figure 5-17 that shows the fluid concentration at the external wall, at instant  $V^* = 1.6$ . As the same color scale is used, the change in the constitutive modeling also shows a lower tendency of channeling in the annulus and lower contamination levels of the fluids.

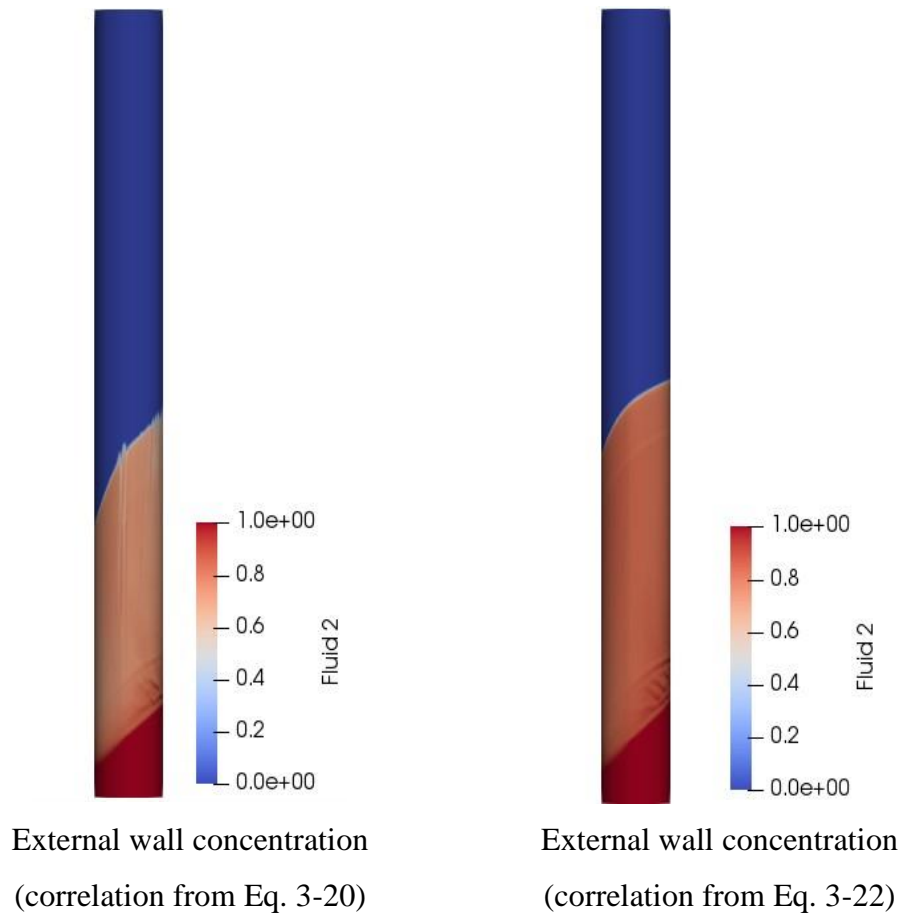


Figure 5-17. Comparison of the displacement at the external wall (Cases Foam #3 and Foam #28)

The results indicate that the proper estimation and selection of rheological models for the foamed fluids has major impact in the results of the displacement process. However, the results were qualitatively consistent in both simulations.

## 5.2.

### Results from the constant density and rheology cement displacement simulations

The following results relate to the eccentricity effect on TDE and WDE for the constant density simulations. The simulations consider identical boundary conditions, except for the fact that the displacing fluid (*Fluid 2*) has constant density equal to the one at the inlet of the foamed fluid simulation and that the liquid flow rates are equal. These considerations intend to closely align the foamed

and unfoamed simulation cases minimizing the variable change (*Ceteris paribus*).

The post-processing for Displacement Efficiency data and plots are the same as section 5.1. and considers the effects of eccentricity, density and viscosity contrast and Reynolds number. Table 5-4 indicates the source that directs to the results of each effect considered in the displacement efficiency simulations.

Table 5-4. Source for TDE and WDE for the constant density displacing fluid simulations

<b>Effect considered in the simulations</b>	<b>Source for TDE and WDE</b>
Eccentricity effect	Figure 5-18
Density contrast effect	Figure 5-19
Rheology and viscosity contrast effect	Figure 5-20
Flow rate effect	Figure 5-21
Combined effect of eccentricity and viscosity contrast	Figure 5-22

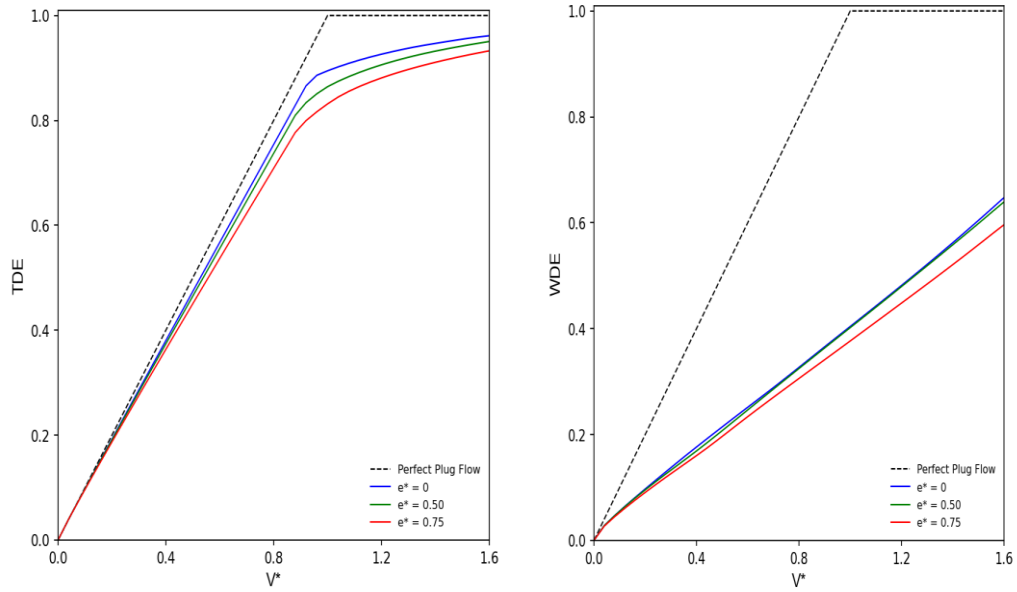


Figure 5-18. Effect from eccentricity for the simulations with the base case with constant density displacing fluid (cases Constant #2, Constant #4 and Constant #6)

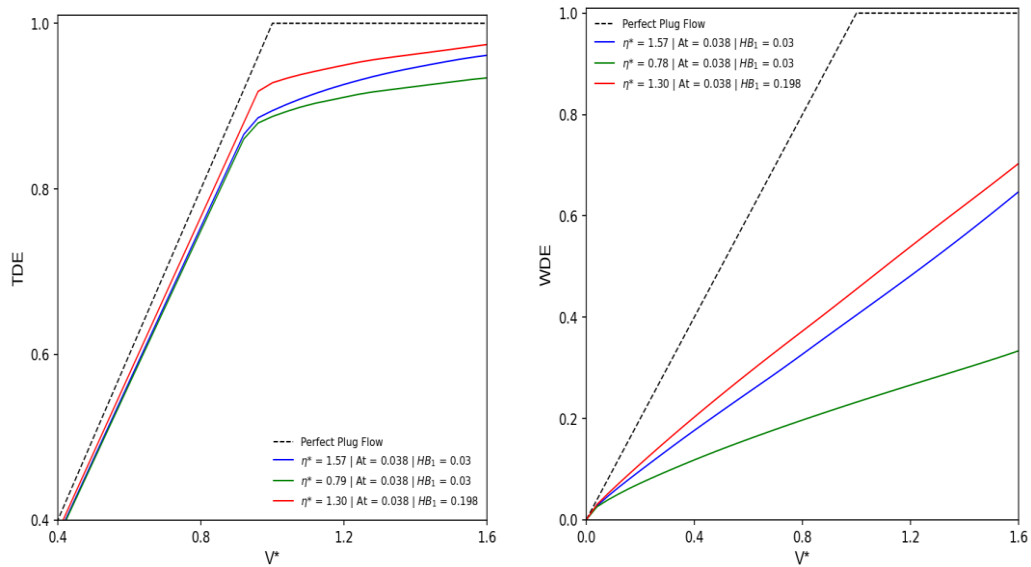


Figure 5-19. Effect from viscosity contrast for the simulations with constant density displacing fluid (cases Constant #2, Constant #10, and Constant #12)

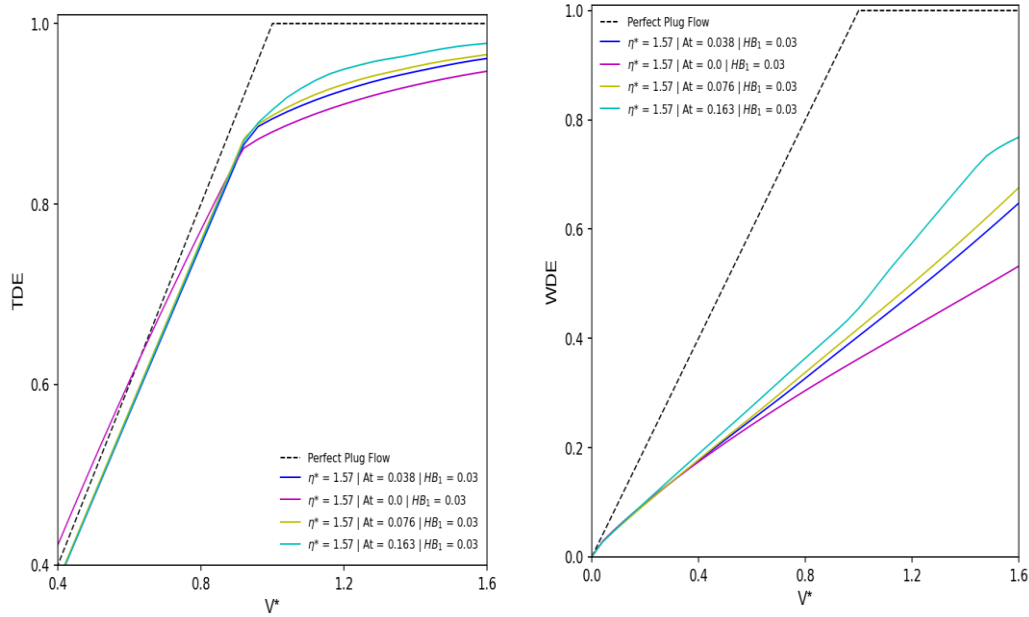


Figure 5-20. Effect from density contrast for the simulations with constant density displacing fluid (cases Constant #2, Constant #14, Constant #16, and Constant #18)

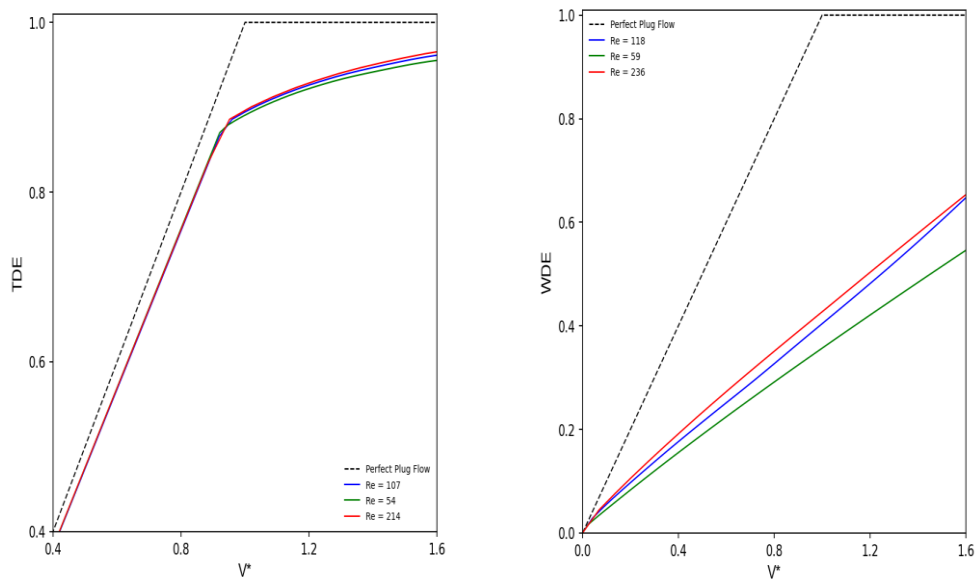


Figure 5-21. Effect from flow rate for the simulations with constant density displacing fluid (cases Constant #2, Constant #20, and Constant #22)

The final case simulated couples the eccentricity,  $45^\circ$  deviation angle and a lower viscosity ratio to evaluate the worst-case scenario.

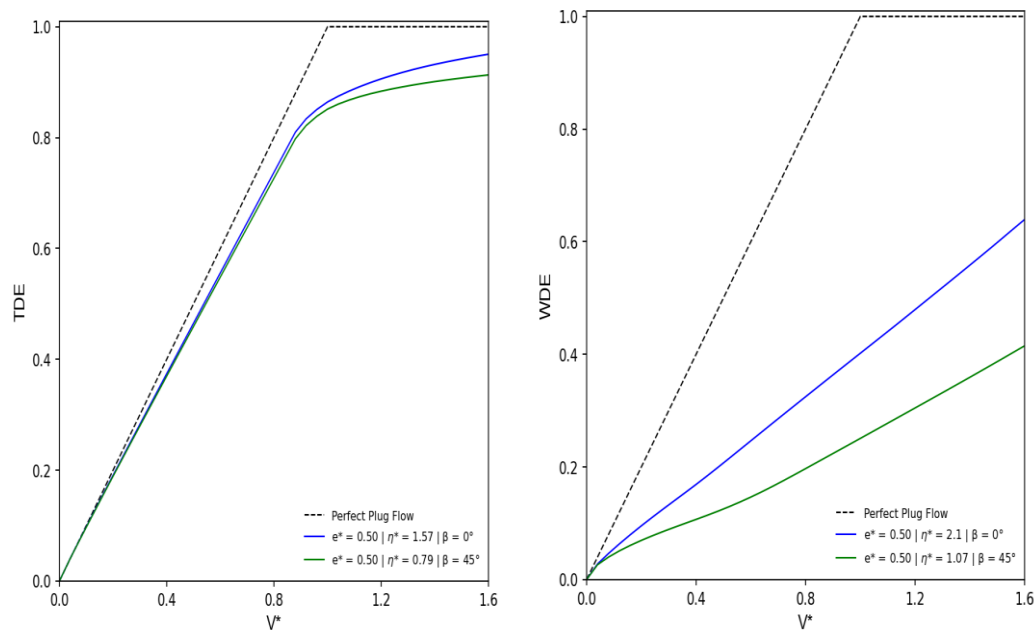


Figure 5-22. Results from eccentric base case ( $e^*=0.50$ ) and combined eccentric, inclined and with lower viscosity ratio for constant-density displacing fluid (cases Constant #4 and Constant #24)

The results are qualitatively consistent of the observed with the foamed fluid simulations for all the effects considered. In the quantitative side, all the efficiencies are slightly lower than the similar case with the foamed displacing fluid. The next section is dedicated to comparing the results for the two considerations.

### 5.3.

#### Comparison of systems from displacement perspective and important considerations

##### 5.3.1.

#### Displacement Efficiency comparison

In this section the displacement efficiency results (TDE and WDE) are compared directly from the simulations with a foamed and a constant-density displacing fluid. Table 5-5 contains the data that directs to the respective result of each effect considered.

Table 5-5. Source for comparison between foamed and unfoamed displacing fluid

<b>Effect</b>	<b>Source</b>
Eccentricity effect	Figure 5-23
Density contrast effect	Figure 5-24
Rheology and viscosity contrast effect	Table 5-6
Flow rate effect	Figure 5-25
Combined effect	Figure 5-26

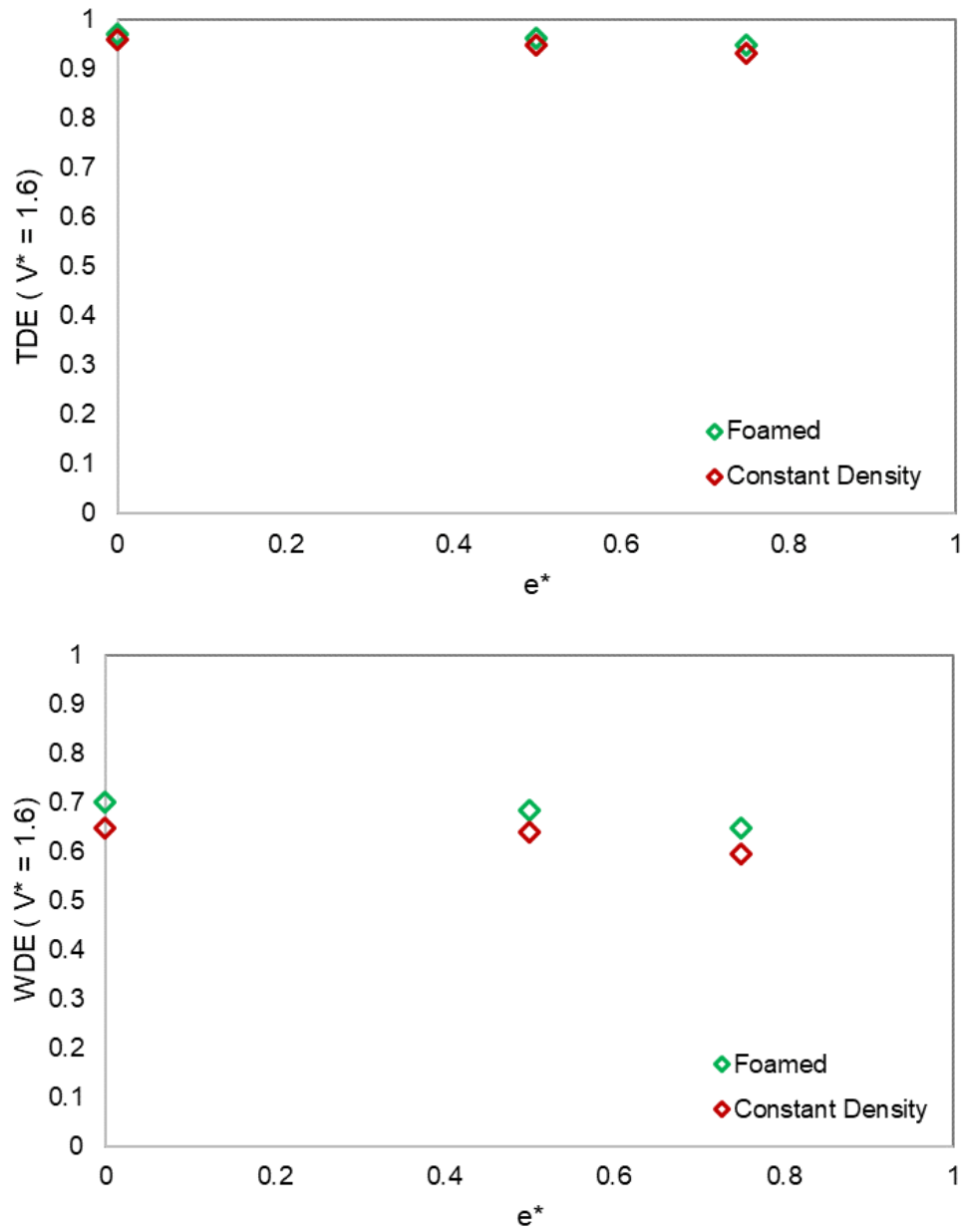


Figure 5-23. Eccentricity effect comparison

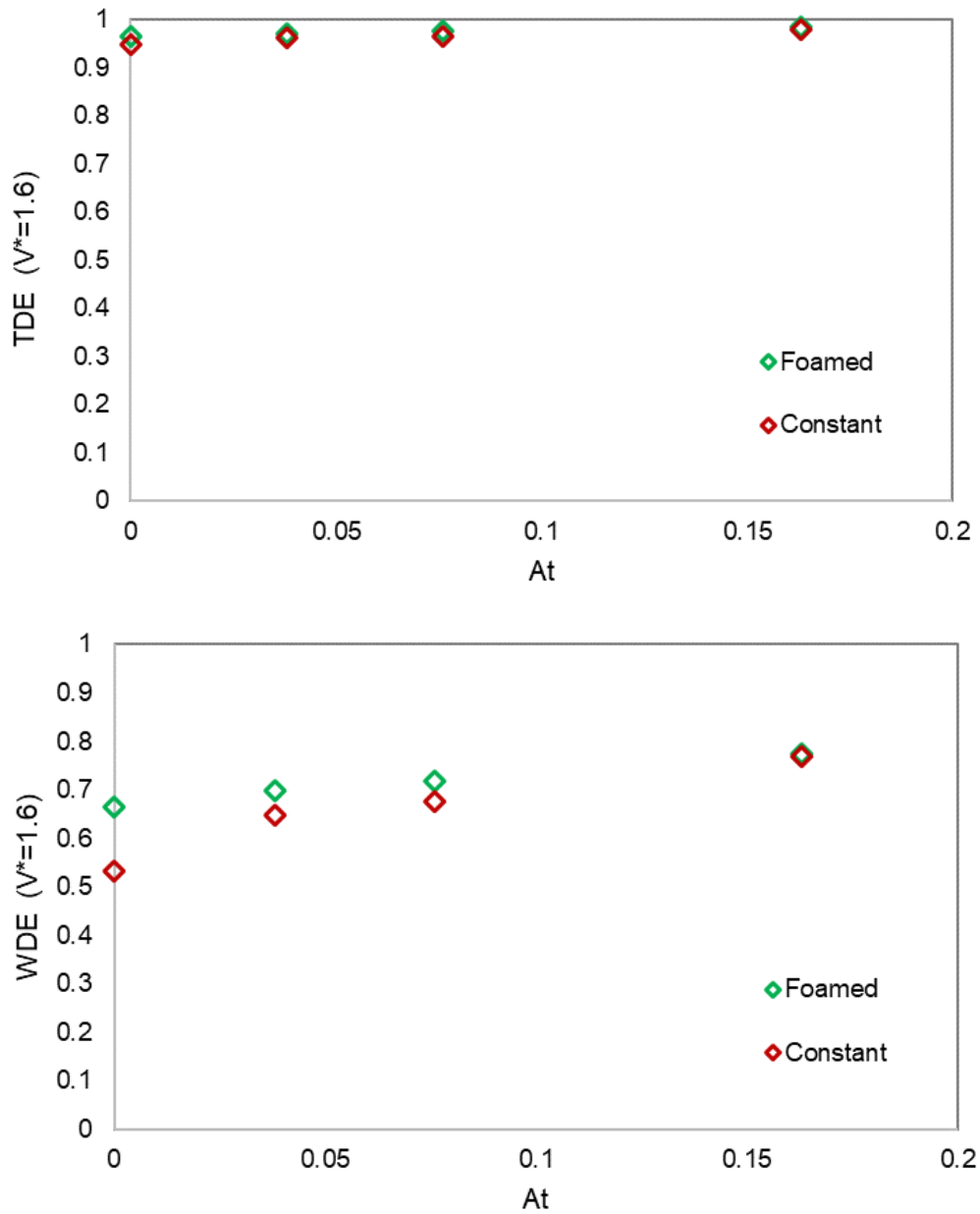


Figure 5-24. Density contrast comparison

Table 5-6. Rheology and viscosity contrast effect comparison

Foamed				Constant Density			
$\eta^*$	HB1	TDE	WDE	$\eta^*$	HB1	TDE	WDE
2.10	0.03	0.9717	0.6994	1.57	0.03	0.9613	0.6474
1.07	0.03	0.9391	0.3864	0.79	0.03	0.9341	0.3334
1.77	0.198	0.9763	0.7268	1.30	0.198	0.9743	0.7033

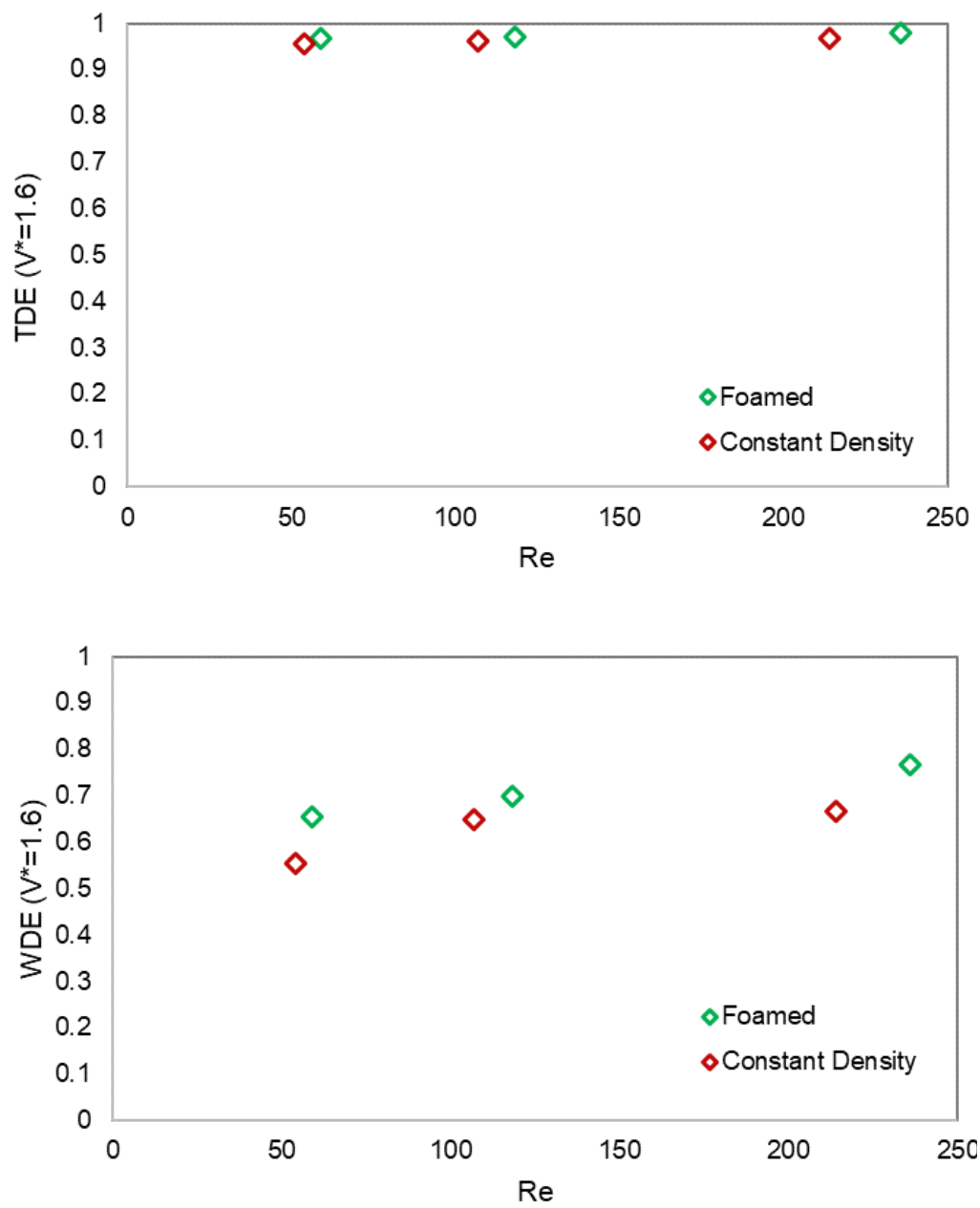


Figure 5-25. Comparison of efficiency from the effect of flow rate

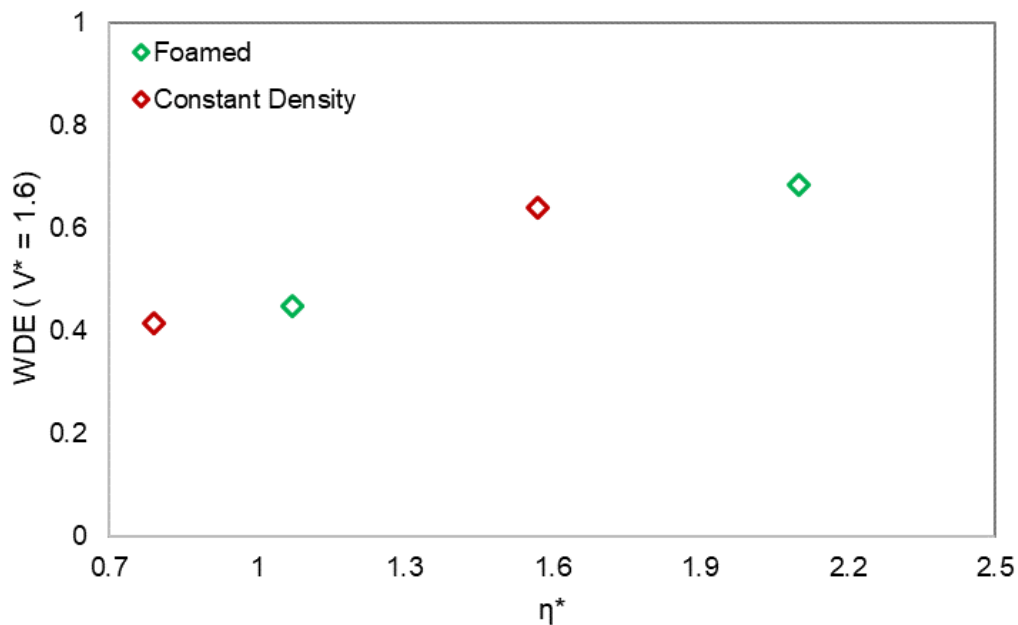
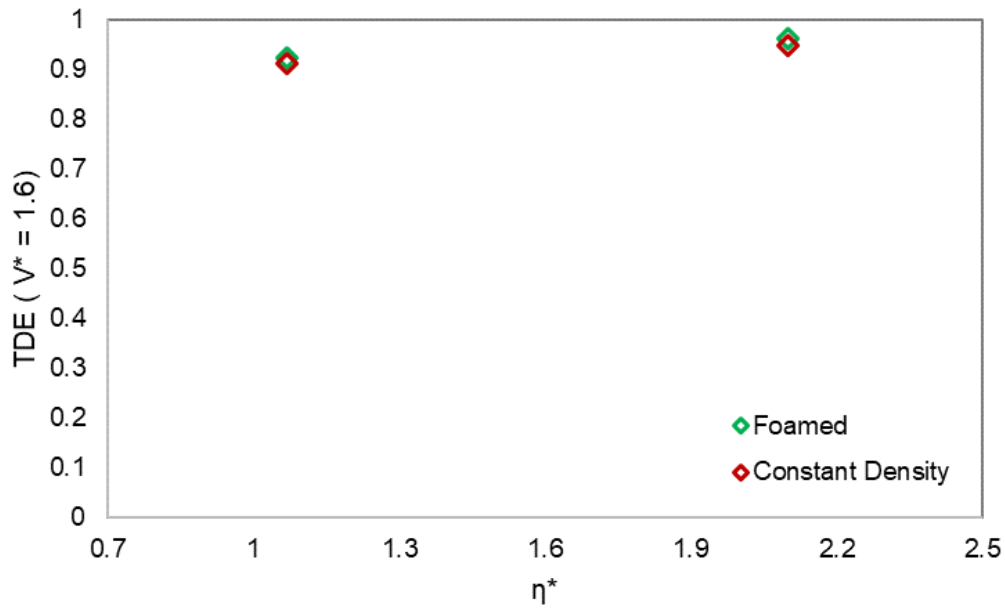


Figure 5-26. Comparison of efficiency from the combined effect of eccentricity and viscosity ratio

In all cases the foamed displacing fluid performs better than the constant-density displacing fluid with the same effect considered. The difference, however, is very small when the density and viscosity contrast are high enough to provide sufficient good-quality displacement process. This conclusion indicates that if the rheology and density of a constant-density spacer or cement slurry matches the foamed one, similar results will be found in the displacement efficiency.

### 5.3.2.

#### Channeling growth in eccentric annuli

This section compares the performance of the foamed and constant-density displacing fluids considering the channel development and growth in an eccentric annulus. The process will consider the difference between the position of the interface on the wide side and the narrow side of the annulus (Eq. 5-1).

$$CH_{Length} = (X_{int,wide} - X_{int,narrow}) \quad (\text{Eq. 5-1})$$

To get the interface position in each side (narrow and wide) of the annulus, the average density for every side is plotted, in a certain time step, throughout the length of the annulus. The interface position considered to be in the midpoint of the gap between the displaced and displacing fluid. Figure 5-27 shows the density profile in the annulus for  $V^* = 1.6$ , where the wide side average density (green) and narrow side average density (red) show a steep decrease in two different positions in the annulus. The blue curve in the left plot represents the concentric interface at the foamed fluid simulation. With this procedure, the interface position may be obtained for all simulation cases.

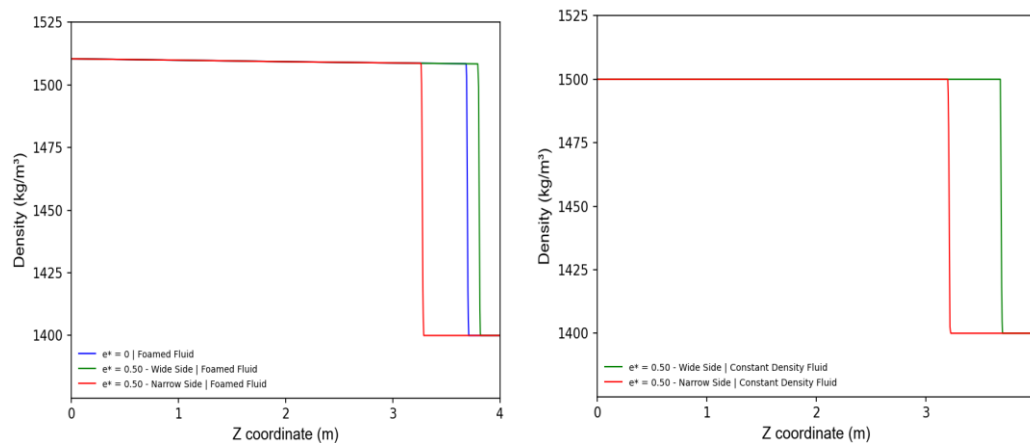


Figure 5-27. Density profile in annulus for foamed fluid simulation (left) and constant density (right), at  $V^* = 1.6$ .

The process may be repeated for different time-steps to catch the evolution of the interface in two sides of the annulus. Figure 5-28 shows the interface position for different dimensionless time-steps ( $V^*$ ).

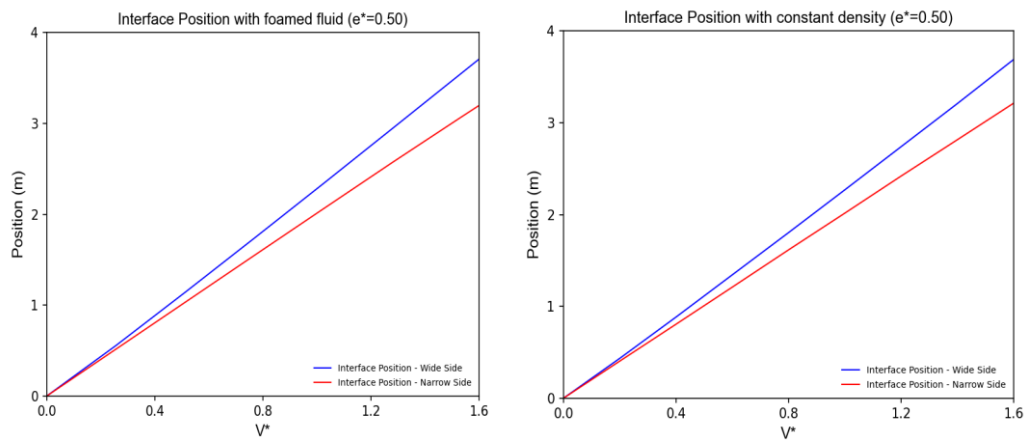


Figure 5-28. Interface Position in annulus for base case with  $e^*=0.50$ .

The channel may be obtained from Eq. 5-1 and plotted as Figure 5-29, where the markers are the data from the results from the simulations and the dashed lines are a quadratic fit for the channel growth.

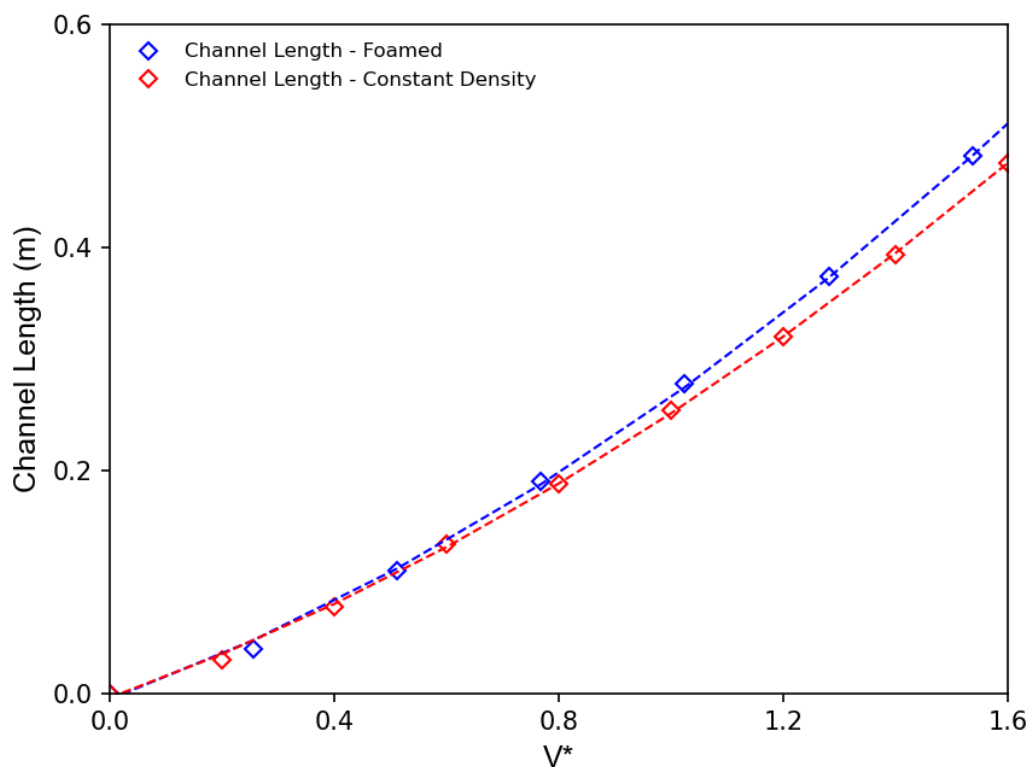


Figure 5-29. Channel length for base case simulation with  $e^*=0.50$  and  $\beta = 0$ .

The channel growth effect is also analyzed in the complex case with lower  $\eta^*$

and inclined geometry ( $\beta = 45^\circ$ ) with  $e^* = 0.50$ . Figure 5-30 and Figure 5-31 show, respectively, the interface position and the channel size for the foamed displacing fluid and constant density displacing fluid.

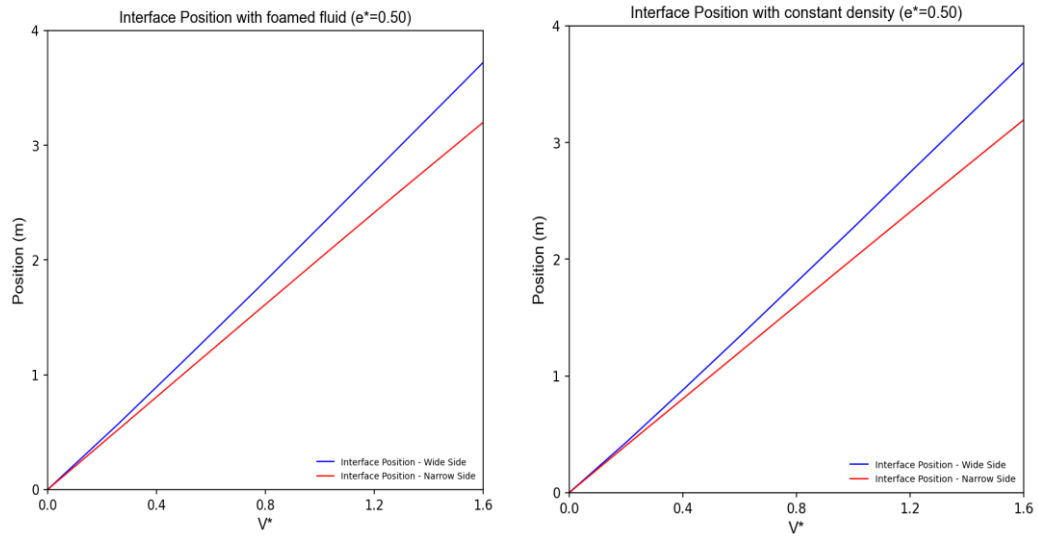


Figure 5-30. Interface Position in annulus for complex 3D case with  $e^* = 0.50$ .

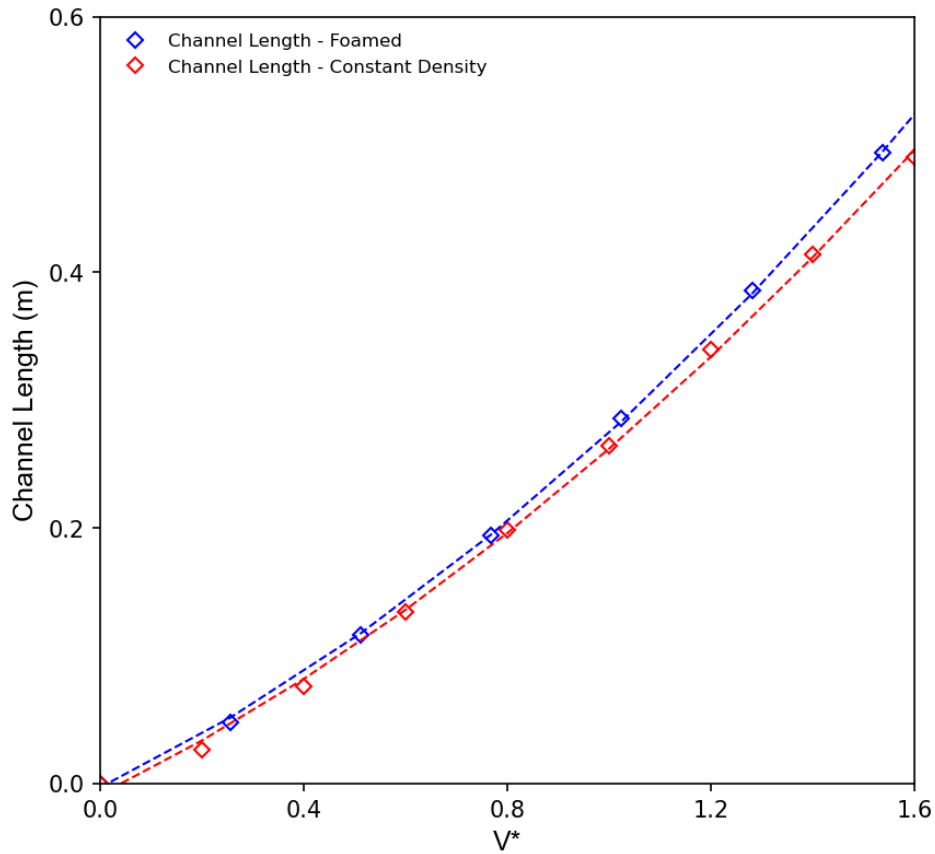


Figure 5-31. Channel length for complex case simulation with  $e^* = 0.50$  and  $\beta = 45^\circ$ .

When comparing both situations (Table 5-7), we see that the complex case (which has  $45^\circ$  deviation and a lower  $\eta^*$ ) present a slightly higher tendency to the growth of the channel. However, it has little influence if only the interface front is considered.

Table 5-7. Channel size at  $V^*=1.6$  for base case and complex case

	Channel Size for $V^* = 1.6$		Channel Size for $V^* = 50$ (extrapolated from quadratic fit)	
	Foamed displacing fluid	Constant- density displacing fluid	Foamed displacing fluid	Constant- density displacing fluid
<b>Base case</b> Channel Size (m)	0.528	0.476	224.505	195.53
<b>Complex case</b> channel size (m)	0.54	0.49	224.335	195.565

The results indicate that the displacement with foamed cement in eccentric annuli induces more channeling than the constant density lightweight cement with the same pumping parameters and base slurry rheology. This could be explained by the low expansion rate of the foamed fluid, where the velocity in the wide side of the annulus grows faster than the velocity in the narrow side, while the expansion increases when the displacing fluid is in a shallower depth.

With those considerations, well cementing engineers should account for the impact of increased channeling size in the annulus, which may be relevant in scenarios such as:

- Undesired higher top of cement (TOC) above previous casing shoes, impacting annular pressure build-up (APB) during well production;
- Increased length of partially cemented casing in front of mobile zones such as creeping salt or shale, which may increase the ununiform loads in the casing, leading to collapse failure;
- Not achieving proper zonal isolation on shallow inflow potential zones.

## 6

### Conclusions

This chapter summarizes the key findings from the research performed in this dissertation and the major contributions in the evaluation of well cementing systems performance.

2D and 3D models for multiphase, isothermal flow in an annular geometry with compressible, non-Newtonian fluids were developed with a proper customization of existing CFD open-source software. The results of the modeling were validated with known mathematical exact solutions for single-phase steady-state flow for the regularized Herschel-Bulkley, Power-Law and Newtonian constitutive relations and showed good agreement. In addition, the model presented agreement with the expected expansion of the foamed fluid in the upward flow through the annular space, consistent velocity profile in a centered and eccentric annulus. The isothermal simplification considered in the modeling did not impact the following conclusions, since the annular length domains analyzed were not large enough to be affected by major temperature change. However, if a long annular length is considered and simulated, this simplified model for the Equation of State may not be adequate.

The modeling is fully customizable for other geometric and fluid properties, becoming the first known 3D modeling capable of simulating displacement flow in annulus with foamed fluids, implemented from existing open-source codes. Therefore, further development to increase complexity of the flow may be obtained.

The modeling showed capacity for simulating real scale, with real drilling fluid and cement slurry properties, and can perform sensitivity and parametric analysis with multiple variations, such as well geometry (eccentricity, well deviation, density, flow rate, pressure, and different rheological models, and in case of the foamed fluids, different gas concentrations).

The real cases simulated focused in challenging well cementing scenarios typically found in deepwater wells with long cemented sections considered to minimize the number of phases in a well, which frequently limits the density contrast between the drilling fluid and the cement slurry to low values. In these

cases, the parametric simulations started from a base-case and then a dimensional analysis was performed with the selection of dimensionless parameters considering variations in the flow and fluid parameters. The main simulations considered a constant density drilling fluid as a displaced fluid and a foamed cement slurry (or spacer) as the displacing fluid.

The displacement efficiency was evaluated in the annular domain (volumetric) and in the walls (surfaces), and these were established as the key performance indicators. In the foamed cement simulations, the following conclusions are presented:

i. The base-case shows high volumetric displacement efficiencies regardless of the eccentricity, over 90%. However, the increase in the eccentricity in all cases leads inevitably to a channel forming in the narrow side of the annular geometry, where the size of the channel increases while the eccentricity increases. In addition, the displacement at the wall is more affected when eccentricity increases;

ii. The well deviation did not pose as significant impact for the displacement with a prescribed eccentricity. It should be noted that the deviation itself is a parameter that induces more eccentricity, but in this work this dependence relation was not considered;

iii. The change in the Reynolds number also showed a proper expected correlation where the increase in flow rate provided better displacement efficiencies, but the impact was lower than the impact of the density contrast and viscosity contrast;

iv. The viscosity contrast posed as a major factor for the volumetric and wall displacement efficiency, where the increase in the viscosity of foams was considered. The increase in density contrast also showed better results, as expected;

v. The correlation used to model the increase in the viscosity of the foamed fluid from the viscosity of the base fluid (unfoamed) showed a major influence in the wall displacement efficiency results. Therefore, the selection of a proper correlation that correctly considers the effect of the dispersed bubbles poses as a critical decision for the engineer;

vi. A simplified approach of modeling a foamed cement job with constant density and rheology fluids will underestimate the displacement

efficiency but may also underestimate the channel size.

Selected scenarios were also simulated to compare the displacement efficiencies if a constant density cement slurry (or spacer) was used instead of the foamed one. In these cases, the same base cement slurry (or spacer) rheological parameters were used, and the constant density is the inlet density of the foamed fluid. From the execution of those additional simulations, it can be concluded that:

vii. The constant (unfoamed) displacing fluid presented worse results in the displacement efficiencies in all the situations when a direct comparison was performed. However, when the volumetric displacement efficiencies are evaluated, a small difference can be observed between the cases;

viii. When the wall displacement efficiency is compared with foamed displacing fluids, the performance of the constant density displacing fluid is significantly lower than the foamed displacing fluid;

ix. The constant density (unfoamed) displacing fluid also showed a higher sensitivity in the displacement efficiency results in more challenging conditions. For example, a lower viscosity contrast and a higher eccentricity provided more impact (lower relative displacement efficiencies) than the impact that occurred with the foamed displacing fluid simulations.

x. In opposition of the previously reported results, the constant density displacing fluid showed a lower tendency for a channeling growth in the annulus. This result suggests that the expansion of the foamed displacing fluid does not influence the capacity of the coverage in the displacement process, as reported qualitatively by some authors.

The results and methodology presented in this dissertation may be used to provide a quantitative estimation method for the differences expected in the displacement efficiency process for well cementing operations when low-density cement slurries are needed. Such consideration may influence the decision on the selection of cement slurry and placement technique, as much as the parameters to be used.

Therefore, when considering the possibilities in a cementing design, a foamed cement strategy should be strongly recommended when there are severe limitations such as narrow viscosity and density contrast (because of a narrow

operational window), highly eccentric annulus, and flow rate limitations, due to the increase in the efficiency and a lower susceptibility of being impacted by the variables. This is a significant addition to the other advantages of the foamed cementing systems. Conversely, if the conditions for cementing are simple, both cementing systems will provide similar expected results.

## 6.1

### **Future work proposals**

As future developments following this work, some possibilities may explore the better understanding of the rheological behavior of cement slurries under field conditions, using experimental procedures to obtain better rheological characterization and/or to consider the heat transfer effects.

In the first, the correlation considered for the foamed cement posed as one of the main variables that influence the displacement efficiency, and therefore, a proper selection of a method to correlate and estimate the variation in the transport properties is a critical step. The literature and industry's techniques for proper measurement methods for the foamed fluids under field conditions - high pressure and temperature – are still on development, however significant improvements have been made in the past 10-15 years. The unfoamed cement slurry rheological properties are much more practical to be measured in the daily basis, and therefore, the development of methods to correlate the behavior of the foamed cement with the unfoamed base cement slurry are of particular importance to the cementing engineer.

Second, the work in this dissertation considered isothermal flow in the annular geometry. As the length of the annulus in the simulations were small (less than ten meters) in comparison of field real cementing operations (which are of hundreds or thousands of meters), this effect could be neglected. However, in larger geometries, temperature variations in the annulus should be considered during the flow, and additionally nitrogen should be treated as a real gas with a temperature-dependent compressibility factor, to avoid larger errors. These considerations would also be necessary for the multiphase flow inside the tubular geometry, which is part of the cementing operation.

Besides these, other improvements of the modeling might be implemented to study the benefits of the use of foams in several other applications in the oil and gas industry, such as hydraulic fracturing, drilling, and plugging and abandonment.

## Bibliography

- [1] International Energy Agency (IEA). **World Energy Outlook 2022**.
- [2] API Standard 65-2. **Isolating Potential Flow Zones During Well Construction**. Second Edition, American Petroleum Institute, 2010.
- [3] API Standard 65-1. **Cementing Shallow-water Flow Zones in Deepwater Wells**. Second Edition, American Petroleum Institute, 2018.
- [4] API RP 10B-4. **Preparation and Testing of Foamed Cement Formulations at Atmospheric Pressure**. Second Edition, 2015. Washington D.C.: API.
- [5] Davies, D.R, Hartog, J. **Foamed cement - a cement with many applications**. Proceedings of the Middle East Oil Technical Conference of the Society of Petroleum Engineers held in Manama, Bahrain, March 9-12, 1981.
- [6] Odden, D.A., Lende, G., Rehman, K., Liledal, L., Smyth, C., Diesen, M., Bjørnstad, L., Laget, M. **Use of Foam Cement to Prevent Shallow Water Flow on Three Wells in Norwegian Waters**. Proceedings of the International Petroleum Technology Conference held in Dhahran, Saudi Arabia, 13 – 15 January 2020.
- [7] Ahmady, A. Turton, S. and Lewis, S. Grant, M., Murphy, B. **Improved Channeling and Gas Migration Issues Using Foam Cement: CaseHistory, Montney Formation**. Paper presented at the IADC/SPE International Drilling Conference and Exhibition, Galveston, 2020.
- [8] Stiles, D.A. **Successful Cementing in Areas Prone to Shallow Saltwater Flows in Deep-Water Gulf of Mexico**. Paper presented at the Offshore Technology Conference, Houston, Texas, May 1997.
- [9] D. Glosser, B. Kutchko, G. Benge. Crandall, M.T. Ley. **Relationship between operational variables, fundamental physics and foamed cement properties in lab and field generated foamed cement slurries**. Journal of Petroleum Science and Engineering, Volume 145, 2016.
- [10] Dalton, L. E., Brown, S., Moore, J., Crandall, D., and Magdalena G. **Laboratory Foamed-Cement-Curing Evolution Using CT Scanning: Insights from Elevated-Pressure Generation**. SPE Drilling & Completions 34, 2019.

- [11] Cunningham, E., Heathman, J., Kutchko, B., Bengel, G., Maxson, J., DeBruijn, G., Buford, C. **Defining the Difference Between Laboratory and Field-Generated Foamed Cement**. Paper presented at the Offshore Technology Conference, Houston, Texas, USA, May 2017.
- [12] Kutchko, Barbara, Crandall, Dustin, Moore, Johanthan, Gill, Magdalena, Haljasmaa, Igor, Spaulding, Richard, Harbert, William, Bengel, Glen, DeBruijn, Gunnar, and Joe Shine. **Assessment of Foamed Cement Used in Deep Offshore Wells**. Paper presented at the SPE Deepwater Drilling and Completions Conference, Galveston, Texas, USA, September 2014.
- [13] Vineet Sinha, Ramadan Ahmed, Tarek Akhtar, Subhash Shah, Mahmood Amani. **Rheology and hydraulics of polymer-based foams at elevated temperatures**. Journal of Petroleum Science and Engineering, Volume 180, 2019.
- [14] R.M. Ahmed, N.E. Takach, U.M. Khan, S. Taoutaou, S. James, A. Saasen, R. Godøy. **Rheology of foamed cement**. Cement and Concrete Research, Volume 39, Issue 4, 2009.
- [15] Mitchell, B.J. **Test Data Fill Theory Gap on Using Foam as a Drilling Fluid**. Oil and Gas Journal, pp. 96-100, 1971.
- [16] Batchelor, G., Green, J. **The determination of the bulk stress in a suspension of spherical particles to order  $c_2$** . Journal of Fluid Mechanics, 56(3), 401-427, 1972.
- [17] Ducloué L, Pitois O, Goyon J, Chateau X, Ovarlez G, 2015. **Rheological behaviour of suspensions of bubbles in yield stress fluids**. Journal of Non-Newtonian Fluid Mechanics, Vol. 215, pp. 31–39.
- [18] Blandine Feneuil, Nicolas Roussel, Olivier Pitois. **Yield stress of aerated cement paste**. Cement and Concrete Research, Volume 127, 2020.
- [19] Enayatpour, S., Oort, E., 2017. **Advanced Modeling of Cementing Complexities**. Paper presented at the IADC/SPE International Drilling Conference and Exhibition, The Hague, The Netherlands.
- [20] Foroushan, H. K., Lund, B., Ytrehus, J.D., Saasen, A. **Cement Placement: An Overview of Fluid Displacement Techniques and**

**Modelling.** Energies, Vol.14, 573, 2021.

[21] Guillot, Dominique Jean; Bastard, Eve L., 2012. **Learnings from Foamed Cement Job Simulations.** Paper presented at the Offshore Technology Conference, Houston, Texas, USA.

[22] Grinchik, I. P. and Kim, A. Kh., 1974. **Axial flow of a nonlinear viscoplastic fluid through cylindrical pipes.** Journal of engineering physics, Vol. 23, pp. 1039–1041.

[23] Hanks, Richard W., 1979. **The Axial Laminar Flow of Yield-Pseudoplastic Fluids in a Concentric Annulus.** Industrial & Engineering Chemistry Process Design and Development, Vol. 18, pp. 488–493.

[24] Hanachi, N., Maleki, A., Frigaard, I., 2018. **A model for foamed cementing of oil and gas wells.** Journal of Engineering Mathematics, Vol. 113, pp. 93–121.

[25] Nelson, E.B., Guillot, D., 2006. **Well Cementing**, Second Ed. Schlumberger, Sugar Land, Texas, US.

[26] Olowolagba, K.; Brenneis, C., 2010. **Techniques for the Study of Foamed Cement Rheology.** Paper presented at the SPE Production and Operations Conference and Exhibition, Tunis, Tunisia.

[27] Rosenbaum, E., Massoudi, M., Dayal, K., 2019. **The Influence of Bubbles on Foamed Cement Viscosity Using an Extended Stokesian Dynamics Approach.** Fluids, Vol. 4, pp. 166.

[28] Becker, T.E., Morgan, R.G., Chin, W.C., Griffif, J.E. **Improved rheology model and hydraulics analysis for tomorrow's wellbore fluid applications.** Paper presented at the SPE Productions and Operations Symposium, Virtual, 2003.

[29] Skadsem, H. J., Kragseta, S., Lundb, B., Ytrehusb, J.D., Taghipourb, A., 2019. **Annular displacement in a highly inclined irregular wellbore: Experimental and three-dimensional numerical simulations.** Journal of Petroleum Science and Engineering, Vol. 172, pp. 998-1013.

[30] P.R. Vargas, E.C. Rodrigues, L.C. Moraes, P.R. de Souza Mendes, M.F. Naccache. **Flow instabilities in fluid displacement through enlarged regions in annular ducts.** Journal of Non-Newtonian Fluid Mechanics, Volume 305, 2022.

- [31] Phadke, A., Hovda, L., Gonuguntla, P., Mueller, D. **Application of Computational Fluid Dynamics for Parametric Optimization of Jet-Type P/W/C Technique**. Paper presented at the SPE Asia Pacific Oil & Gas Conference and Exhibition, Virtual, November 2020.
- [32] Enayatpour, S., Oort, E. **Advanced Modeling of Cement Displacement Complexities**. Paper presented at the SPE/IADC Drilling Conference and Exhibition, The Hague, The Netherlands, March 2017.
- [33] A.-P. Bois; H. Zhao; D. Wen; Y. Luo; Y. Li; A. M. Badalamenti; M. Song; C. Calvo; J. Reñe; H. Liang. **Cement Placement Modeling—A Review**. SPE Drill & Compl 38 (02): 342–357.
- [34] Sheriff, T., Ahmed, R., Shah, S., Amani, M., 2016. **Rheology of Oil-Based Drilling Foams**. Paper presented at the AADE Fluids Technical Conference and Exhibition At: Houston, Texas, USA.
- [35] Sinha, V., Ahmed, R., Akhtar, T., Shah, S., Amani, M., 2019. **Rheology and hydraulics of polymer-based foams at elevated temperatures**. Journal of Petroleum Science and Engineering, Vol. 180, pp. 330-346.
- [36] Westermaier, S., Kowalczyk, W., 2020. **Implementation of Non-Newtonian Fluid Properties for Compressible Multiphase Flows in OpenFOAM**. Open Journal of Fluid Dynamics, Vol. 10, pp. 135-150.
- [37] Brill, James P. **Multiphase Flow in Wells**. Henry L. Doherty Memorial Fund of AIME, Society of Petroleum Engineers, Richardson, Tex, 1999.
- [38] F. Moukalled M., L. Mangani, Darwish F, **The Finite Volume Method in Computational Fluid Dynamics: An Advanced Introduction with OpenFOAM and MATLAB**, Springer, 2015.
- [39] Hacıislamoglu, M. and Langlinais, J. **Non-Newtonian flow in eccentric annuli**. Journal of Energy Resources, pp 163,169, 1990.
- [40] Bailey, W. J., and Peden, J. M. **A Generalized and Consistent Pressure Drop and Flow Regime Transition Model for Drilling Hydraulics**. SPE Drill. Completion, 15(1), pp. 44–56, 2000.
- [41] Passos, A. G. L. G., Menezes, G. M. R., Lima, F. M., Piedade, T., Geraci, L. C. M., Peralta Moreira, R., and G. I. M. dos Reis. **"Reduction of Well Construction Time with Innovative Design: Tot-3p (True One Trip**

- **3 Phases).**" Paper presented at the Offshore Technology Conference, Houston, Texas, USA, May 2023.

[42] Ferreira, F. K., Fiorotti, J., Brunherotto, L., Cunha, M., Paredes, Jose L., Piedade, T., Peralta, R., and Filho, G. **"Tailored Dependable Barrier Enables Operator to Flawlessly Complete True One Trip Ultra Slender Deepwater Well."** Paper presented at the International Petroleum Technology Conference, Riyadh, Saudi Arabia, February 2022.

[43] Kim Niggemann, K., Samuel, A., Morriss, A., Hernández, R. **"Foamed Cementing Geothermal 13 3/8-in. Intermediate Casing: NGP #61-22"**. Proceedings World Geothermal Congress, 2010.

[44] Okagaki, Y.; Yonomoto, T.; Ishigaki, M.; Hirose, Y. **Numerical Study on an Interface Compression Method for the Volume of Fluid Approach.** Fluids 2021, 6, 80.

[45] CENPES/PDDP/PCP. **SIMENTAR 2.5 – Projeto hidrostático e simulação hidráulica de fluidos espumados.** July 2017.

[46] H. Garcia Jr. **Estudo de pressões de bombeio durante as operações de cimentação com pastas espumadas.** Master's thesis, Universidade Estadual de Campinas, Campinas, 1992.

[47] Terra, F.S., Moreira, R.P.M, Moreno, G.V., Campos, G. Domingues, R.S. **Numerical simulation as a driver of the pumping strategy through the tubing using foamed fluids for plug and abandonment operation.** Rio Oil and Gas Expo and Conference, v. 20, p. 147-148, 2020.

[48] Kalyanraman, R.S., Chen, X., Wu, P., Constable, K., Govil, A., and A. Abubakar. **Autonomous Interpretation Methods of Ultrasonic Data Through Machine Learning Facilitates Novel and Reliable Casing Annulus Characterization.** Paper presented at the SPE/IADC International Drilling Conference and Exhibition, Virtual, March 2021

## Nomenclature

$A$  – Area of a section

$A_t$  – Atwood Number

$\alpha_i$  – Phase volumetric concentration of phase  $i$

BHCT – Bottom Hole Circulating Temperature

Casing – Steel tubular

$D_h$  – Hydraulic Diameter

$e$  - Casing eccentricity

$e^*$  - Dimensionless eccentricity

EoS – Equation of State

$F_{st}$  – Surface Tension Force

$HB_{Ni}$  – Herschel Bulkley Number for fluid  $i$

$\dot{m}$  – Mass flow rate

$\eta^*$  - Dimensionless Viscosity Ratio

$p$  – Pressure

$\rho_i$  – Density of Fluid  $i$

$\rho_b$  – Density of base fluid

$\rho_{g,STD}$  – Density of gas at standard conditions

$\rho_g$  – Density of gas at field conditions

$\rho_f$  – Density of foamed fluid

Re – Reynolds Number

$t$  – time

$V^*$  - Dimensionless pumped volume

$\vec{U}$  – Velocity vector

$\eta$  – Viscosity Function

$\phi$  – Gas volume fraction

$\bar{\gamma}$  – Shear Rate Tensor

$|\dot{\gamma}|$  – Shear Rate Magnitude

$\dot{\gamma}_c$  – Characteristic Shear-rate of the flow

SOR – Stand-off ratio

$\bar{\tau}$  – Shear Stress Tensor

$\tau_y$  – Yield Stress of fluid

$\tau_w$  – Shear stress at the wall

TOC – Top of Cement

TDE – Total Displacement Efficiency

VOF – Volume of Fluid

$GLR_{STD}$  – Gas-liquid volumetric ratio at standard conditions

WDE – Wall Displacement Efficiency

## Appendix A – New Solver Compilation

In the case of this work, the desired models for the fluid density as a function of pressure and a gas-liquid ratio and non-Newtonian Power-Law and Herschel-Bulkley models also depending on the gas-liquid ratio are not between the pre-compiled templates for the *compressibleInterFoam* solver. Thus, a new solver was compiled to include used defined functions.

In OpenFOAM v9, the transport and thermodynamic properties are linked to the “Base Class” *fluidThermo*. A new “Child Class” was created and named *cimThermo* to comprise the new models to be used in this dissertation, as shown in Figure A-1. This new “Child Class” will call the functions that will calculate the thermophysical properties in the elements and its boundaries.

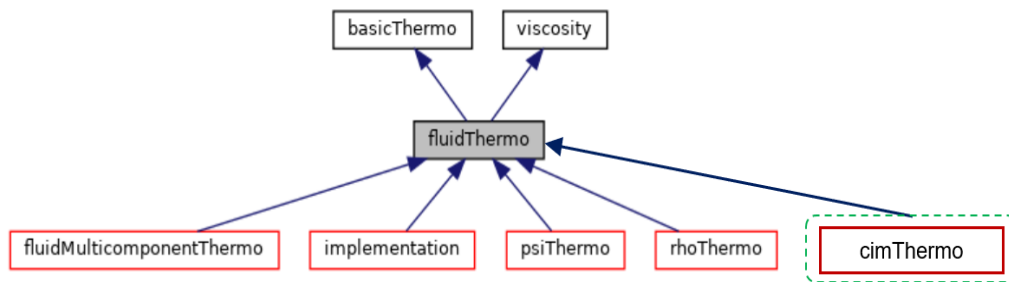


Figure A-1. Child class created *cimThermo* for the thermodynamical properties

This class will include the package of thermophysical modelling that will be used in the simulations. The steps described briefly in Figure 3-4 are more detailed to allow for new developed solvers to follow the same procedure.

### Step 1 – Source code for the equations of state

The Header and Main Files (.H and .C) for the definition of the new equation of state shall be written to include all the necessary variables to define the fluid properties.

The class *cimFoam* was defined and included in the dictionary of the Equations of State, and the two variables *rho0* (density of the base fluid) and *GLR* (gas-liquid ratio) were defined as scalars to be provided by the user. The *cimFoam.C* file is

described as follows as example.

```

\*-----*/
#include "cimFoam.H"
#include "IOstreams.H"
// * * * * * Constructors * * * * *
template<class Specie>
Foam::cimFoam<Specie>::cimFoam(const dictionary& dict)
:
    Specie(dict),
    GLR_(dict.subDict("equationOfState").lookup<scalar>("GLR")),
    rho0_(dict.subDict("equationOfState").lookup<scalar>("rho0"))
{}
// * * * * * Member Functions * * * * *
template<class Specie>
void Foam::cimFoam<Specie>::write(Ostream& os) const
{
    Specie::write(os);

    dictionary dict("equationOfState");
    dict.add("GLR", GLR_);
    dict.add("rho0", rho0_);

    os << indent << dict.dictName() << dict;
}
// * * * * * Ostream Operator * * * * *
template<class Specie>
Foam::Ostream& Foam::operator<<(Ostream& os, const
cimFoam<Specie>& pf)
{
    pf.write(os);
    return os;
}
// * * * * *

```

To call for the density, the header file *cimFoam.H* include the density function as follows.

```

//- Return density [kg/m^3]
inline scalar rho(scalar p, scalar T) const;

```

Where the function calculation is described in the initialization file *cimFoamI.H* with the model defined in Eq. 3-13 and Eq. 3-14. As expressed in the “Future Work” section, the use of the temperature dependence could be considered if the energy equations are solved and passed for each cell and boundary.

```

// * * * * * Member Functions * * * * *
* * * * * //

template<class Specie>
inline Foam::scalar Foam::cimFoam<Specie>::rho(scalar p, scalar T)
const
{

```

```

    const scalar qual = ((101035/p)*GLR_)/(1+(101035/p)*GLR_); //
DECLARAR FUNCAO QUALIDADE

    return rho0_ - qual*(rho0_ - 1.2506*p/101035);
}

```

## Step 2 – Source code for the viscosity models

Like in the case of the equations of state, the Header, and Main Files (.H and .C) for the definition of the new transport models had to be created. In this case, the *herschelbulkleyTransport* class will serve as an example. The input data (regularization parameter, yield stress, consistency index, behavior index and gas liquid ratio) are declared as input to be provided by the user at each simulation.

The *herschelbulkleyTransport.C* file is described as follow.

```

\*-----*/
#include "herschelbulkleyTransport.H"
#include "Iostreams.H"
// * * * * * Private Member Functions * * * * *
template<class Thermo>
Foam::scalar Foam::herschelbulkleyTransport<Thermo>::readCoeff
(
    const word& coeffName,
    const dictionary& dict
)
{
    return dict.subDict("transport").lookup<scalar>(coeffName);
}
// * * * * * Constructors * * * * *
template<class Thermo>
Foam::herschelbulkleyTransport<Thermo>::herschelbulkleyTransport(c
onst dictionary& dict):
    Thermo(dict),
    mu0_(readCoeff("mu0", dict)),
    tau0_(readCoeff("tau0", dict)),
    ka_(readCoeff("ka", dict)),
    n_(readCoeff("n", dict)),
    GLR_(readCoeff("GLR", dict)),
    rPr_(1.0/dict.subDict("transport").lookup<scalar>("Pr"))
{}
// * * * * * Member Functions * * * * *
template<class Thermo>
void Foam::herschelbulkleyTransport<Thermo>::write(Ostream& os)
const
{
    os << this->specie::name() << endl
        << token::BEGIN_BLOCK << incrIndent << nl;
    Thermo::write(os);
    dictionary dict("transport");
    dict.add("mu0", mu0_);
    dict.add("tau0", tau0_);
    dict.add("ka", ka_);
    dict.add("n", n_);
}

```

```

dict.add("GLR", GLR_);
dict.add("Pr", 1.0/rPr_);

os << indent << dict.dictName() << dict
  << decrIndent << token::END_BLOCK << nl;
}
// * * * * * Iostream Operators * * * * * //
template<class Thermo>
Foam::Ostream& Foam::operator<<
(
  Ostream& os,
  const herschelbulkleyTransport<Thermo>& plt
)
{
  plt.write(os);
  return os;
}
// * * * * * //

```

The member function for the dynamic viscosity defined in the header file *herschelbulkleyTransport.H* needs to include the strain-rate variable (scalar *sr*), which is not present in any of the implemented models in the *compressibleInterFoam* solver.

```

//- Dynamic viscosity [kg/m/s]
inline scalar mu(const scalar p, const scalar T, const scalar sr)
const;

```

The initialization file *herschelbulkleyTransportI.H* includes the returned value for the dynamic viscosity with the model defined in Eq. 3-13 and 3-20.

```

template<class Thermo>
inline Foam::scalar Foam::herschelbulkleyTransport<Thermo>::mu
(
  const scalar p,
  const scalar T,
  const scalar sr
) const
{
  const scalar qual = ((101035/p)*GLR_)/(1+(101035/p)*GLR_); //
DECLARAR FUNCAO QUALIDADE
  const scalar kanew = ka_*pow(((5+3*qual)/(5-2*qual)),
(n_+1)/2)*pow((1-qual), 0.5 - n_); // ATUALIZA ka
  const scalar tynew = tau0_*sqrt(max((1-qual)*(5+3*qual)/(5-
2*qual), scalar(0))); // ATUALIZA tau0

  return min
  (
    mu0_,
    // (tau0_ + ka_*pow(max(sr, 0.0000000001),
n_))/(max(sr, 0.0000000001))
    (tynew+ kanew*pow(sr, n_))/(max(sr, 0.0000000001))
  )
}

```



```

}
//
*****
***** //

```

#### Step 4 – Edit thermophysical loops

The *hecimThermo.C* include the calculation of the strain-rate that will be needed to to calculation of the dynamic viscosity in the functions defined in the Step 2. Thus, the first step is to access the velocity vector and then calculate the strain-rate magnitude as per Eq. 3-16.

```

// ***** Private Member Functions ***** //
template<class BasicPsiThermo, class MixtureType>
void Foam::hecimThermo<BasicPsiThermo, MixtureType>::calculate()
{
    const scalarField& hCells = this->he();
    const scalarField& pCells = this->p_;
    /*
    ***** */
    // BUSCA PELO PERFIL DE VELOCIDADE
    const volVectorField& U = this-
>db().objectRegistry::lookupObject<volVectorField>("U");
    // TERMINADA BUSCA PELO PERFIL DE VELOCIDADE
    /*
    ***** */
    // CALCULA A TAXA DE DEFORMACAO
    volScalarField sr_ = sqrt(scalar(2))*mag(symm(fvc::grad(U)));
    // TERMINA CALCULO DA TAXA DE DEFORMACAO
    /*
    ***** */

```

The second step is to calculate the strain-rate field in each cell and to calculate the dynamic viscosity passing the information of the cell's pressure, temperature, and strain-rate magnitude.

```

// CALCULA CAMPO DE TAXA DE DEFORMACAO
    scalarField& srCells = sr_.primitiveFieldRef();

muCells[celli] = mixture_.mu(pCells[celli], TCells[celli],
srCells[celli]);

```

The process will be repeated for the calculation of the dynamic viscosity in the boundaries of the cells as follows.

```

// CALCULA O CAMPO DA TAXA DE DEFORMACAO NA FRONTEIRA DA CELULA
volScalarField::Boundary& srBf =
sr_.boundaryFieldRef();

```

```
fvPatchScalarField& psr = srBf[patchi]; // CALCULA EM CADA
FRONTEIRA

pmu[facei] = mixture_.mu(pp[facei], pT[facei], psr[facei]);
```

The *mixture\_.mu* is a function calculated by the weighted average of the viscosity of each fluid by the concentration, and the dynamic viscosity of each fluid will follow from the result of the model selected as per Step 2.

```
mu_ = alpha1()*thermo1_->mu() + alpha2()*thermo2_->mu();
alpha_ = alpha1()*thermo1_->alpha() + alpha2()*thermo2_->alpha();
```

### Step 5 – Edit main solver file to update mixture properties before solving equations.

This step is very straightforward. In the pressure-velocity solving loops, the mixture properties shall be updated before every loop. This step does not exist in the unchanged *compressibleInterFoam.C* solver because the dynamic viscosity does not change with the velocity profile, which is the case for the non-Newtonian models considered.

The function *mixture.correct()* as shown below will be called before every iteration.

```
void Foam::cimmtwoPhaseMixtureThermo::correct()
{
    thermo1_->correct(); // ATUALIZAR AS PROPRIEDADES DA FASE
    ANTES DE ALTERAR A MISTURA
    thermo2_->correct(); // ATUALIZAR AS PROPRIEDADES DA FASE
    ANTES DE ALTERAR A MISTURA

    psi_ = alpha1()*thermo1_->psi() + alpha2()*thermo2_->psi();
    mu_ = alpha1()*thermo1_->mu() + alpha2()*thermo2_->mu();
    alpha_ = alpha1()*thermo1_->alpha() + alpha2()*thermo2_-
    >alpha();

    interfaceProperties::correct();
}
```

### Step 6 – Compile new solver.

The new solver (named *Cimento.C*) shall be compiled including all the files described in this section. In the *Make* folder, the compilation instructions will be updated considering the modified solver and thermophysical models.

Files (the folder that includes all the models created and modified is highlighted in blue):

```
cimento.C
I$(WM_PROJECT_USER_DIR)/applications/solvers/cimento/needforciment
o/modelos/cimThermos.C
I$(WM_PROJECT_USER_DIR)/applications/solvers/cimento/needforciment
o/modelos/cimThermo.C
EXE = $(FOAM_USER_APPBIN)/cimento
```

Options (the folder that includes all the models created and modified is highlighted in blue):

```
EXE_INC = \
-I. \
-IcimtTwoPhaseMixtureThermo \
-
I$(WM_PROJECT_USER_DIR)/applications/solvers/cimento/needforciment
o/modelos \
-IvoFphaseCompressibleMomentumTransportModels/lnInclude \
-I$(LIB_SRC)/thermophysicalModels/basic/lnInclude \
-I$(LIB_SRC)/thermophysicalModels/specie/lnInclude \
-I$(LIB_SRC)/twoPhaseModels/twoPhaseMixture/lnInclude \
-I$(LIB_SRC)/twoPhaseModels/interfaceProperties/lnInclude \
-
I$(LIB_SRC)/MomentumTransportModels/momentumTransportModels/lnIncl
ude \
-I$(LIB_SRC)/MomentumTransportModels/compressible/lnInclude \
-
I$(LIB_SRC)/MomentumTransportModels/phaseCompressible/lnInclude \
-I$(LIB_SRC)/meshTools/lnInclude \
-I$(LIB_SRC)/dynamicMesh/lnInclude \
-I$(LIB_SRC)/dynamicFvMesh/lnInclude \
-I$(LIB_SRC)/finiteVolume/lnInclude

EXE_LIBS = \
-L$(FOAM_USER_LIBBIN) \
-lcimtTwoPhaseMixtureThermo \
-ltwoPhaseSurfaceTension \
-lfluidThermophysicalModels \
-lspecie \
-ltwoPhaseMixture \
-ltwoPhaseProperties \
-linterfaceProperties \
-lmomentumTransportModels \
-lfluidThermoMomentumTransportModels \
-lcimVoFphaseCompressibleMomentumTransportModels \
-lfiniteVolume \
-lfvOptions \
-lmeshTools \
-ldynamicMesh \
-ldynamicFvMesh
```

## Appendix B – Validation of steady-state single-phase flow

For non-Newtonian Yield-stress fluids, an exact solution may be derived to solve the laminar, compressible single-phase steady-state flow in a concentric annulus to be used to validate the numerical solution of a developed numerical simulation. This appendix shows the process used to generate the exact solution for compressible flow.

*Grinchik and Kim* (1974) and Hanks and Richard (1979) developed exact solutions for slit geometry – that may be used with good precision in small gaps – and for annular geometry, respectively.

Assuming steady-state flow, the density in every depth in the annulus does not vary with time, thus  $\dot{m} = \rho A_T \bar{U} = \dot{m}_{inlet}$ , and  $\vec{U} = (0, 0, u(y, z))$ .

With a known boundary condition  $p(z_0) = P_0$ , it follows that  $\bar{U}(z_0) = \frac{\dot{m}}{A_T \cdot \rho(P_0)}$  and thus, the average velocity may be expressed as  $\bar{U}(z) = \frac{\bar{U}(z_0) \cdot \rho(P_0)}{\rho(p(z))}$ .

Using the above expression for the average velocity in the linear momentum equation in the Z direction, the expression for the pressure gradient will generate an initial value differential equation.

$$\frac{\partial p}{\partial z} = \rho(p) \cdot g \cdot \cos(\beta) + \frac{\left(\frac{d\tau_w(p)}{dz}\right)}{(D_h/4)} + \left(\frac{\dot{m}_{inlet}}{A_T}\right)^2 \cdot \frac{1}{\rho(p)^3} \cdot \frac{\partial \rho(p)}{\partial z} \quad \text{Eq. B-1}$$

With the boundary condition  $p(z_0) = P_0$ .

Now we need to define expressions for the density and shear stress as a function of pressure. In the case of density an explicit expression (Eq. B-2) may be obtained, however the shear stress will be dependent on flow parameters. To solve this problem, the friction loss will be calculated to match the mass flowrate, which is known.

The density expression will follow from the equation of state of the foamed fluid derived from the base fluid density and the dispersed gas density as follows.

$$\rho(\phi) = (1 - \phi) \cdot \rho_{base-fluid} + \phi \cdot \left( \rho_{g,STD} \cdot \frac{P}{P_{STD}} \right) \quad \text{Eq. B-2}$$

Where:

$$\phi = \frac{RGL \cdot \frac{P_{STD}}{P}}{1 + RGL \cdot \frac{P_{STD}}{P}} \quad \text{Eq. B-3}$$

The expression for the shear-stress for a Herschel-Bulkley fluid will be as follows.

$$\tau_w(p) = \tau_y(p) + k(p) \cdot \left( \frac{\partial u}{\partial y} \right)_w^n \quad \text{Eq. B-4}$$

However, it is possible to correlate the shear-stress and pressure drop through an equilibrium balance, since the inertia terms are very small. So Eq. B-5 comes.

$$\tau_w(p) = \left( \frac{\partial p}{\partial z} \right)_{pdrop} \cdot \left( \frac{D_h}{4} \right) \quad \text{Eq. B-5}$$

In the case of the Slot geometry (Grinchik and Kim, 1974), the volumetric flow rate and velocity profile will be:

$$Q_{outer} = 2 \cdot b \cdot \left( \frac{n}{n+1} \right) \cdot \left( \frac{\partial p / \partial z}{k} \right)^{(1/n)} \left[ (H/2 - h_0)^{(1/n+1)} \cdot (H/2 - h_0) - \left( \frac{n}{2n+1} \right) \cdot (H/2 - h_0)^{1/n+2} \right]$$

$$Q_{shear-surface} = 2 \cdot b \cdot h_0 \cdot u(h_0)$$

$$Q_{total} = Q_{shear-surface} + Q_{outer} \quad \text{Eq. B-6}$$

$$u(y) = \left( \frac{n}{n+1} \right) \cdot \left( \frac{\partial p / \partial z}{k} \right)^{(1/n)} \cdot \left[ \left( \frac{H}{2} - h_0 \right)^{1+1/n} - (y - h_0)^{1+1/n} \right], \mathbf{h_0 \leq y \leq H/2}$$

$$u(y) = \left( \frac{n}{n+1} \right) \cdot \left( \frac{\partial p / \partial z}{k} \right)^{(1/n)} \cdot \left( \frac{H}{2} - h_0 \right)^{1+1/n}, \mathbf{y \leq h_0}$$

$$\text{Eq. B-7}$$

Where:

$H = R_{out} - R_{in}$  is half of the gap in the slot

$h_0 = \tau_y / (\partial p / \partial z)$  is half of the thickness of the shear surface

$k$  – Consistency index of the Herschel-Bulkley fluid

$n$  – behavior index of the Herschel-Bulkley fluid

$\partial p / \partial z$  – is the pressure drop due to friction in the flow

The numerical integration of Eq. B-1 can be performed, where the steps to calculate the pressure and velocity profiles are:

1. Start from the initial pressure and  $z_0$  coordinate;
2. For the pressure at previous  $Z$  coordinate, calculate gas volumetric fraction (eq. B-3);
3. Calculate at next  $Z$  coordinate the density and Herschel-Bulkley coefficients (Eq. B-2 and Eq. 3-20)
4. Calculate pressure drop between the  $Z$  coordinates with a shooting method to match the mass flow rate boundary condition (Eq. B-6);
5. Get velocity profile from the pressure drop calculated at step (4) and fluid data from step (3), (Eq. B-7);
6. Calculate the inertia and body force gradient terms in the pressure gradient (Eq. B-1);
7. Calculate the pressure next  $Z$  coordinate pressure from steps (4) and (6) (Eq. B-1);
8. Repeat steps (2) to (7) for every iteration up to the final  $Z$  coordinate.

The same process may be applied with the solution for the concentric annulus (Hanks and Richards, 1979) or a pipe geometry (Grinchik and Kim, 1974). In that case, the expressions for the flow rate at step (4) used to match the pressure drop will have to be changed to the exact solution for each case.

This exact solution for single-phase compressible flow is valid for 1D laminar flow and assumes steady-state flow with a constant mass flow rate.

# Appendix C – List of variables per case

Table C-1. Parameter list

Name	Density-1 (kg/m <sup>3</sup> )	GLR-1	Ty-1 (Pa)	k-1 (Pa.s <sup>n</sup> )	n-1	Density-2 (kg/m <sup>3</sup> )	GLR-2	Ty-2 (Pa)	k-2 (Pa.s <sup>n</sup> )	n-2	Surface Tension (N/m)	Liquid Pump Rate (m <sup>3</sup> /s)	Outlet Pressure (Pa)	Eccentricity Ratio	Well Inclination
Validation #1	1000	0	0	0,1	1	1000	0	0	0,1	1	0	0.010332	1.00E+06	0	0
Validation #2	1000	0	0	0,1	0,7	1000	0	0	0,1	0,7	0	0.010332	1.00E+06	0	0
Validation #3	1000	0	0,1	0,1	0,7	1000	0	0,1	0,1	0,7	0	0.010332	1.00E+06	0	0
Validation #4	1000	5	0,1	0,1	0,7	1000	5	0,1	0,1	0,7	0	0.010332	1.00E+06	0	0
Simple #1	1000	0	0,1	0,3	0,8	1900	4,5	1	0,5	0,7	0,07	0.020664	1.00E+06	0	0
Simple #2	1000	0	0,1	0,3	0,8	1900	4,5	1	0,5	0,7	0,07	0.020664	1.00E+06	0,5	0
Foam #1	1400	0	0,4	2	0,4	1900	28	4	0,5	0,85	0,07	0.020664	1.00E+07	0	0
Constant #2	1400	0	0,4	2	0,4	1500	0	4	0,5	0,85	0,07	0.020664	1.00E+07	0	0
Foam #3	1400	0	0,4	2	0,4	1900	28	4	0,5	0,85	0,07	0.020664	1.00E+07	0,5	0
Constant #4	1400	0	0,4	2	0,4	1500	0	4	0,5	0,85	0,07	0.020664	1.00E+07	0,5	0
Foam #5	1400	0	0,4	2	0,4	1900	28	4	0,5	0,85	0,07	0.020664	1.00E+07	0,75	0
Constant #6	1400	0	0,4	2	0,4	1500	0	4	0,5	0,85	0,07	0.020664	1.00E+07	0,75	0
Foam #7	1400	0	0,4	2	0,4	1900	28	4	0,5	0,85	0,07	0.020664	1.00E+07	0,5	45
Foam #8	1400	0	0,4	2	0,4	1900	28	4	0,5	0,85	0,07	0.020664	1.00E+07	0,5	90
Foam #9	1400	0	0,8	4	0,4	1900	28	4	0,5	0,85	0,07	0.020664	1.00E+07	0	0
Constant #10	1400	0	0,8	4	0,4	1500	0	4	0,5	0,85	0,07	0.020664	1.00E+07	0	0
Foam #11	1400	0	3	2	0,4	1900	28	4	0,5	0,85	0,07	0.020664	1.00E+07	0	0
Constant #12	1400	0	3	2	0,4	1500	0	4	0,5	0,85	0,07	0.020664	1.00E+07	0	0
Foam #13	1500	0	0,4	2	0,4	1900	28	4	0,5	0,85	0,07	0.020664	1.00E+07	0	0
Constant #14	1500	0	0,4	2	0,4	1500	0	4	0,5	0,85	0,07	0.020664	1.00E+07	0	0
Foam #15	1297	0	0,4	2	0,4	1900	28	4	0,5	0,85	0,07	0.020664	1.00E+07	0	0
Constant #16	1297	0	0,4	2	0,4	1500	0	4	0,5	0,85	0,07	0.020664	1.00E+07	0	0
Foam #17	1080	0	0,4	2	0,4	1900	28	4	0,5	0,85	0,07	0.020664	1.00E+07	0	0
Constant #18	1080	0	0,4	2	0,4	1500	0	4	0,5	0,85	0,07	0.020664	1.00E+07	0	0
Foam #19	1400	0	0,4	2	0,4	1900	28	4	0,5	0,85	0,07	0.012096	1.00E+07	0	0
Constant #20	1400	0	0,4	2	0,4	1500	0	4	0,5	0,85	0,07	0.012096	1.00E+07	0	0
Foam #21	1400	0	0,4	2	0,4	1500	0	4	0,5	0,85	0,07	0.035942	1.00E+07	0	0
Constant #22	1400	0	0,4	2	0,4	1500	0	4	0,5	0,85	0,07	0.035942	1.00E+07	0	0
Foam #23	1400	0	0,8	4	0,4	1900	28	4	0,5	0,85	0,07	0.020664	1.00E+07	0,5	45
Constant #24	1400	0	0,8	4	0,4	1500	0	4	0,5	0,85	0,07	0.020664	1.00E+07	0,5	45
Foam2 #25	1400	0	0,4	2	0,4	1900	28	4	0,5	0,85	0,07	0.020664	1.00E+07	0	0
Foam2 #26	1400	0	0,8	4	0,4	1900	28	4	0,5	0,85	0,07	0.020664	1.00E+07	0	0
Foam2 #27	1500	0	0,4	2	0,4	1900	28	4	0,5	0,85	0,07	0.020664	1.00E+07	0	0
Foam2 #28	1400	0	0,4	2	0,4	1900	28	4	0,5	0,85	0,07	0.020664	1.00E+07	0,5	0